NASA TM-87162

NASA Technical Memorandum 87162

NASA-TM-87162 19860005007

Secondary Pattern Computation of an Arbitrarily Shaped Main Reflector

Peter T.C. Lam and S.W. Lee
University of Illinois
Urbana, Illinois

and

R. Acosta
Lewis Research Center
Cleveland, Ohio

November 1985

LIBRARY COPY

DEC 6 1985

LANGLEY RESEARCH CENTER
LIBRARY, NASA
HAMPTON, VIRGINIA

NF01484

NASA

1. INTRODUCTION

Reflector antennas are widely used in communication satellite systems because of their relatively good radiation characteristics, low cost, and light weight. A central problem in the analysis of a reflector antenna is the secondary pattern computation. As sketched in Figure 1, for an incident field from a feed located at P_1, the problem is to calculate the scattered field $\vec{E}^s$ from a known reflector Σ at a far-field observation point $\vec{r}$. Several methods exist for calculating the high-frequency asymptotic solution of $\vec{E}^s(\vec{r})$, as explained below.

(i) Physical Optics Method (PO, Fig. 1a) [1]-[7]. The induced current on the reflector is approximated by $2\hat{n} \times \vec{H}^i$. An integration of this current over the curved reflector Σ gives the far field $\vec{E}^s$.

(ii) Geometrical Theory of Diffraction (GTD, Fig. 1b) [8]-[10]. At a far-field observation point $\vec{r}$, the scattered field $\vec{E}^s$ consists of two terms: the reflected field on ray $\overline{P_1O^r}$, and the edge diffracted field on ray $\overline{P_1O^d}$.

(iii) Aperture Integration Method (AI, Fig. 1c) [1],[11]-[13]. The field on aperture plane Σ_a is first calculated by tracing a reflected ray $\overline{P_1O^rP_2}$ using geometrical optics theory and an edge diffracted ray $\overline{P_1O^dP_2}$ using GTD. Next, we integrate the field over Σ_a via FFT to obtain the scattered far-field $\vec{E}^s$.

The accuracy of the above three methods is discussed below. As a reference, let us represent the exact solution of $\vec{E}^s$ by a high-frequency asymptotic series, namely,

N86-14477#

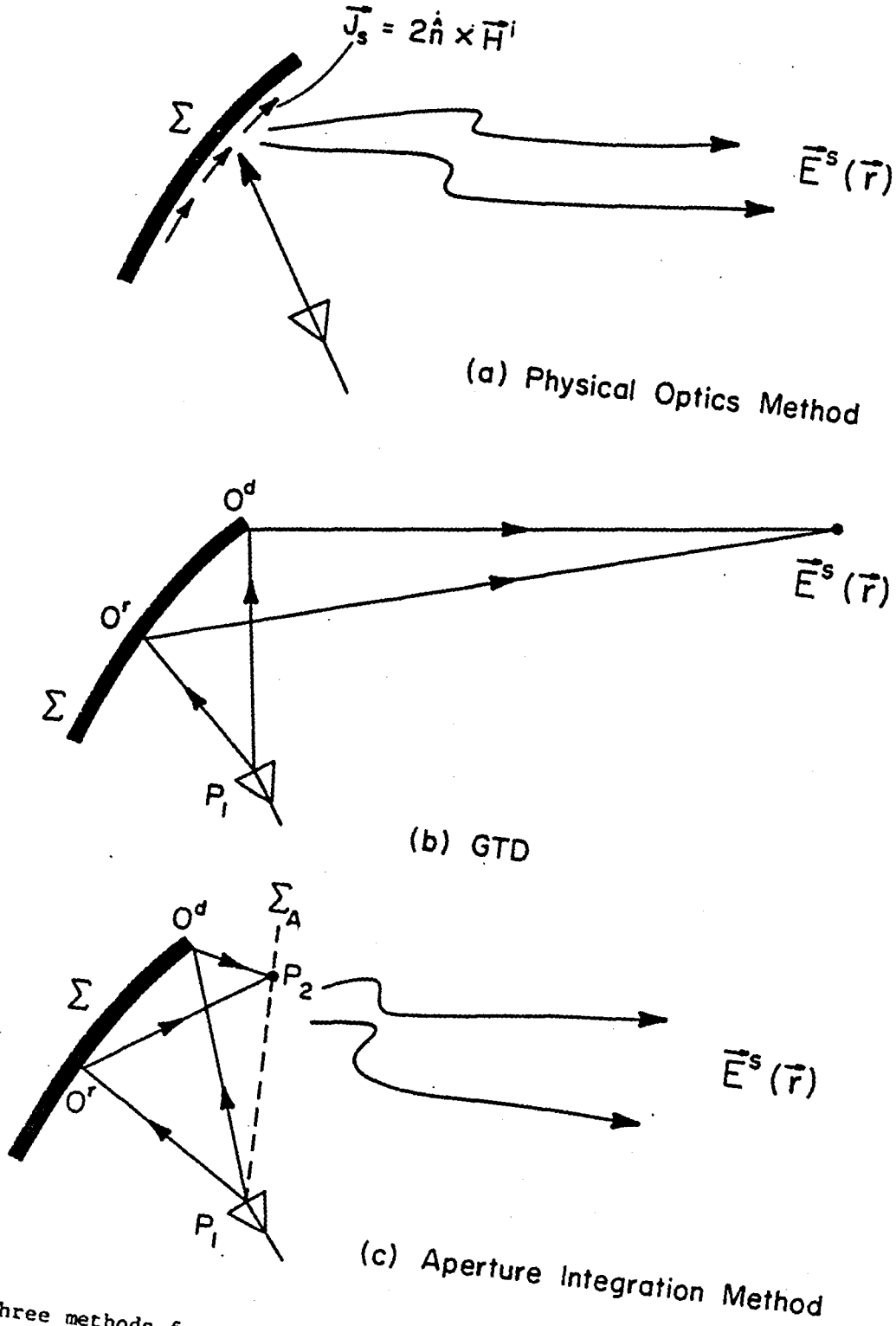

Figure 1. Three methods for calculating scattered field $\vec{E}^s$ from a reflector.

$$\vec{E}^s(\vec{r}) \sim e^{-jkS(\vec{r})}[\vec{A}_o(\vec{r}) + k^{-1/2}\vec{A}_1(\vec{r}) + k^{-1}\vec{A}_2(\vec{r}) + \ldots] \text{ , for } k \to \infty \quad (1.1)$$

Then, we may summarize the accuracy and limitations of the three methods in the following table:

TABLE 1

ACCURACY AND LIMITATIONS OF PO, AI, AND GTD

Methods	Accuracy	Limitation
PO AI	recover $\vec{A}_o$ and partial $\vec{A}_1$	not accurate for wide-angle lobes
GTD	recover $\vec{A}_o$ and $\vec{A}_1$	predicts infinite field in main beam direction (caustics)

In this report, we will study the main reflector far-field pattern using the aperture integration (AI) method for the following reasons:

(i) Unlike the other two methods, AI gives the near-field (aperture field) as well as the far field. Most of today's large reflector measurements are done in a near field range. Thus, only AI provides a convenient theoretical check for the near field measurements.

(ii) The accuracy of AI is comparable to the popular PO. The use of FFT in AI makes it numerically efficient. Furthermore, as will be discussed later, the present AI formulation is most suitable for extension to multiple (2 or more) reflectors.

There exists an extensive list of published literature on AI - notably, Silver [1], Kauffman and Croswell [11], Acosta [12], and Hwang, Tsao, and

Han [13]. In comparison with these prior works, the present AI analysis may be considered as an extension in one or more of the following areas:

(i) The surface of the reflector is completely arbitrary. It can be a numerically specified surface.

(ii) The edge of the reflector is not restricted to a circular curve. It can be an arbitrary curve lying on an elliptical cone or cylinder.

(iii) The divergence factor of the GO field is correctly computed. Hence, our analysis is not restricted to feeds located very close to the focal point (in which case the divergence factor is nearly unity and is ignored by several researchers).

(iv) The edge diffracted field is included in the aperture field calculation. Near the incident and reflected shadow boundaries, two uniform theories [14]-[15] are used so that the aperture field is continuous from the lit to the shadow region.

In short, the present AI analysis represents a generalized and improved version of previous work. In particular, it is amendable for a convenient extension for analyzing multiple reflectors.

The organization of this report is as follows: The description of the problem is described in Section 2. The incident field, feed coordinates, and power radiated from the feed are covered in Section 3. Sections 4 and 5 give a step-by-step procedure to compute the various contributions that make up the aperture field, namely, the geometrical optics and edge-diffracted fields. Section 6 covers the aperture field theory, the application of the FFT, and gain normalization. Numerical results and concluding remarks will be presented in Sections 7 and 8.

2. DESCRIPTION OF PROBLEM

The geometry of the problem under consideration is sketched in Figures 2 and 3. A reflector Σ is illuminated by the incident field from a point source at P_1. The problem is (a) to determine the high-frequency asymptotic solution of the total field at an observation point on the aperture grid Σ_a as shown in Figure 2, and (b) to determine the secondary pattern using the FFT as depicted in Figure 3. In this section, we shall describe the various elements involved in the problem.

2.1. Coordinate Systems and Time Convention

The main coordinate system is the rectangular system (x,y,z), whose origin and orientation are arbitrarily chosen. In calculating the edge diffracted field which involves the boundary of the reflector, we employ a primed rectangular system (x',y',z'), whose relation with (x,y,z) is explicitly stated later. The feed coordinate system (x_f,y_f,z_f) required to describe the polarization and incident field is related to the main coordinate system by Eulerian angles [16]. This will be discussed in detail in Section 3. The time factor is $\exp(+j\omega t)$ and is suppressed throughout.

2.2. Source

We assume that the source has a well-defined "phase center" at P_1 with coordinates (x_1,y_1,z_1), and radiates a spherical wave denoted by $(\vec{H}^i,\vec{E}^i)$. If the feed is an array, it is necessary to consider each element in the array separately and superimpose their final scattered fields.

2.3. Reflector Σ

The perfectly conducting surface is described by the equation

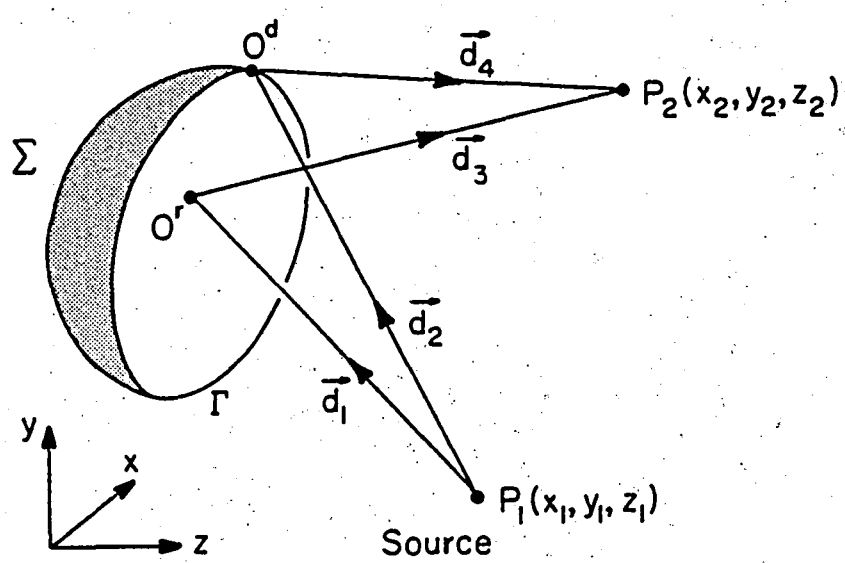

Figure 2. A reflector Σ with edge Γ being illuminated by the incident field from a point source at P_1.

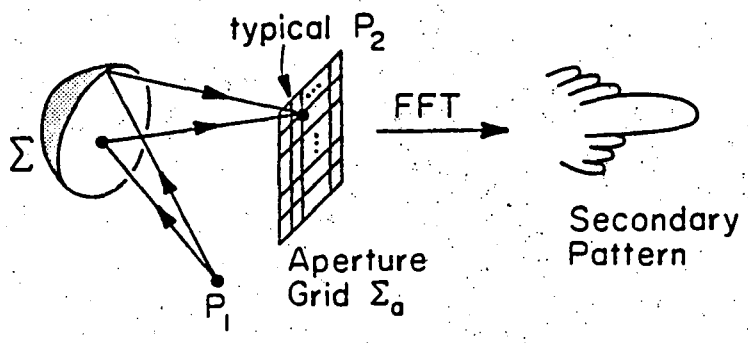

Figure 3. Secondary pattern using the Fast Fourier Transform.

$$z = f(x,y) \quad , \quad \text{for } a < x < b \quad \text{and} \quad c < y < d \tag{2.1}$$

It is not necessary to know the analytical form of the function f(x,y). In fact, the present computer program requires only a set of discrete data points (x_n, y_n, f_n) with $n = 1,2,\ldots,N$ as the description of Σ. Those points are fitted by a cubic spline which gives automatically first and second partial derivatives of f, namely, $\partial f/\partial x$, $\partial f/\partial y$, $\partial^2 f/\partial x^2$, $\partial^2 f/\partial x \partial y$, $\partial^2 f/\partial y^2$. There are two requirements on the cubic-spline fit: (i) the data points can be distributed over a random grid, but they must be dense enough to describe the fine details of Σ; (ii) the domain of the data points $(a < x < b, c < y < d)$ must be somewhat greater than the area defined by the boundary Γ of the reflector. Thus, we must know surface Σ in the shaded region in Figure 4 as well. Typically, the "width" of the shaded region is about 3 to 4 wavelengths. Our present program contains an extrapolation subroutine, which automatically extends Σ outward "smoothly to obtain the necessary data points in the shaded region." The final scattered field, for all practical purposes, is independent of the surface outside Γ. Consequently, the exact manner in which the extrapolation is done is unimportant.

2.4. Boundary Γ

Two types of reflector boundaries are most frequently used in practice, and they receive our special attention.

(a) Cylinder Case. In the first case, Γ is the intersection of surface Σ and an elliptical cylinder (Figure 5a). The parameters of the cylinder are:

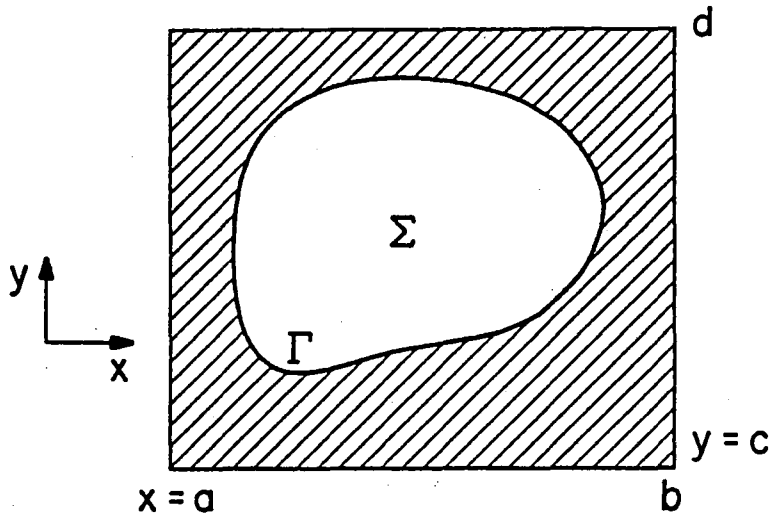

Figure 4. Projection of reflector $\sum$ and its boundary Γ on x-y plane.

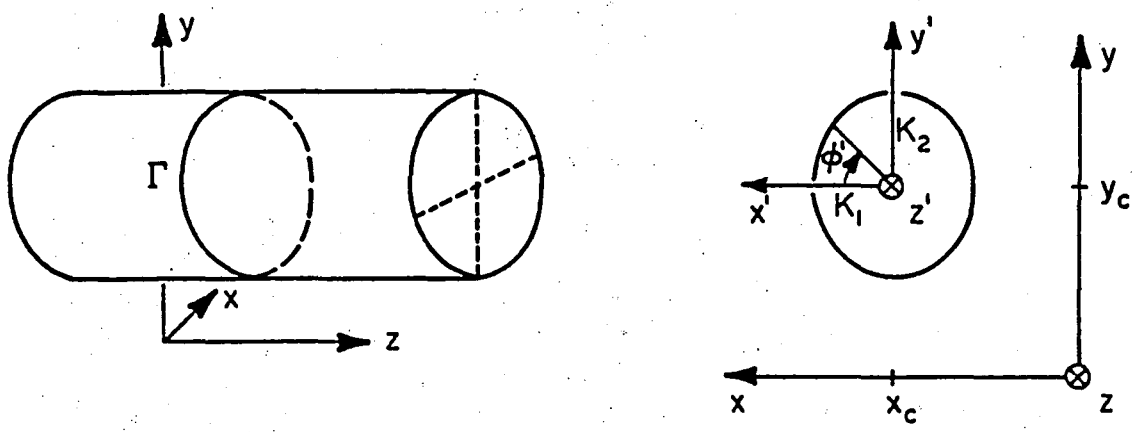

a. Γ on elliptical cylinder.

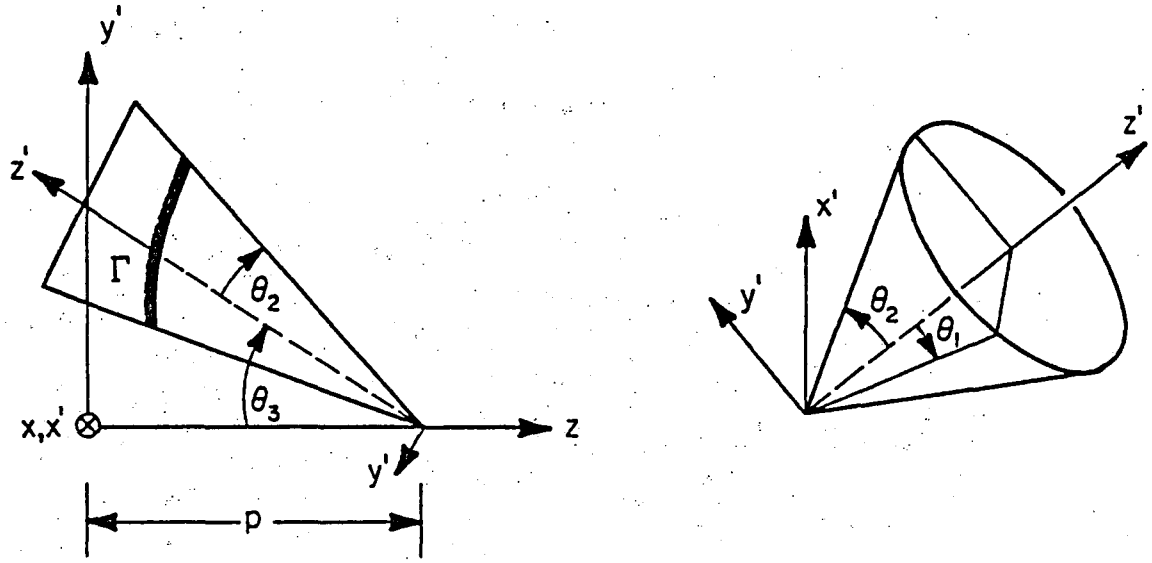

b. Γ on elliptical cone.

Figure 5. Two examples of boundary Γ of the reflector.

(x_c, y_c) = center of the ellipse

(K_1, K_2) = semiaxis along (x,y) direction.

Using a point on the axis of the cylinder as the origin, we introduce the second rectangular coordinates system (x', y', z') such that

$$\begin{cases} x' = x - x_c \\ y' = y - y_c \\ z' = z \end{cases} \tag{2.2}$$

The curve Γ may be described by a parametric equation with parameter ϕ', $0 \leq \phi' < 2\pi$,

$$\Gamma: \begin{cases} x' = g_1(\phi') = \rho' \cos \phi' \\ y' = g_2(\phi') = \rho' \sin \phi' \\ z' = g_3(\phi') = f(x = x_c + g_1, y = y_c + g_2) \end{cases} \tag{2.3}$$

where

$$\rho' = \left[\left(\frac{\cos \phi'}{K_1}\right)^2 + \left(\frac{\sin \phi'}{K_2}\right)^2\right]^{-1/2} \tag{2.4}$$

The projection of Γ on the x-y plane is always an ellipse.

(b) Cone Case. In the second case, Γ is the intersection of surface Σ and an elliptical cone (Figure 5b). The axis of the cone lies in the $y' - z'$ plane and its parameters are

$(x = 0, y = 0, z = -p)$ = tip of cone

θ_3 = inclination angle of cone axis measured from z-axis

(θ_1, θ_2) = half-cone angles in the $x' - z'$ and $y' - z'$ plane

Using the cone tip as the origin, the primed coordinates (x', y', z') are introduced such that

$$\begin{cases} x' = x \\ y' = -y \cos \theta_3 - (z - p) \sin \theta_3 \\ z' = y \sin \theta_3 - (z - p) \cos \theta_3 \end{cases} \tag{2.5}$$

Using parameters ϕ', the curve Γ is described by

$$\Gamma: \begin{cases} x' = g_1(\phi') = \rho' \cos \phi' \\ y' = g_2(\phi') = \rho' \sin \phi' \\ z' = g_3(\phi') = \rho'\left[(\cot \theta_1 \cos \phi')^2 + (\cot \theta_2 \sin \phi')^2\right]^{1/2} \end{cases} \tag{2.6}$$

To determine ρ' as a function of ϕ', we must solve the following nonlinear equation:

$$f(x,y) - p + y' \sin \theta_3 + z' \cos \theta_3 = 0 \tag{2.7}$$

For a given ϕ', there is a unique root ρ' from (2.7). The pair (ϕ', ρ') gives the desired relation $\rho' = \rho'(\phi')$, which is fitted by spline functions. The projection of Γ on the x-y plane is, in general, a pear-shaped curve.

(c) Arbitrary Case. In addition to the above two frequently used special cases, Γ may be an arbitrary curve described by

$$x' = g_1(\phi'), y' = g_2(\phi'), z' = g_3(\phi')$$

where (x', y', z') is related to (x,y,z) by either (2.2) or (2.5). The functions (g_1, g_2, g_3) can be specified either analytically or numerically.

2.5. Aperture Grid Points

A general point on the aperture plane Σ_a is denoted by P_2 with coordinates (x_2, y_2, z_2). Each point on Σ_a as shown in Figure 3 is fed into the computer for repeated calculations of the scattered field. It is essential that successive observation points are adjacent, because of the following fact. In determining the reflection (specular) points on the reflector, we make an exhaustive search only for the first observation point in a batch. From the second point on, we use the reflection point of the previous observation point as the initial guess for the current reflection point. It is only when successive observation points are adjacent that such an initial guess ensures fast convergence. In the cases that were considered, only one iteration was needed to obtain the reflection point for all observation points other than the first observation point.

2.6. Method of Solution

For a given incident field $(\vec{H}^i, \vec{E}^i)$ from the source at P_1, the asymptotic solution of the total field $(\vec{H}^t, \vec{E}^t)$ at point P_2 is determined by Keller's geometrical theory of diffraction (GTD) [17]. Explicitly, the total magnetic field is asymptotically given by

$$\text{Keller:} \quad \vec{H}^t(P_2) = \vec{H}^g + \vec{H}^d + O(k^{-1}), \qquad k \to \infty \tag{2.8}$$

Here $\vec{H}^g$, the geometrical optics field, is of order k^0 relative to the incident field and is the dominant term. The second term $\vec{H}^d$ is the edge-diffracted field and is of order $k^{-1/2}$. It is well-known that $\vec{H}^d$ becomes infinite and (2.8) fails if observation point P_2 is close to the incident or reflected shadow boundary. In the latter case, we will use the uniform asymptotic theory (UAT) [14], [18]-[21], which amounts to replacing $\vec{H}^d$ in

(2.8) by a new term $\vec{H}^D$ (with capital D):

$$\text{UAT:} \quad \vec{H}^t(P_2) = \vec{H}^g + \vec{H}^D + O(k^{-1}) \ , \quad k \to \infty \tag{2.9}$$

Once $\vec{H}^t$ is found, we calculate $\vec{E}^t$ from it by using the fact that $\vec{H}^g$, $\vec{H}^d$, and $\vec{H}^D$ are all the so-called "ray fields" which are locally plane waves.

Once the tangential fields ($\vec{E}^t$ or $\vec{H}^t$) on Σ_a are obtained, the Fourier transform of these fields will essentially produce the secondary pattern. This will be discussed in detail in Section 6.

3. INCIDENT FIELD

The definition of the incident field is given. The incident power from an arbitrarily polarized feed is derived so that the secondary pattern has the correct gain level. Finally, the computation of the incident field at a point on the reflector in the reflector system is described.

3.1. Definition of Incident Field

The surface current at the radiating aperture of the feed element may be expressed as

$$\vec{J}(x,y) = I(\hat{x}\, ae^{j\psi} + \hat{y}b) \tag{3.1}$$

where (a,b,ψ) are real and

$$a^2 + b^2 = 1 \quad . \tag{3.2}$$

By choosing (a,b,ψ), one may obtain any feed polarization. Table 2 shows the values of a,b,ψ corresponding to linear and circular polarizations.

TABLE 2

VARIOUS FEED POLARIZATIONS

	a	b	ψ
linear x	1	0	0
linear y	0	1	0
RHCP	$1/\sqrt{2}$	$1/\sqrt{2}$	90°
LHCP	$1/\sqrt{2}$	$1/\sqrt{2}$	-90°

The radiated electric field due to $\vec{J}$ given by (3.1) is

$$\vec{E} \sim \frac{e^{-jkr}}{r} \vec{f}(\theta,\phi) \tag{3.3}$$

where $\vec{f}(\theta,\phi)$ is the active element pattern. The function $\vec{f}(\theta,\phi)$ may be approximately expressed by

$$\vec{f}(\theta,\phi) = \hat{\theta} U_E(\theta)(ae^{j\psi} \cos\phi + b \sin\phi) + \hat{\phi} U_H(\theta)(b \cos\phi - ae^{j\psi} \sin\phi) \tag{3.4}$$

where

$U_E(\theta)$ = E-plane active pattern

$U_H(\theta)$ = H-plane active pattern

Typically, these active patterns may be approximated by $(\cos\theta)^q$, i.e.,

$$U_E(\theta) = (\cos\theta)^{q_E} \tag{3.5a}$$

$$U_H(\theta) = (\cos\theta)^{q_H} \tag{3.5b}$$

3.2. Incident Power Radiated

From (3.3) and (3.4), the radiated electric field is given by

$$\vec{E} \sim \frac{e^{-jkr}}{r} \left[U_E(\theta)(ae^{j\psi} \cos\phi + b \sin\phi)\hat{\theta} + U_H(\theta)(b \cos\phi - ae^{j\psi} \sin\phi)\hat{\phi} \right] \tag{3.6}$$

The power radiated, assuming forward radiation only, is

$$P_{inc} = \int_{\phi=0}^{2\pi} \int_{\theta=0}^{\pi/2} \frac{\vec{E}\cdot\vec{E}^*}{Z_o} r^2 \sin\theta \, d\theta \, d\phi \tag{3.7}$$

where

$$Z_o = 120\pi \text{ ohms.} \tag{3.8}$$

Using (3.2), (3.6), and (3.8), the incident power radiated is

$$P_{inc} = \frac{1}{120} \int_0^{\pi/2} \left[U_E U_E^* + U_H U_H^* \right] \sin\theta \, d\theta \tag{3.9}$$

For $(\cos\theta)^q$ type patterns,

$$P_{inc} = \frac{q_E + q_H + 1}{60(2q_E + 1)(2q_H + 1)} \tag{3.10}$$

3.3. Determining the Incident Field on the Reflector

The geometry of this problem is illustrated in Figure 6. The feed coordinate system (x_f, y_f, z_f) and the main reflector system (x,y,z) are related by Eulerian angles $\gamma_1, \gamma_2, \gamma_3$. In the most general case, these Cartesian systems can be aligned by three rotations. The angles of these rotations are known as Eulerian angles. Figure 7 illustrates the Eulerian angles $\gamma_1, \gamma_2, \gamma_3$. The definitions of these angles [22] are as follows. Angle γ_1 describes a counterclockwise (ccw) rotation about the z axis which brings the x axis to the x" axis aligned with the line of nodes (line of intersection between xy and $x_f y_f$ planes), angle γ_2 defines a rotation about the line of nodes in a ccw sense as indicated so that this brings the z axis to z_f, and angle γ_3 is another rotation about the z_f axis and aligns the x" axis with the x_f axis in a ccw sense. Typically, $\hat{x}_f$ and $\hat{z}_f$ are given. Let these unit vectors be expressed by

$$\hat{x}_f = x_1\hat{x} + x_2\hat{y} + x_3\hat{z} \tag{3.11}$$

$$\hat{z}_f = z_1\hat{x} + z_2\hat{y} + z_3\hat{z} \tag{3.12}$$

Then, the Eulerian angles are given by

$$\gamma_1 = \tan^{-1}\left(\frac{z_1}{-z_2}\right) \tag{3.13}$$

$$\gamma_2 = \tan^{-1}\left(\frac{\sqrt{1 - z_3^2}}{z_3}\right) \tag{3.14}$$

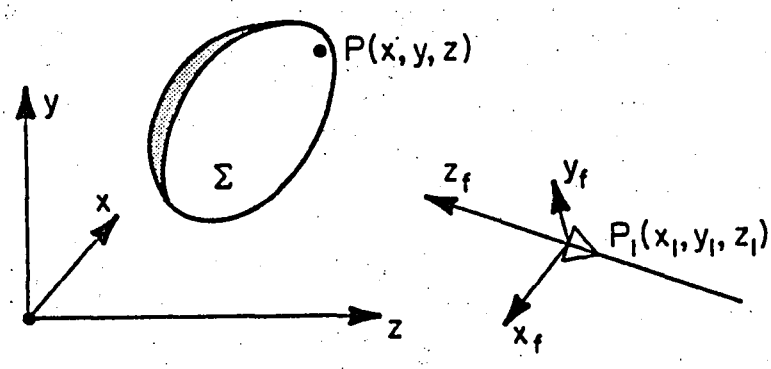

Figure 6. Feed and reflector coordinate systems.

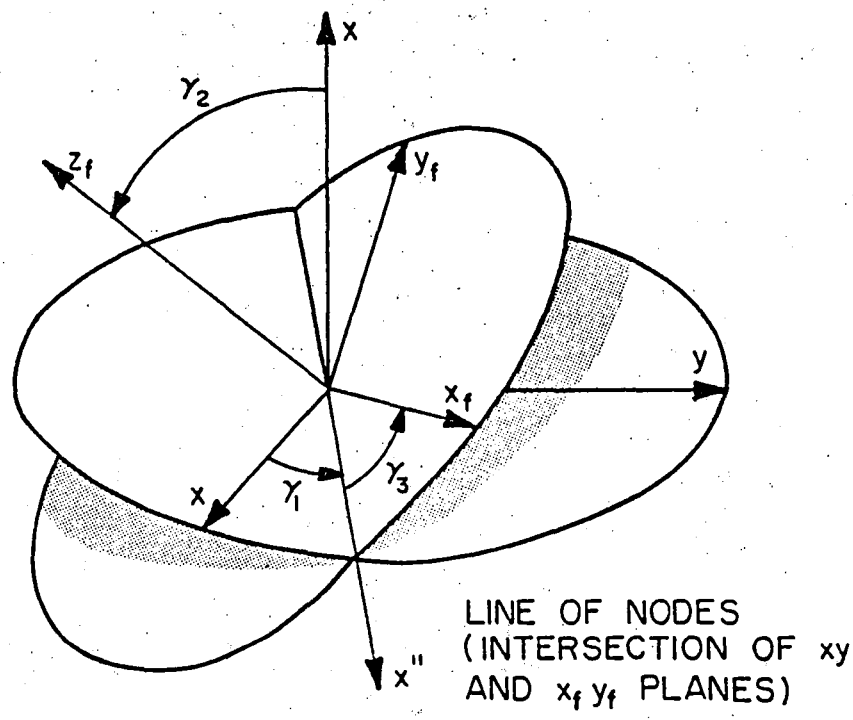

Figure 7. Eulerian angles.

$$\gamma_3 = \tan^{-1}\left(\frac{x_3}{z_1 x_2 - x_1 z_2}\right) \tag{3.15}$$

From [16], it can be shown that

$$[\hat{x}_f \ \hat{y}_f \ \hat{z}_f]^T = \bar{\bar{A}}[\hat{x} \ \hat{y} \ \hat{z}]^T \tag{3.16}$$

where

$$\bar{\bar{A}} = \begin{bmatrix} \cos\gamma_1\cos\gamma_3 - \sin\gamma_1\cos\gamma_2\sin\gamma_3 & \sin\gamma_1\cos\gamma_3 + \cos\gamma_1\cos\gamma_2\sin\gamma_3 & \sin\gamma_2\sin\gamma_3 \\ -\cos\gamma_1\sin\gamma_3 - \sin\gamma_1\cos\gamma_2\cos\gamma_3 & \cos\gamma_1\cos\gamma_2\cos\gamma_3 - \sin\gamma_1\sin\gamma_3 & \sin\gamma_2\cos\gamma_3 \\ \sin\gamma_1\sin\gamma_2 & -\cos\gamma_1\sin\gamma_2 & \cos\gamma_2 \end{bmatrix} \tag{3.17}$$

Thus, a point with coordinates (x,y,z) in the main coordinate system on Σ has coordinates (x^F, y^F, z^F) in the feed coordinate system given by

$$\begin{bmatrix} x^F \\ y^F \\ z^F \end{bmatrix} = \bar{\bar{A}} \begin{bmatrix} x - x_1 \\ y - y_1 \\ z - z_1 \end{bmatrix} \tag{3.18}$$

The corresponding spherical coordinates are

$$\begin{cases} r_f = [(x^F)^2 + (y^F)^2 + (z^F)^2]^{1/2} \\ \theta_f = \cos^{-1}(z^F/r_f) \\ \phi_f = \tan^{-1}(y^F/x^F) \end{cases} \tag{3.19}$$

From the feed function given by (3.6), the incident E-field may be obtained. To find the incident H-field, the following equation is used:

$$\vec{H}_{inc} \triangleq [H_{r_f} \; H_{\theta_f} \; H_{\phi_f}]^T = \frac{\hat{r} \times \vec{E}_{inc}}{Z_o} \tag{3.20}$$

where Z_o is given by (3.8). Next, the incident field is converted from spherical components to rectangular components using

$$\begin{bmatrix} H_{x_f} \\ H_{y_f} \\ H_{z_f} \end{bmatrix} = \begin{bmatrix} \sin\theta_f \cos\phi_f & \cos\theta_f \cos\phi_f & -\sin\phi_f \\ \sin\theta_f \sin\phi_f & \cos\theta_f \sin\phi_f & \cos\phi_f \\ \cos\theta_f & -\sin\theta_f & 0 \end{bmatrix} \begin{bmatrix} H_{r_f} \\ H_{\theta_f} \\ H_{\phi_f} \end{bmatrix} \tag{3.21}$$

Finally, the incident H-field in the (x_f, y_f, z_f) system is converted to the (x,y,z) system using the following equation

$$\begin{bmatrix} H_x \\ H_y \\ H_z \end{bmatrix} = \bar{\bar{A}}^T \begin{bmatrix} H_{x_f} \\ H_{y_f} \\ H_{z_f} \end{bmatrix} \tag{3.22}$$

where $\bar{\bar{A}}$ is given by (3.17).

4. GEOMETRICAL OPTICS FIELD

The geometrical optics field $\vec{H}^g$ in (2.8) consists of two components: the incident field $\vec{H}^i$ and the reflected field $\vec{H}^r$ which is calculated in this section. It should be noted that the incident field at an observation point on the aperture grid is taken to be zero because the incident field does not contribute to the secondary pattern.

4.1. Reflection Point

For a given source point P_1 and an observation point P_2 (Figure 2), a reflection point O^r may exist on the reflector Σ, and we denote its coordinates by $(x,y,z=f(x,y))$. The vectors

$$\vec{d}_1 = \hat{x}(x - x_1) + \hat{y}(y - y_1) + \hat{z}(f(x,y) - z_1) \tag{4.1a}$$

$$\vec{d}_2 = \hat{x}(x_2 - x) + \hat{y}(y_2 - y) + \hat{z}(z_2 - f(x,y)) \tag{4.1b}$$

are the connecting vectors between P_1 and O^r, and O^r and P_2, respectively. The condition on the reflection point is that the distance $(d_1 + d_2)$ must be stationary, i.e.,

$$\frac{\partial}{\partial x}(d_1 + d_2) = 0 \quad , \quad \frac{\partial}{\partial y}(d_1 + d_2) = 0 \tag{4.2}$$

which is explicitly given by

$$\begin{cases} \frac{1}{d_1}\left\{(x - x_1) + \left[f(x,y) - z_1\right]\frac{\partial f}{\partial x}\right\} + \frac{1}{d_2}\left\{(x - x_2) + \left[f(x,y) - z_2\right]\frac{\partial f}{\partial x}\right\} = 0 \\ \\ \frac{1}{d_1}\left\{(y - y_1) + \left[f(x,y) - z_1\right]\frac{\partial f}{\partial y}\right\} + \frac{1}{d_2}\left\{(y - y_2) + \left[f(x,y) - z_2\right]\frac{\partial f}{\partial y}\right\} = 0 \end{cases} \tag{4.3a}$$

A root (x,y,z=f) of the two nonlinear equations in (4.3a) gives the location of a reflection point. For a given P_1 and P_2, there may be none, one, or more than one reflection point. It may be shown that (4.3a) is equivalent to the satisfaction of Snell's law.

The system of equations (4.3a) can be also satisfied if P_1, O^r, and P_2 are collinear. Such a spurious root may be eliminated by an additional condition

$$\left(\frac{x - x_1}{d_1} + \frac{x - x_2}{d_2}\right)^2 + \left(\frac{y - y_1}{d_1} + \frac{y - y_2}{d_2}\right)^2 + \left(\frac{z - z_1}{d_1} + \frac{z - z_2}{d_2}\right)^2 > \delta \tag{4.3b}$$

where δ is a small positive number. We set $\delta = 0.0001$.

A root of (4.3) may or may not fall inside the boundary Γ of the reflector (Figure 4). Thus, for each root (x,y,z=f) or its corresponding coordinates (x', y', z') in the primed system, the following test must be performed. If

$$\sqrt{(x')^2 + (y')^2} \leq \ell_1 \tag{4.4}$$

then the root is inside Γ and it is indeed a reflection point on the reflector. If (4.4) is not satisfied, then the root should be discarded. The parameter ℓ_1 in (4.4) is given by

$$\ell_1 = \left[(x')^2 + (y')^2\right]^{1/2} \left[\left(\frac{x'}{K_1}\right)^2 + \left(\frac{y'}{K_2}\right)^2\right]^{-1/2} \tag{4.5a}$$

if Γ lies on an elliptical cylinder (Figure 5a); and

$$\ell_1 = |z'| \left[(x')^2 + (y')^2\right]^{1/2} \left[(x' \cot \theta_1)^2 + (y' \cot \theta_2)^2\right]^{-1/2} \tag{4.5b}$$

if Γ lies on an elliptical cone (Figure 5b).

4.2. Formula for Reflected Field

The reflected magnetic field at P_2 is given by

$$\vec{H}^r(P_2) = (DF)\, e^{-jkd_2}\{\vec{H}^i(O^r) - 2[\vec{H}^i(O^r)\cdot\hat{N}]\hat{N}\} \tag{4.6}$$

which is given in terms of the incident field $\vec{H}^i$ at the reflection point O^r, the surface normal $\hat{N}$ of the reflector at O^r, and a divergence factor DF. We choose $\hat{N}$ pointing toward the source; thus, $(\hat{N}\cdot\hat{z})$ is always greater than zero (Figure 8). Explicitly, $\hat{N}$ is given by

$$\hat{N} = \Delta(-f_x\hat{x} - f_y\hat{y} + \hat{z}) \tag{4.7}$$

where $\Delta = +(f_x^2 + f_y^2 + 1)^{-1/2}$ and the subscript x of f_x, for example, means partial derivative with respect to x. The divergence factor in (4.6) is

$$DF = \frac{1}{\sqrt{1 + (d_2/R_1^r)}} \cdot \frac{1}{\sqrt{1 + (d_2/R_2^r)}} \tag{4.8}$$

where the square roots take positive real, negative imaginary, or zero value (so that DF is positive real, positive imaginary or infinite). (R_1^r, R_2^r) are the principal radii of curvature of the reflected wavefront passing through O^r. Their computation is given next.

4.3. Curvatures of Reflected Wavefront

We use the formulas given in Section IV of [18] for calculating (R_1^r, R_2^r). The three orthonormal base vectors of the incident pencil are chosen to be (Figure 8)

$$\hat{x}_1^i = \frac{\hat{y} \times \hat{x}_3^i}{|\hat{y} \times \hat{x}_3^i|} = \frac{\hat{x}(z - z_1) - \hat{z}(x - x_1)}{[(z - z_1)^2 + (x - x_1)^2]^{1/2}} \tag{4.9a}$$

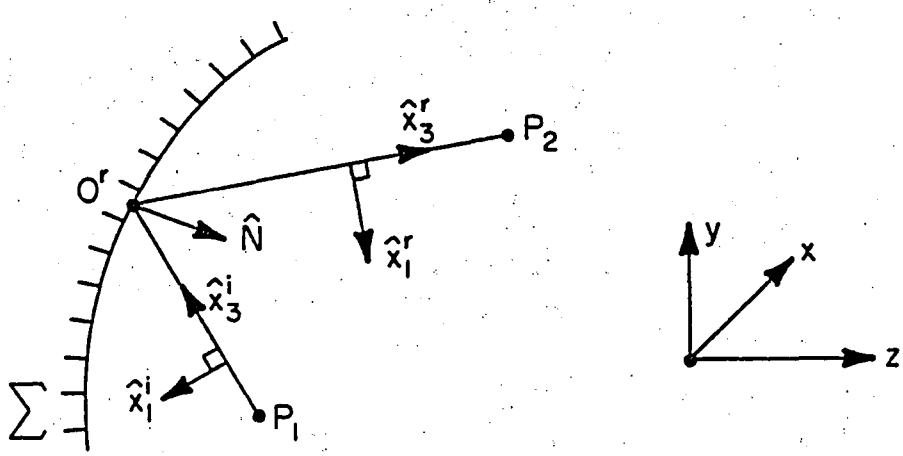

Figure 8. Reflection from reflector Σ.

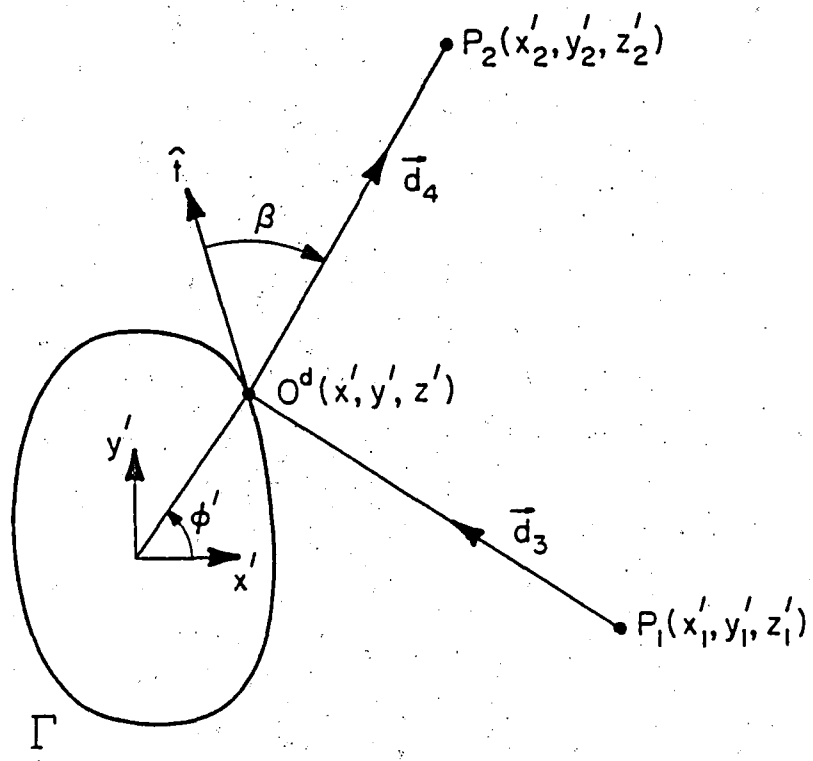

Figure 9. Diffraction from boundary Γ of the reflector.

$$\hat{x}_2^i = \frac{\hat{x}_3^i \times \hat{x}_1^i}{|\hat{x}_3^i \times \hat{x}_1^i|} \tag{4.9b}$$

$$\hat{x}_3^i = \frac{\hat{x}(x - x_1) + \hat{y}(y - y_1) + \hat{z}(z - z_1)}{[(x - x_1)^2 + (y - y_1)^2 + (z - z_1)^2]^{1/2}} \tag{4.9c}$$

where (x,y,z) are the coordinates of the reflection point O^r. Those of the reflected pencil are chosen to be

$$\hat{x}_1^r = \hat{x}_1^i - 2(\hat{x}_1^i \cdot \hat{N})\hat{N} \tag{4.10a}$$

$$\hat{x}_2^r = \hat{x}_2^i - 2(\hat{x}_2^i \cdot \hat{N})\hat{N} \tag{4.10b}$$

$$\hat{x}_3^r = \frac{\hat{x}(x_2 - x) + \hat{y}(y_2 - y) + \hat{z}(z_2 - z)}{[(x_2 - x)^2 + (y_2 - y)^2 + (z_2 - z)^2]^{1/2}} \tag{4.10c}$$

Note that (4.10) chosen above is a left-handed system, i.e., $\hat{x}_1^r \times \hat{x}_2^r = -\hat{x}_3^r$. This choice, of course, does not affect the final solutions of (R_1^r, R_2^r). The three orthonormal base vectors of reflector Σ at O^r are chosen to be

$$\hat{x}_1^\Sigma = \frac{\hat{x} + \hat{z}f_x}{(1 + f_x^2)^{1/2}} \tag{4.11a}$$

$$\hat{x}_2^\Sigma = \frac{\hat{y} + \hat{z}f_y}{(1 + f_y^2)^{1/2}} \tag{4.11b}$$

$$\hat{x}_3^\Sigma = \hat{N} \tag{4.11c}$$

From (4.9) and (4.11) the elements

$$P^i_{mn} = \hat{x}^i_m \cdot \hat{x}^\Sigma_n \quad , \quad m,n = 1,2,3 \tag{4.12}$$

can be calculated with the results

$$p^i_{11} = \frac{(z - z_1) - f_x(x - x_1)}{[1 + f_x^2]^{1/2}\ [(x - x_1)^2 + (z - z_1)^2]^{1/2}} \tag{4.13a}$$

$$p^i_{12} = \frac{-f_y(x - x_1)}{[1 + f_y^2]^{1/2}\ [(x - x_1)^2 + (z - z_1)^2]^{1/2}} \tag{4.13b}$$

$$p^i_{21} = \frac{-(x-x_1)(y-y_1)-f_x(y-y_1)(z-z_1)}{[1+f_x^2]^{1/2}\{(x-x_1)^2(y-y_1)^2+[(z-z_1)^2+(x-x_1)^2]^2+(y-y_1)^2(z-z_1)^2\}^{1/2}} \tag{4.13c}$$

$$p^i_{22} = \frac{(z-z_1)^2+(x-x_1)^2-f_y(y-y_1)(z-z_1)}{[1+f_y^2]^{1/2}\{(x-x_1)^2(y-y_1)^2+[(z-z_1)^2+(x-x_1)^2]^2+(y-y_1)^2(z-z_1)^2\}^{1/2}} \tag{4.13d}$$

$$p^i_{33} = \frac{1}{d_1}\ \Delta[f_x(x - x_1) + f_y(y - y_1) - (z - z_1)] \tag{4.13e}$$

The first four elements in (4.13a) through (4.13d) form the 2 × 2 matrix $\bar{\bar{P}}^i$. Because of the particular choice in (4.10), we have $\bar{\bar{P}}^r = \bar{\bar{P}}^i$. The curvature matrix of the incident pencil is

$$\bar{\bar{Q}}^i = \begin{bmatrix} d_1^{-1} & 0 \\ 0 & d_1^{-1} \end{bmatrix} \tag{4.14}$$

The curvature matrix of reflector Σ at O^r is

$$\bar{\bar{Q}}^{\Sigma} = \begin{bmatrix} \Delta^2(eG - fF) & \Delta^2(fE - eF) \\ \Delta^2(fG - gF) & \Delta^2(gE - fF) \end{bmatrix} \tag{4.15}$$

where

$$E = 1 + f_x^2 \quad , \quad F = f_x f_y \quad , \quad G = 1 + f_y^2$$

$$e = -\Delta f_{xx} \quad , \quad f = -\Delta f_{xy} \quad , \quad g = \Delta f_{yy}$$

Δ is defined just below (4.7)

The desired curvature matrix $\bar{\bar{Q}}^r$ may be calculated from the following matrix equation

$$\bar{\bar{Q}}^r = \bar{\bar{Q}}^i + 2p_{33}^i[(\bar{\bar{P}}^i)^T]^{-1}\,\bar{\bar{Q}}^{\Sigma}(\bar{\bar{P}}^i)^{-1} \tag{4.16}$$

Let us denote the four elements of $\bar{\bar{Q}}^r$ by

$$\bar{\bar{Q}}^r = \begin{bmatrix} Q_{11} & Q_{12} \\ Q_{21} & Q_{22} \end{bmatrix} \tag{4.17}$$

Then the desired radii of curvature of the reflected wavefront at O^r are given by

$$\frac{1}{R_1^r}, \frac{1}{R_2^r} = \frac{1}{2}\left\{(Q_{11} + Q_{22})^2 \pm \sqrt{(Q_{11} + Q_{22})^2 - 4(Q_{11}Q_{22} - Q_{12}Q_{21})}\right\} \tag{4.18}$$

Both R_1^r and R_2^r are real. Their signs have the following meaning: If R_1^r is positive (negative), the corresponding normal section of the reflected wavefront is divergent (convergent). The same convention applies to R_2^r.

Two final remarks about the calculation of the reflected field: (i) For a given P_1 and P_2, there may be more than one reflection point on Σ. Then the total reflected field is the superposition of the contributions from each reflection point. If there is no reflection point on Σ, the reflected field is zero; (ii) If the reflection point is close to the boundary Γ, we still calculate its reflected field in the usual manner. We shall adjust the diffracted field $\vec{H}^d$ later by using UAT so that the total field $\vec{H}^t$ in this case is correct.

5. EDGE-DIFFRACTED FIELD

5.1. Diffraction Points

To calculate the edge-diffracted field, the diffraction points on the boundary Γ of the reflector must be located first. Consider a source point P_1 at (x_1', y_1', z_1') and an observation point P_2 at (x_2', y_2', z_2'), with their coordinates given in the primed system (Figure 9). A diffraction point 0^d with coordinates (x', y', z') can be determined from the law of diffraction

$$\frac{1}{d_3}\vec{d}_3 \cdot \hat{t} = \frac{1}{d_4}\vec{d}_4 \cdot \hat{t} \tag{5.1}$$

Here $\hat{t}$ is the unit tangent of Γ at 0^d, and

$$\vec{d}_3 = \hat{x}'(x' - x_1') + \hat{y}'(y' - y_1') + \hat{z}'(z' - z_1') \tag{5.2a}$$

$$\vec{d}_4 = \hat{x}'(x_2' - x') + \hat{y}'(y_2' - y') + \hat{z}'(z_2' - z') \tag{5.2b}$$

From Fermat's principle, (5.1) is equivalent to

$$\frac{d}{d\phi'}(d_3 + d_4) = 0 \tag{5.3}$$

From (5.2), (5.3) may be written as a nonlinear equation for unknown ϕ':

$$\left(\frac{g_1 - x_1'}{d_3} + \frac{g_1 - x_2'}{d_4}\right)\frac{\partial g_1}{\partial \phi'} + \left(\frac{g_2 - y_1'}{d_3} + \frac{g_2 - y_2'}{d_4}\right)\frac{\partial g_2}{\partial \phi'}$$

$$+ \left(\frac{g_3 - z_1'}{d_3} + \frac{g_3 - z_2'}{d_4}\right)\frac{\partial g_3}{\partial \phi'} = 0 \tag{5.4}$$

where (g_1, g_2, g_3) are defined in (2.3) if Γ lies on a cylinder, and in (2.6) if Γ lies on a cone. A root of ϕ' of (5.4) determines a diffraction point

on Γ. Depending on the geometry, there exist examples where as many as four diffraction points have been found.

5.2. Formula for Diffracted Field

Corresponding to each diffraction point O^d, there is a contribution to the diffracted field $\vec{H}^d$ in (2.8). Following Equation (5.21) of [18], the formula for such a contribution reads

$$\vec{H}^d(P_2) = g(kd_4) \frac{1}{\sqrt{1 + (d_4/R_1)}} \frac{1}{\sin\beta} \left[\hat{\beta} D^h H^i_\beta + \hat{\alpha} D^s H^i_\alpha\right] \tag{5.5}$$

Here g is a cylindrical wave factor

$$g(x) = \frac{1}{2\sqrt{2\pi x}} \left[\exp\left(-j\ x + \frac{\pi}{4}\right)\right] \tag{5.6}$$

The other factors used in (5.5) are explained below.

5.3. Divergence Factor

The square root in (5.5) as usual takes positive real, negative imaginary, or zero value. R_1 is a radius of curvature of the diffracted wavefront passing through O^d. It may be calculated from Equation (5.11) of [18] which reads

$$\frac{1}{R_1} = \frac{1}{d_3} + \frac{\kappa}{\sin^2\beta} \left[\frac{1}{d_3}\vec{d}_3 - \frac{1}{d_4}\right]\vec{d}_4 \cdot \hat{n} \tag{5.7}$$

Here β is the angle between tangent $\hat{t}$ and $\vec{d}_4$ (Figure 9). The factor $\sin\beta$ is given by

$$\sin\beta = \left|\sqrt{1 - Q^2}\right| \tag{5.8a}$$

where

$$Q = \frac{1}{Pd_3}\left[(x' - x_1')\frac{\partial g_1}{\partial \phi'} + (y' - y_1')\frac{\partial g_2}{\partial \phi'} + (z' - z_1')\frac{\partial g_3}{\partial \phi'}\right] \tag{5.8b}$$

$$P = +\left[\left(\frac{\partial g_1}{\partial \phi'}\right)^2 + \left(\frac{\partial g_2}{\partial \phi'}\right)^2 + \left(\frac{\partial g_3}{\partial \phi'}\right)^2\right]^{1/2} \tag{5.8c}$$

All the derivatives in (5.8) and in the remainder of this section are evaluated at the diffraction point 0^d, whose coordinates are (x', y', z'). The curvature κ and normal $\hat{n}$ of the curve Γ at 0^d can be calculated from Equation (13.9) of [23]. The results are

$$\kappa = \frac{R}{P^3} \tag{5.9a}$$

$$\hat{n} = \frac{1}{PR}\begin{vmatrix} \hat{x}' & \hat{y}' & \hat{z}' \\ g_2'g_3'' - g_3'g_2'' & g_3'g_1' - g_1'g_3'' & g_1'g_2'' - g_2'g_1'' \\ g_1' & g_2' & g_3' \end{vmatrix} \tag{5.9b}$$

where the prime on g_n' signifies the partial derivative with respect to ϕ' and

$$R = [(g_2'g_3'' - g_3'g_2'')^2 + (g_3'g_1'' - g_1'g_3'')^2 + (g_1'g_2'' - g_2'g_1'')^2]^{1/2} \tag{5.10}$$

Summarizing the results in (5.7) through (5.10), we obtain the final expression for the divergence factor of the diffracted field

$$DFD = \frac{1}{\sqrt{1 + (d_4/R_1)}} = \frac{1}{\sqrt{1 + G}} \tag{5.11}$$

where

$$G = \frac{d_4}{d_3} + \frac{d_4}{P^4(\sin\beta)^2}\left\{\left(\frac{x' - x_1'}{d_3} + \frac{x' - x_2'}{d_4}\right)[g_3'(g_3'g_1'' - g_1'g_3'') - g_2'(g_1'g_2'' - g_2'g_1'')\right.$$

$$+\left(\frac{y' - y_1'}{d_3} + \frac{y' - y_2'}{d_4}\right)[g_1'(g_1'g_2'' - g_2'g_1'') - g_3'(g_2'g_3'' - g_3'g_2'')]$$

$$\left.+\left(\frac{z' - z_1'}{d_3} + \frac{z' - z_2'}{d_4}\right)[g_2'(g_2'g_3'' - g_3'g_2'') - g_1'(g_3'g_1'' - g_1'g_3'')]\right\}$$

5.4. Diffraction Coefficients

The soft and hard Keller's diffraction coefficients D^s and D^h are defined in Equation (5.22) of [18], namely,

$$D^{s,h} = \chi^i \mp \chi^r$$

$$= -\sec\frac{1}{2}(\phi - \phi^i) \pm \sec\frac{1}{2}(\phi + \phi^i) \tag{5.12}$$

The angles ϕ^i and ϕ are shown in Figure 10. Because of the fact that $\hat{N}\cdot\hat{z} > 0$, it can be shown that vector $\hat{t} \times \hat{N}$ is tangent to Σ at O^r, and points away from (not toward) Σ. We calculate ϕ^i and ϕ from the relations

$$\cos\phi^i = \frac{(\text{Proj } \vec{d}_3)\cdot(\hat{t} \times \hat{N})}{|\text{Proj } \vec{d}_3|}(-1) \tag{5.13}$$

$$\cos\phi = \frac{(\text{Proj } \vec{d}_4)\cdot(\hat{t} \times \hat{N})}{|\text{Proj } \vec{d}_4|} \tag{5.14}$$

Here Proj $\vec{d}_3$ is the projection of $\vec{d}_3$ on the plane perpendicular to $\hat{t}$, namely,

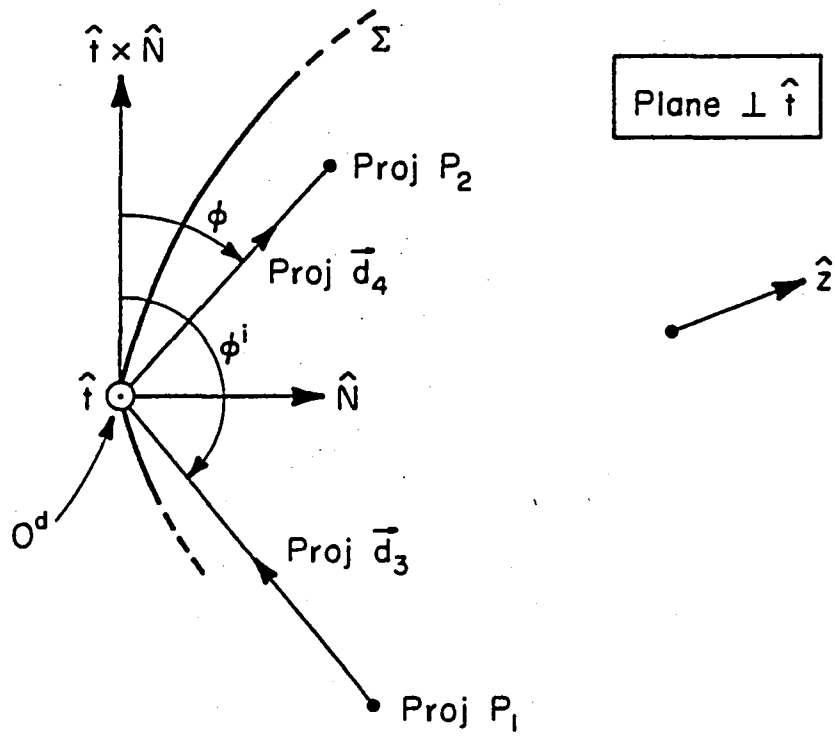

Figure 10. Projection of Figure 9 on a plane perpendicular to tangent $\hat{t}$.

$$\text{Proj } \vec{d}_3 = \vec{d}_3 - (\vec{d}_3 \cdot \hat{t})\hat{t}$$

$$= \hat{x}' S_{31} + \hat{y}' S_{32} + \hat{z}' S_{33} \tag{5.15}$$

where.

$$S_{31} = (x' - x_1') - \frac{d_3 Q}{P} \frac{\partial g_1}{\partial \phi'}$$

$$S_{32} = (y' - y_1') - \frac{d_3 Q}{P} \frac{\partial g_2}{\partial \phi'}$$

$$S_{33} = (z' - z_1') - \frac{d_3 Q}{P} \frac{\partial g_3}{\partial \phi'}$$

Similarly Proj $\vec{d}_4$ is given by

$$\text{Proj } \vec{d}_4 = \hat{x}' S_{41} + \hat{y}' S_{42} + \hat{z}' S_{43} \tag{5.16}$$

where

$$S_{41} = (x_2' - x') - \frac{d_4 Q}{P} \frac{\partial g_1}{\partial \phi'}$$

$$S_{42} = (y_2' - y') - \frac{d_4 Q}{P} \frac{\partial g_2}{\partial \phi'}$$

$$S_{43} = (z_2' - z') - \frac{d_4 Q}{P} \frac{\partial g_3}{\partial \phi'}$$

The normal $\hat{N}$ of the reflector at O^d is given in (4.7). For the present application, it is convenient to change its base vectors to those in the primed coordinate system. The result is

$$\hat{N} = \hat{x}' N_1 + \hat{y}' N_2 + \hat{z}' N_3 \tag{5.17}$$

where

$$N_1 = -\Delta f_x \ , \quad N_2 = -\Delta f_y \ , \quad N_3 = \Delta \tag{5.18}$$

if boundary Γ lies on an elliptical cylinder; and

$$N_1 = -\Delta f_x \tag{5.19a}$$

$$N_2 = -\Delta(-f_y \cos \theta_3 + \sin \theta_3) \tag{5.19b}$$

$$N_3 = -\Delta(f_y \sin \theta_3 - \cos \theta_3) \tag{5.19c}$$

if Γ lies on an elliptical cone. Substitution of (5.15) through (5.19) into (5.13) and (5.14) gives the final formulas for calculating ϕ^i and ϕ:

$$\cos \phi^i = [S_{31}M_1 + S_{32}M_2 + S_{33}M_3][S_{31}^2 + S_{32}^2 + S_{33}^2]^{-1/2} \tag{5.20}$$

$$\cos \phi = [S_{41}M_1 + S_{42}M_2 + S_{43}M_3][S_{41}^2 + S_{42}^2 + S_{43}^2]^{-1/2} \tag{5.21}$$

where

$$M_1 = \frac{1}{P}\left[N_2 \frac{\partial g_3}{\partial \phi'} - N_3 \frac{\partial g_2}{\partial \phi'}\right]$$

$$M_2 = \frac{1}{P}\left[N_3 \frac{\partial g_1}{\partial \phi'} - N_1 \frac{\partial g_3}{\partial \phi'}\right]$$

$$M_3 = \frac{1}{P}\left[N_1 \frac{\partial g_2}{\partial \phi'} - N_2 \frac{\partial g_1}{\partial \phi'}\right]$$

The solutions of ϕ^i and ϕ are subject to the following tests:

(i) ϕ^i takes the value in the range $(0,\pi)$ if $T_3 \geq 0$, and the range $(\pi,2\pi)$ if $T_3 < 0$, where

$$T_3 = (-\text{Proj } \vec{d}_3)\cdot\hat{N} = -S_{31}N_1 - S_{32}N_2 - S_{33}N_3 \tag{5.22}$$

(ii) ϕ takes the value in the range $(0,\pi)$ if $T_4 \geq 0$, and the range $(\pi,2\pi)$ if $T_4 < 0$, where

$$T_4 = (\text{Proj } \vec{d}_4)\cdot\hat{N} = S_{41}N_1 + S_{42}N_2 + S_{43}N_3 \tag{5.23}$$

(iii) If the observation point P_2 is <u>exactly</u> on the incident shadow boundary, then

$$\phi - \phi^i - \pi = 0 \tag{5.24}$$

(iv) If the observation point P_2 is <u>exactly</u> on the reflected shadow boundary, then

$$\phi + \phi^i - \pi = 0 \tag{5.25}$$

When the observation point is exactly on the incident shadow boundary, the first factor χ^i in (5.12) becomes infinite, and causes computational difficulty. A simple remedy is to shift P_2 slightly whenever (5.24) is satisfied. It should be remarked that when P_2 is near but not exactly on the incident shadow boundary, χ^i is large but finite. It does not cause any computational difficulty at the moment. Later on, the diffracted field $\vec{H}^d$ in this case will be modified to become $\vec{H}^D$ by using the uniform asymptotic theory so that the total field $\vec{H}^t$ is correct. Similarly, χ^r in (5.12) becomes infinite if the observation point P_2 falls exactly on the reflected shadow boundary. Hence, we shift P_2 slightly when (5.25) is satisfied.

5.5. Spherical Components of Incident Field

Fields $\vec{H}^i_\beta$ and $\vec{H}^i_\alpha$ in (5.5) are the two spherical components in the directions of $\hat{\beta}^i$ and $\hat{\alpha}^i$ of the incident magnetic field $\vec{H}^i$ evaluated at O^d.

The base vectors $(\hat{\beta}^i, \hat{\alpha}^i)$ are shown in Figure 11 and may be calculated from

$$\hat{\beta}^i = (\hat{\alpha}^i \times \vec{d}_3)/d_3 \tag{5.26a}$$

$$\hat{\alpha}^i = (\hat{t} \times \vec{d}_3)/(d_3 \sin \beta) \tag{5.26b}$$

Then it may be shown that

$$H^i_\beta = \frac{-1}{\sin \beta} [\vec{H}^i(0^d) \cdot \hat{t}]$$

$$= \frac{-1}{P \sin \beta} \left[H_1 \frac{\partial g_1}{\partial \phi'} + H_2 \frac{\partial g_2}{\partial \phi'} + H_3 \frac{\partial g_3}{\partial \phi'} \right] \tag{5.27a}$$

$$H^i_\alpha = \frac{1}{Pd_3 \sin \beta} \left\{ H_1 \left[\frac{\partial g_2}{\partial \phi'} (z' - z'_1) - \frac{\partial g_3}{\partial \phi'} (y' - y'_1) \right] \right.$$

$$+ H_2 \left[\frac{\partial g_3}{\partial \phi'} (x' - x'_1) - \frac{\partial g_1}{\partial \phi'} (z' - z') \right]$$

$$\left. + H_3 \left[\frac{\partial g_1}{\partial \phi'} (y' - y'_1) - \frac{\partial g_2}{\partial \phi'} (x' - x'_1) \right] \right\} \tag{5.27b}$$

Here (H_1, H_2, H_3) are the components of $\vec{H}^i$ in the directions of $(\hat{x}', \hat{y}', \hat{z}')$. They are given by

$$H_1 = H^i_x(0^d) \ , \quad H_2 = H^i_y(0^d) \ , \quad H_3 = H^i_z(0^d) \tag{5.28a}$$

if Γ lies on elliptical cylinder; and

$$\begin{cases} H_1 = H^i_x(0^d) \\ H_2 = -\cos \theta_3 \, H^i_y(0^d) - \sin \theta_3 \, H^i_z(0^d) \\ H_3 = \sin \theta_3 \, H^i_y(0^d) - \cos \theta_3 \, H^i_z(0^d) \end{cases} \tag{5.28b}$$

if Γ lies on elliptical cone.

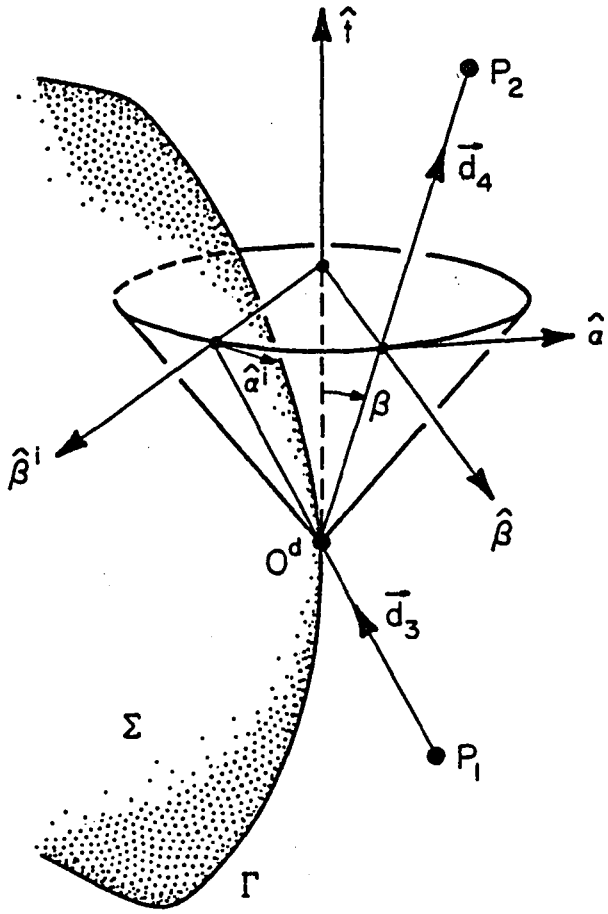

Figure 11. Spherical base vectors $(\hat{\beta}^i, \hat{\alpha}^i)$ and $(\hat{\beta}, \hat{\alpha})$.

5.6. Rectangular Components of Diffracted Field

The diffracted field $\vec{H}^d$ calculated from (5.5) must be eventually expressed in terms of rectangular components in the directions of $(\hat{x},\hat{y},\hat{z})$, so that it can be conveniently superimposed with the geometrical optics field $\vec{H}^g$ in Section 4. In (5.5), the two spherical base vectors $(\hat{\beta},\hat{\alpha})$ (Figure 11) may be calculated from

$$\hat{\beta} = (\hat{\alpha} \times \vec{d}_4)/d_4 \tag{5.29a}$$

$$\hat{\alpha} = (\hat{t} \times \vec{d}_4)/(d_4 \sin \beta) \tag{5.29b}$$

The diffracted field expressed in terms of the primed base vectors are

$$\vec{H}^d(P_2) = \hat{x}'h_1 + \hat{y}'h_2 + \hat{z}'h_3 \tag{5.30}$$

where

$$h_n = [D^h \beta_n H^i_\beta + D^s \alpha_n H^i_\alpha]\, g(kd_4)\, (DFD) \frac{1}{\sin \beta} \quad , \qquad n = 1,2,3$$

$$\alpha_1 = \frac{1}{Pd_4 \sin \beta}\left[\frac{\partial g_3}{\partial \phi'}(y' - y_2') - \frac{\partial g_3}{\partial \phi'}(z' - z_2')\right]$$

$$\alpha_2 = \frac{1}{Pd_4 \sin \beta}\left[\frac{\partial g_1}{\partial \phi'}(z' - z_2') - \frac{\partial g_3}{\partial \phi'}(x' - x_2')\right]$$

$$\alpha_3 = \frac{1}{Pd_4 \sin \beta}\left[\frac{\partial g_2}{\partial \phi'}(x' - x_2') - \frac{\partial g_1}{\partial \phi'}(y' - y_2')\right]$$

$$\beta_1 = \frac{1}{d_4}[\alpha_3(y' - y_2') - \alpha_2(z' - z_2')]$$

$$\beta_2 = \frac{1}{d_4}[\alpha_1(z' - z_2') - \alpha_3(x' - x_2')]$$

$$\beta_3 = \frac{1}{d_4}[\alpha_2(x' - x_2') - \alpha_1(y' - y_2')]$$

The factor g is defined in (5.6), DFD in (5.11), and sin β in (5.8). The final expressions for the diffracted field in the umprimed coordinate system are as follows:

$$\vec{H}^d(P_2) = \hat{x}H_x^d + \hat{y}H_y^d + \hat{z}H_z^d \tag{5.31a}$$

where

$$H_x^d = h_1 \ , \quad H_y^d = h_2 \ , \quad H_z^d = h_3 \tag{5.31b}$$

if Γ lies on an elliptical cylinder; and

$$\begin{cases} H_x^d = h_1 \\ H_y^d = -h_2 \cos\theta_3 - h_3 \sin\theta_3 \\ H_z^d = h_2 \sin\theta_3 - h_3 \cos\theta_3 \end{cases} \tag{5.31c}$$

if Γ lies on an elliptical cone. The corresponding diffracted electric field $\vec{E}^d$ at P_2 is calculated from

$$\vec{E}^d(P_2) = 120\pi \ d_4^{-1}[\vec{H}^d(P_2) \times \vec{d}_4] \tag{5.32}$$

5.7. Detour Parameter

The diffracted field $\vec{H}^d$ calculated from (5.5) is not valid when observation point P_2 is near the reflected shadow boundary which is defined by (5.25). To detect if P_2 is indeed so, we may calculate the so-called "detour parameter" of the reflected field (Section VI of [18]).

$$\xi = \varepsilon[k(d_3 + d_4 - d_1 - d_2)]^{1/2} \tag{5.33}$$

Here ε is the shadow indicator of the reflected field defined by

$$\varepsilon = \begin{cases} +1, \text{ if } P_2 \text{ is in the shadow side of the reflected field} \\ \\ -1, \text{ if } P_2 \text{ is in the lit side of the reflected field} \end{cases}$$

It may be shown that

$$\varepsilon = \mathrm{Sgn}\left[-\cos \frac{1}{2} (\phi + \phi^i)\right] \tag{5.34}$$

The square root in (5.33) takes positive real, negative imaginary, or zero value. When the caustic of the reflected field falls on the reflected shadow boundary, ξ is imaginary; otherwise, ξ is always real. Detour parameter ξ in (5.33) becomes zero when P_2 is exactly on the reflected shadow boundary, because the diffraction point O^d and reflection point O^r coincide (Figure 2). Following the numerical study in [24], we take

$$|\xi| = 2 \tag{5.35}$$

as on the on-set point. Thus, if $|\xi| > 2$, P_2 is considered to be away from the reflected shadow boundary, and the diffracted field $\vec{H}^d$ in (5.5) is valid. If $|\xi| < 2$, P_2 is considered to be near the reflected shadow boundary, and we must replace $\vec{H}^d$ by $\vec{H}^D$ as stated in (2.9).

When ξ is small, $(d_3 + d_4)$ in (5.33) is nearly equal to $(d_1 + d_2)$. In many practical problems, the reflection point O^r and diffraction point O^d may not be determined with great precision. Thus, when ξ is small, a direct computation of ξ from (5.33) can have a numerical accuracy problem. To circumvent this possible problem, we have given below an alternative formula for ξ when its value is small:

$$\xi \approx -\left[\cos \frac{1}{2} (\phi + \phi^i)\right] \sin \beta \sqrt{2k} \frac{\sqrt{d_4[1 + (d_4/R_1)]}}{\sqrt{1 + (d_2/R_1^r)}\sqrt{1 + (d_2/R_2^r)}}$$

$$= \left[- \cos \frac{1}{2} (\phi + \phi^i)\right] \sin \beta \sqrt{2k} \frac{(DF)\sqrt{d_4}}{(DDF)} , \quad \text{if } |\xi| \to 0 \qquad (5.36)$$

where (DF) of the reflected field is defined in (4.8), and (DDF) of the diffracted field in (5.11). The derivation of (5.36) is given in Appendix A of [14]. In all of the following computations, we use (5.33) if $|\xi| > 2$, and (5.36) if $|\xi| < 2$.

5.8. Uniform Asymptotic Theory

We shall calculate $\vec{H}^D$ by the UAT developed in [14], [19], [21]. The formula reads

$$\vec{H}^D(P_2) = \vec{H}^d(P_2) + \left[F(\xi) - \hat{F}(\xi) - \frac{1}{2}(1 - \varepsilon)\right] \vec{H}^r(P_2) \qquad (5.37)$$

where F is a Fresnel integral defined by

$$F(z) = \pi^{-1/2} e^{j\pi/4} \int_z^\infty e^{-jt^2} dt \qquad (5.38a)$$

and

$$\hat{F}(z) = \frac{1}{2z\sqrt{\pi}} \exp\left[-j \left(z^2 + \frac{\pi}{4}\right)\right] \qquad (5.38b)$$

The factor $(1 - \varepsilon)/2$ in (5.37) is one if P_2 is in the lit region of the reflected field, and zero, if P_2 is in the shadow. As expected, $\vec{H}^D$ reduces to $\vec{H}^d$ when P_2 is away from the reflected shadow boundary. This is because of the fact that for $|\xi| \to \infty$,

$$[F(\xi) - \hat{F}(\xi)] \sim \frac{1}{2}(1 - \varepsilon) \tag{5.39}$$

When P_2 is near or on the reflected shadow boundary, $\vec{H}^D$ in (5.37) is always finite, and compensates exactly for the discontinuity in $\vec{H}^g$ so that the total field $\vec{H}^t$ in (2.9) is everywhere continuous.

6. SECONDARY PATTERN COMPUTATION

6.1. Aperture Field Theory

Refer to Figure 3. From field equivalence principles, solutions for the far field may be obtained knowing the tangential fields at Σ_a. The aperture plane Σ_a is taken to be perpendicular to the z-axis.

Let us denote the tangential electric and magnetic fields at Σ_a by $\vec{E}_a$ and $\vec{H}_a$, respectively. The field may be determined by using vector potentials [25]. However, it is more convenient to express the far field directly in terms of the aperture fields. Let us define the following vector quantities:

$$\vec{f}(u,v) = \iint_{\Sigma_a} \vec{E}_a(x,y)\, e^{jk(ux+vy)} dxdy \tag{6.1}$$

$$\vec{g}(u,v) = \iint_{\Sigma_a} \vec{H}_a(x,y)\, e^{jk(ux+vy)} dxdy \tag{6.2}$$

where

$$u = \sin\theta \cos\phi \tag{6.3}$$

$$v = \sin\theta \sin\phi \tag{6.4}$$

$$k = 2\pi/\lambda$$

θ,ϕ = spherical coordinates of far field point

Since the aperture fields are tangent to $\hat{z}$, let

$$\vec{f} = f_x \hat{x} + f_y \hat{y} \tag{6.5}$$

$$\vec{g} = g_x \hat{x} + g_y \hat{y} \tag{6.6}$$

From each of the 3 equivalence principle formulations, three different expressions arise for E_θ and E_ϕ of the far field, namely,

(1) using $\vec{E}_a$ and $\vec{H}_a$

$$E_\theta = \frac{jke^{-jkr}}{4\pi r}\left[f_x\cos\phi + f_y\sin\phi + Z_o\cos\theta\,(g_y\cos\phi - g_x\sin\phi)\right] \tag{6.7a}$$

$$E_\phi = \frac{jke^{-jkr}}{4\pi r}\left[\cos\theta\,(f_y\cos\phi - f_x\sin\phi) - Z_o(g_y\sin\phi + g_x\cos\phi)\right] \tag{6.7b}$$

(2) using $\vec{H}_a$

$$E_\theta = \frac{jk\,Z_o\,e^{-jkr}\cos\theta}{2\pi r}(g_y\cos\phi - g_x\sin\phi) \tag{6.8a}$$

$$E_\phi = \frac{jk\,Z_o\,e^{-jkr}}{2\pi r}(g_y\sin\phi + g_x\cos\phi) \tag{6.8b}$$

(3) using $\vec{E}_a$

$$E_\theta = \frac{jke^{-jkr}}{2\pi r}(f_x\cos\phi + f_y\sin\phi) \tag{6.9a}$$

$$E_\phi = \frac{jke^{-jkr}\cos\theta}{2\pi r}(f_y\cos\phi - f_x\sin\phi) \tag{6.9b}$$

This method suits large apertures (in terms of λ) because the Fourier transforms of the aperture field, $\vec{f}$ and $\vec{g}$, are highly peaked in the frequency domain.

This method is exact if the fields at Σ_a were known everywhere. However, one must truncate Σ_a to finite dimensions in order to employ the FFT.

6.2 Fast Fourier Transform

To employ the FFT subroutine, the integrals (6.1) and (6.2) must be rearranged so that the form of the integral matches the definition given by the documentation of the FFT subroutine. For this particular 2-dimensional FFT subroutine, the function being considered is assumed to be periodic in x and y with period 1 in x and y. Hence, the aperture grid as shown in Figure 12 must be scaled accordingly.

Many manipulations are required in order to use the FFT. These manipulations are carried out for f_x. Similarly, this can be applied to obtain f_y, g_x, and g_y. From (6.1) and (6.5)

$$f_x(u,v) = \int_{y_1}^{y_2}\int_{x_1}^{x_2} E_{ax}(x,y)\, e^{jk(ux+vy)}dxdy \tag{6.10}$$

where E_{ax} is the x-component of $\vec{E}_a(x,y)$ in (6.1). Using the substitutions

$$\underline{\overline{X}} = (x-x_1)/(x_2-x_1) \tag{6.11}$$

$$\underline{\overline{Y}} = (y-y_1)/(y_2-y_1), \tag{6.12}$$

(6.11) becomes

$$f_x(u,v) = K_1 \int_0^1\int_0^1 E_{ax}\left(x_1+\underline{\overline{X}}(x_2-x_1),\ y_1+\underline{\overline{Y}}(y_2-y_1)\right) \cdot$$

$$e^{j\frac{2\pi}{\lambda}\left(u(x_2-x_1)\underline{\overline{X}} + v(y_2-y_1)\underline{\overline{Y}}\right)} d\underline{\overline{X}}d\underline{\overline{Y}} \tag{6.13}$$

where

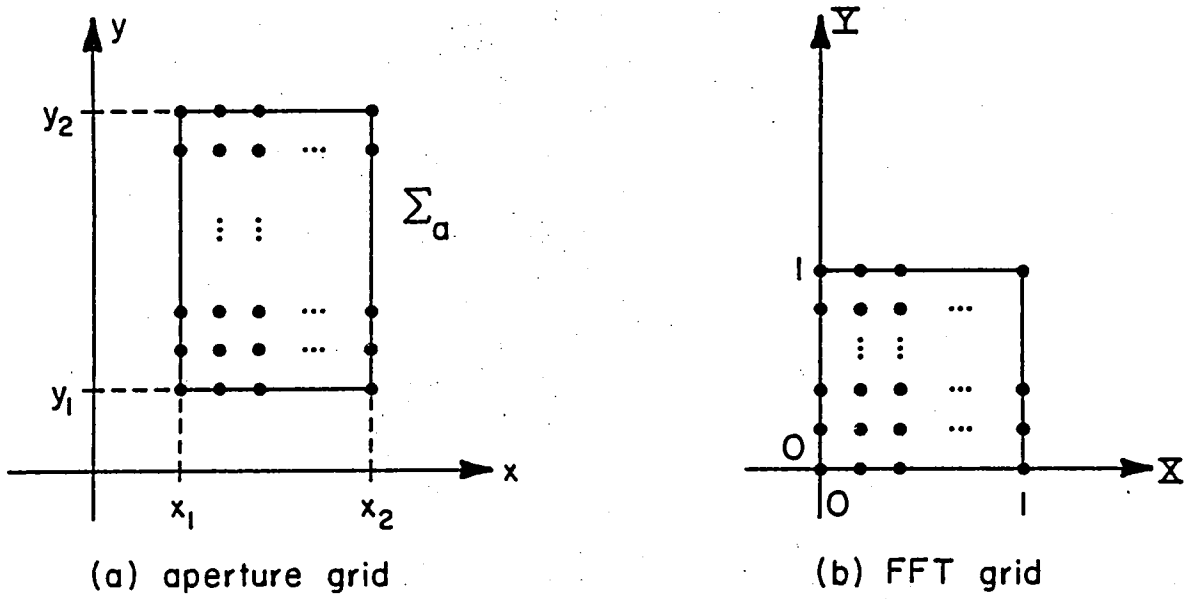

Figure 12. Aperture grid $\sum_a$ and FFT grid.

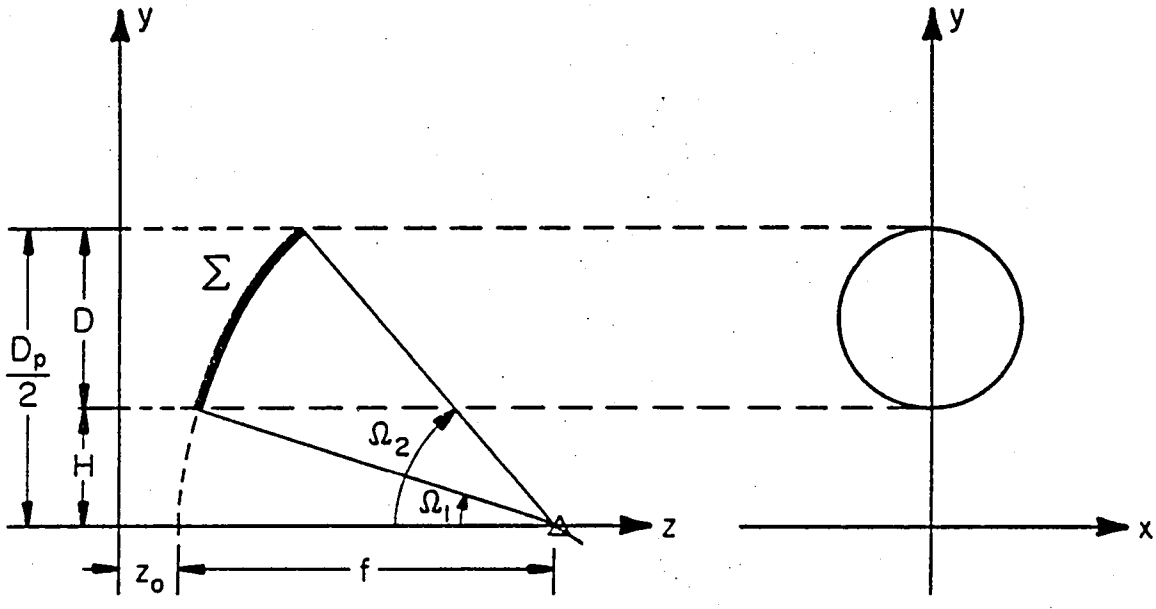

Figure 13. An offset parabolic reflector.

$$K_1 = (x_2-x_1)(y_2-y_1)\, e^{j\frac{2\pi}{\lambda}(ux_1+vy_1)} \tag{6.14}$$

The expression $E_{ax}\left(x_1+(x_2-x_1)\underline{\overline{X}},\ y_1+(y_2-y_1)\underline{\overline{Y}}\right)$ under the integral may be interpreted as $E_{ax}(x,y)$ scaled to $F(a,b)$ where $0\leq a\leq 1$ and $0\leq b\leq 1$ (see Figure 12). $F(a,b)$ may be approximated by

$$F(a,b) = \sum_{n=N_1}^{N_2} \sum_{m=M_1}^{M_2} C_{mn} e^{j2\pi(m\underline{\overline{X}}+n\underline{\overline{Y}})}\ , \tag{6.15}$$

where C_{mn} are the Fourier coefficients obtained using the FFT subroutine. For a 32x32 FFT,

$$N_1 = M_1 = -15$$

$$N_2 = M_2 = 16$$

From (6.13) and (6.15),

$$f_x(u,v) = K_1 \int_0^1 \int_0^1 \sum_{n=N_1}^{N_2} \sum_{m=M_1}^{M_2} C_{mn} e^{j\frac{2\pi}{\lambda}\left[\left(m\lambda+u(x_2-x_1)\right)\underline{\overline{X}} + \left(n\lambda+v(y_2-y_1)\right)\underline{\overline{Y}}\right]}\, d\underline{\overline{X}}\, d\underline{\overline{Y}} \tag{6.16}$$

Interchanging the summation and integral signs and noting that

$$\int_0^1 e^{j\frac{2\pi}{\lambda}cx}\, dx = \frac{\sin(\frac{\pi c}{\lambda})}{\frac{\pi c}{\lambda}}\ e^{\frac{j\pi c}{\lambda}} \tag{6.17}$$

the expression for f_x is

$$f_x(u,v) = K \sum_{n=N_1}^{N_2} \sum_{m=M_1}^{M_2} C_{mn} e^{j\frac{\pi}{\lambda}(m+n)}\ \frac{\sin\left[\frac{\pi}{\lambda}\left(m\lambda+u(x_2-x_1)\right)\right]\sin\left[\frac{\pi}{\lambda}\left(n\lambda+v(y_2-y_1)\right)\right]}{\frac{\pi\left(m\lambda+u(x_2-x_1)\right)}{\lambda}\ \frac{\pi\left(n\lambda+v(y_2-y_1)\right)}{\lambda}} \tag{6.18}$$

where

$$K = (x_2-x_1)(y_2-y_1)e^{j\frac{\pi}{\lambda}\left(u(x_1+x2) + v(y1+y2)\right)} \tag{6.19}$$

In summary, to evaluate the integral (6.10), we first calculate $\{C_{mn}\}$ of (6.15) by FFT and then calculate $f_x(u,v)$ via (6.18).

6.3 Gain Normalization

The secondary pattern is usually decomposed into two orthogonal polarizations. Following Ludwig's definition 3 [26], the following unitary polarization vectors are introduced.

$$\hat{R} = \hat{\theta}(ae^{j\psi}\cos\phi + b\sin\phi) + \hat{\phi}(-ae^{j\psi}\sin\phi + b\cos\phi) \tag{6.20}$$

$$\hat{C} = \hat{\theta}(ae^{-j\psi}\sin\phi - b\cos\phi) + \hat{\phi}(ae^{-j\psi}\cos\phi + b\sin\phi) \tag{6.21}$$

Let the secondary pattern be expressed as

$$\vec{E} = \frac{e^{-jkr}}{r}\left[\hat{\theta}\ U_\theta + \hat{\phi}\ U_\phi\right] \tag{6.22}$$

The reference-polarization and cross-polarization expressions of $\vec{E}$ are

$$\text{Reference-pol of } \vec{E} = \left(\vec{E}\cdot(\hat{R}^*)^*\right) \tag{6.23a}$$

$$\text{Cross-pol of } \vec{E} = \left(\vec{E}\cdot(\hat{C}^*)^*\right) \tag{6.23b}$$

The second conjugate operation in (6.23) results from the change in direction of the field after being reflected by the reflector.

The directivity for the reference polarization is defined by

$$D_R\ (\theta,\phi) = \frac{4\pi\ |\vec{E}\cdot\hat{R}|^2/Z_o}{P_{inc}} \tag{6.24}$$

Similarly, the directivity for the cross polarization is defined by

$$D_C\ (\theta,\phi) = \frac{4\pi\ |\vec{E}\cdot\hat{C}|^2/Z_o}{P_{inc}} \tag{6.25}$$

where P_{inc} is the incident power radiated from the feed. Noting that e^{-jkr}/r factor is common in both the secondary pattern (6.22) and the incident radiated field (3.6) the directivity formulas are

$$D_R(\theta,\phi) = \frac{4\pi\ |U_\theta(ae^{j\psi}\cos\phi + b\sin\phi) + U_\phi(-ae^{j\psi}\sin\phi + b\cos\phi)|^2}{Z_o\ P_{inc}} \tag{6.26}$$

$$D_C(\theta,\phi) = \frac{4\pi\ |U_\theta(ae^{-j\psi}\sin\phi - b\cos\phi) + U_\phi(ae^{-j\psi}\cos\phi + b\sin\phi)|^2}{Z_o\ P_{inc}} \tag{6.27}$$

Thus, for any feed polarization (a,b,ψ), (6.26) and (6.27) give the reference and cross-polarization directivities.

7. NUMERICAL EXAMPLES

The present aperture integration method for calculating the secondary pattern of a reflector entails the following steps:

(i) Input the reflector geometry, eq. (2.1), and the boundary description.

(ii) Input the feed pattern as described in eq. (3.4).

(iii) Calculate GO contribution to the aperture field.

(iv) Calculate edge-diffraction contribution to the aperture field. Use either UAT [14] or UTD [15] for aperture grid points near the shadow boundary.

(v) Use the FFT, eq. (6.15), to obtain the far field.

(vi) Decompose the far field pattern into reference-pol and cross-pol components using eq. (6.23).

(vii) Use eqs. (6.26) and (6.27) to obtain the reference and cross-polarization directivities.

In this section, we shall present some numerical results to establish the numerical accuracy of the present method. Near field, far field and scan data for a large reflector are presented.

7.1. Effects of Aperture Grid Size and Location on Secondary Pattern

The aperture field theory used to determine the secondary pattern is exact if the tangential fields are known everywhere on the aperture plane Σ_a. When employing the FFT, Σ_a is truncated. To minimize the amount of computer time spent, the size of Σ_a should be as small as possible while capturing almost all of the field. To this end, a study of varying the aperture grid size and location of Σ_a was performed to determine their effects on the secondary pattern.

The reflector used for this study is an offset parabolic reflector (see Figure 13) with typical f/D_p and f/D values:

$$\frac{f}{D_p} = 0.40, \ \frac{f}{D} = 1.00 \tag{7.1}$$

The corresponding values of Ω_1, Ω_2, and H are

$$\Omega_1 = 14.25° \tag{7.2a}$$

$$\Omega_2 = 64.01° \tag{7.2b}$$

$$H = 0.25D \tag{7.2c}$$

The reflector is being illuminated by a $\hat{y}_f$-polarized feed at focus with 10 dB feed taper. Assuming $(\cos\theta)^q$ type patterns, eq. (3.5), the E- and H-plane feed patterns are given by

$$U_E(\theta) = (\cos\theta)^{11.82} \tag{7.3a}$$

$$U_H(\theta) = (\cos\theta)^{11.82} \tag{7.3b}$$

Refer to Figure 14. Let the aperture plane Σ_a be located a distance L away from the focal plane. The focal plane is located at $z = f$. Plots of the tangential components of the aperture field along two cuts of Σ_a are obtained as the distance L is varied. These two cuts are

x-cut: $y = H + 0.5D, \ z = f + L$

y-cut: $x = 0 \qquad , \ z = f + L$

The diameter of this test reflector is 50λ. Due to the choice of feed polarization, only the y-component of the electric field, E_y, is plotted. Figures 15(a)-(c) are plots of $|E_y|$ for a x-cut for $L = 0$, 10λ, and 20λ,

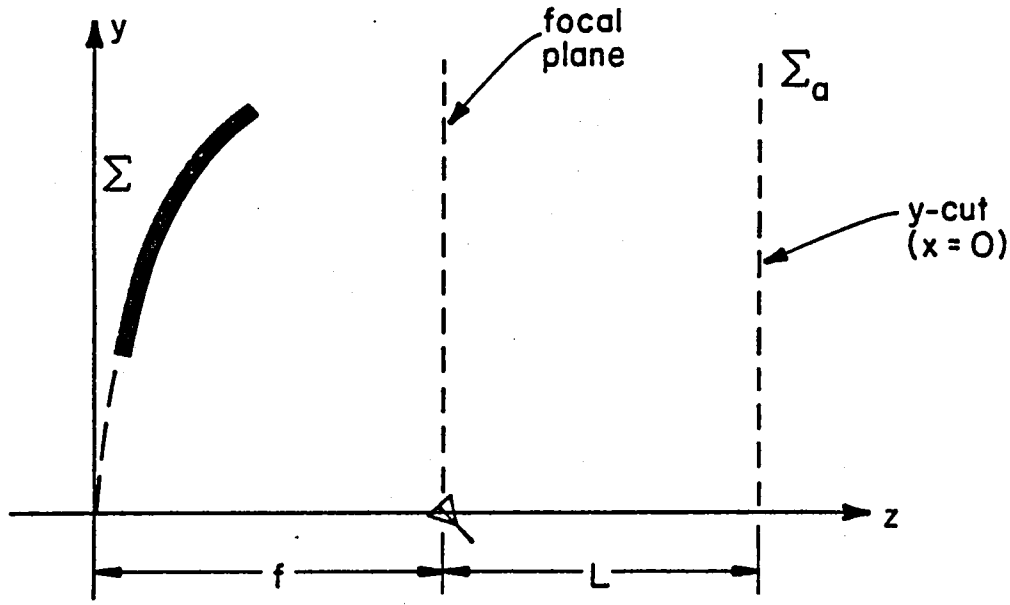

(a) y-cut

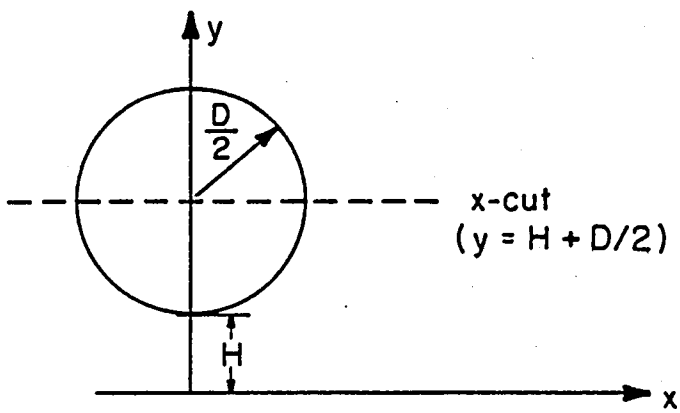

(b) x-cut

Figure 14. Two cuts of aperture plane Σ_a at distance L away from focal plane.

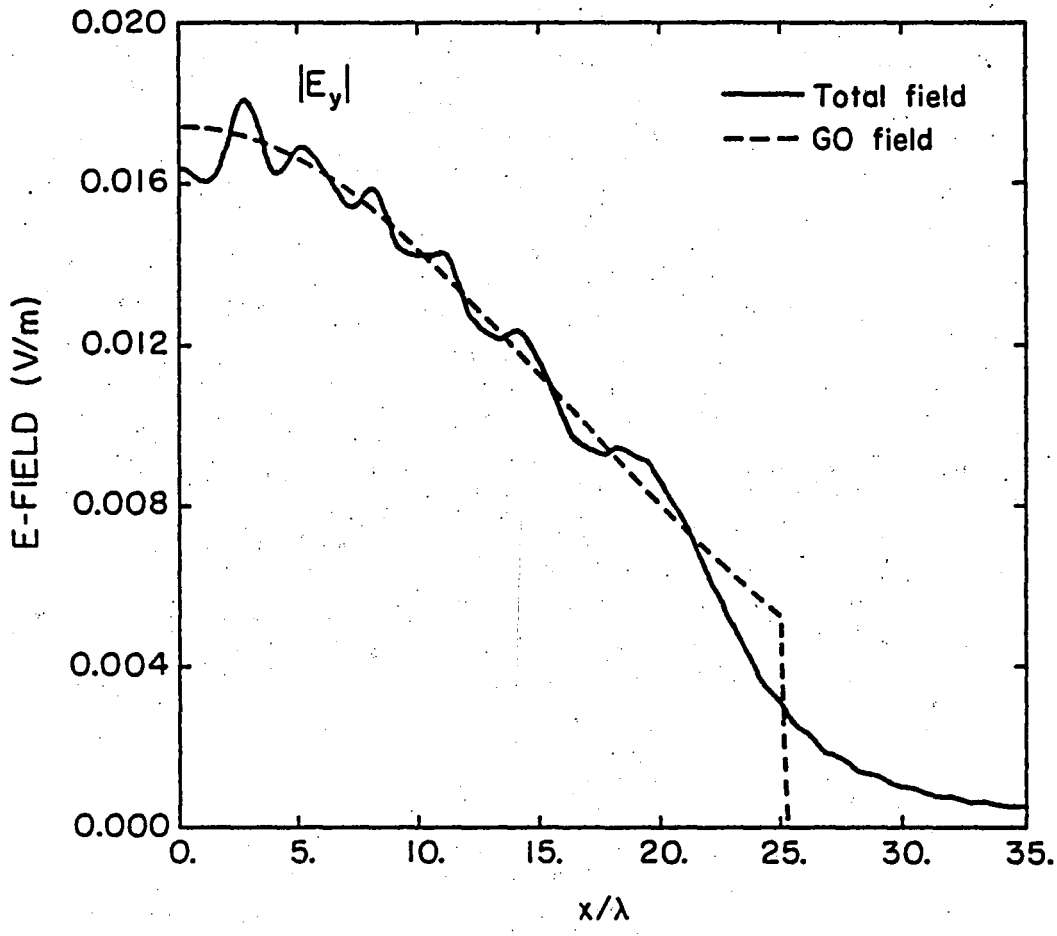

Figure 15a. $|E_y|$ for a x-cut, L = 0

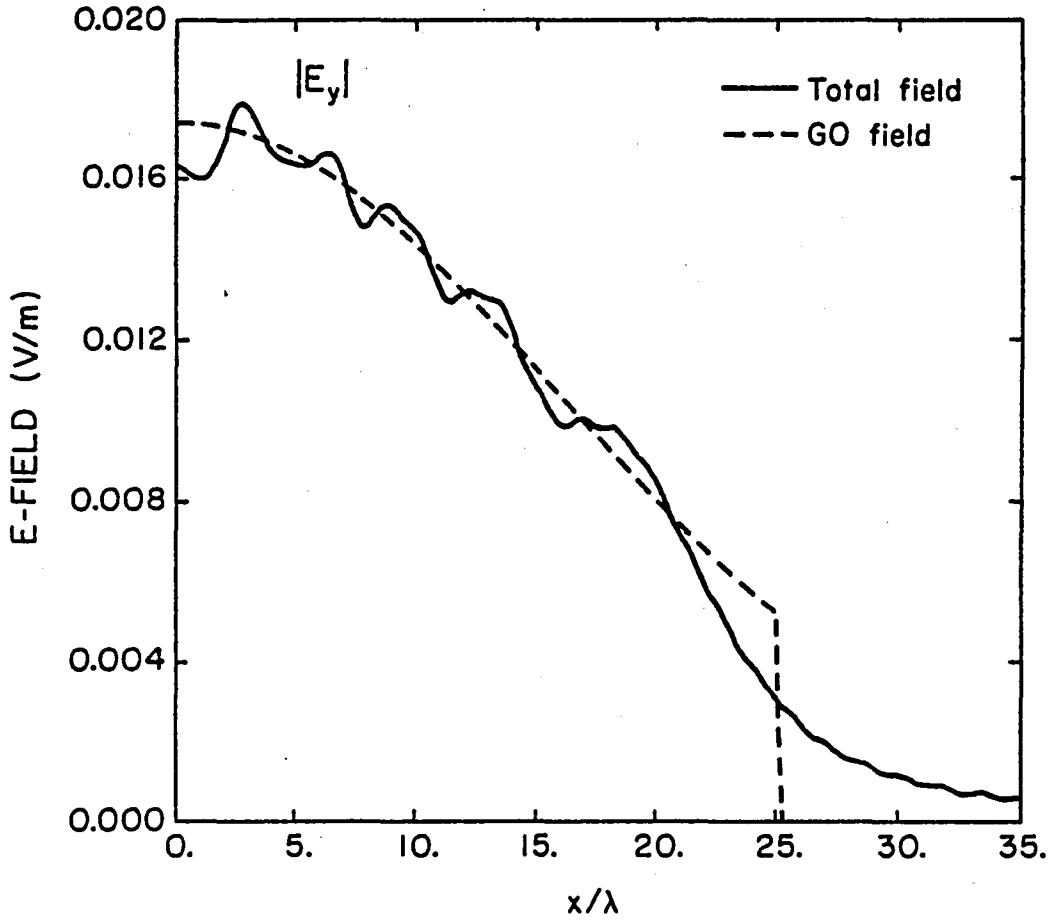

Figure 15b. $|E_y|$ for a x-cut, L = 10λ

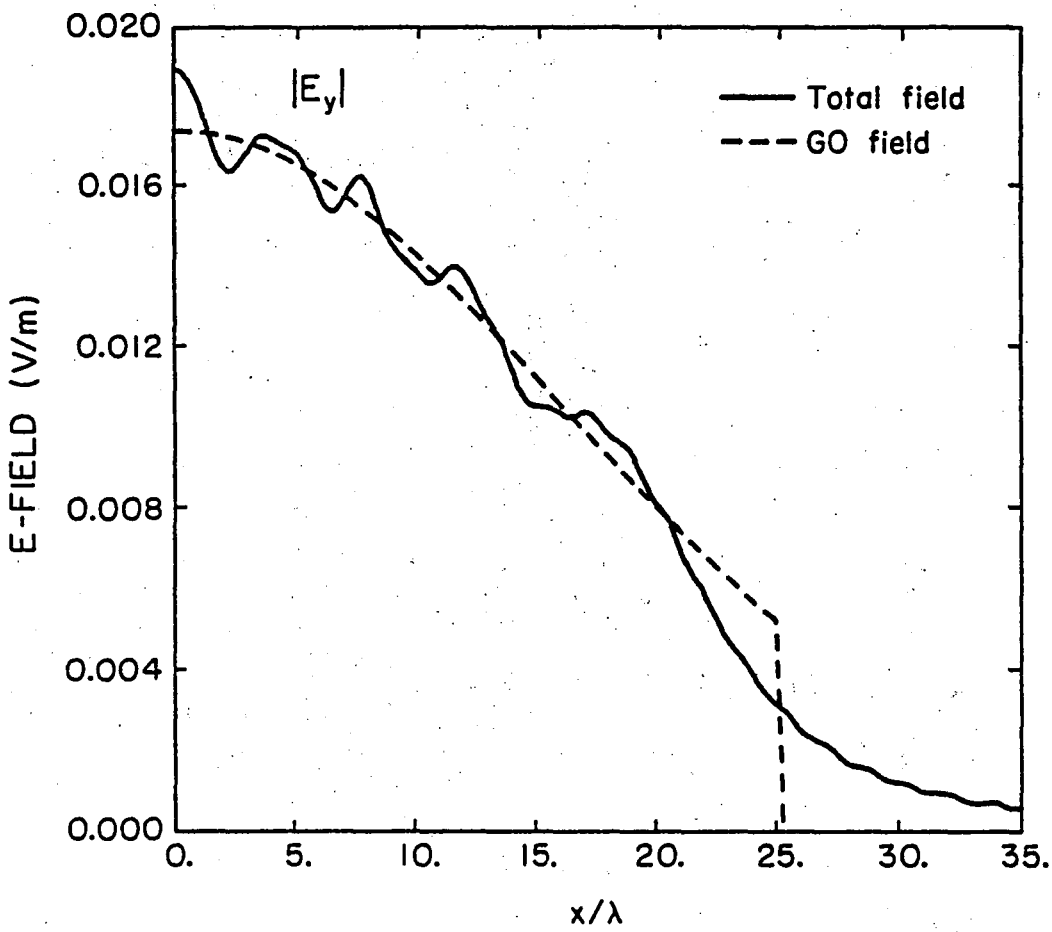

Figure 15c. $|E_y|$ for a x-cut, L = 20λ

respectively. Figures 16(a)-(c) are plots of $|E_y|$ for a y-cut for L = 0, 10λ, and 20λ, respectively.

From Figures 15(a)-(c) and 16(a)-(c), note that the aperture field does not spread as L increases. This is so because the feed is at the focus. To demonstrate that the aperture field does spread as L increases, let's move the feed toward the reflector along $\hat{z}_f$ by an amount d_f (see Figure 17). Figures 18(a)-(c) are plots of $|E_y|$ for a x-cut for $d_f = 2\lambda$ at L = 0, 10λ, and 20λ, respectively. Figures 19(a)-(c) are for the y-cut. Figures 18(a)-(c) and 19(a)-(c) show a slight increase of $|E_y|$ for grid points near the edge of the aperture grid. Also note that the width of the region where the GO field is nonzero increased when L is increased. Thus, to minimize the field strength for a fixed size of Σ_a, L = 0 was chosen. Let the aperture grid be W by W. Choosing the criterion that the field at the edge of Σ_a is at least 20 dB below the maximum field value on Σ_a, W = 1.14D centered at the midpoint of the projected aperture was chosen.

7.2 DBS Antenna

A direct broadcast satellite (DBS) antenna was designed by Lee et al. [27]. Pattern computation programs using the Jacobi-Bessel series technique [4] were developed by Y. Rahmat-Samii. A parabolic reflector was used and it is described by

$$D = \text{dish diameter} = 108.148\lambda \tag{7.4a}$$

$$f = \text{focal length} = 94.867\lambda \tag{7.4b}$$

$$H = \text{offset height} = 16.865\lambda \tag{7.4c}$$

The feed is located at the focus and the primary pattern, eq. (34), is described by

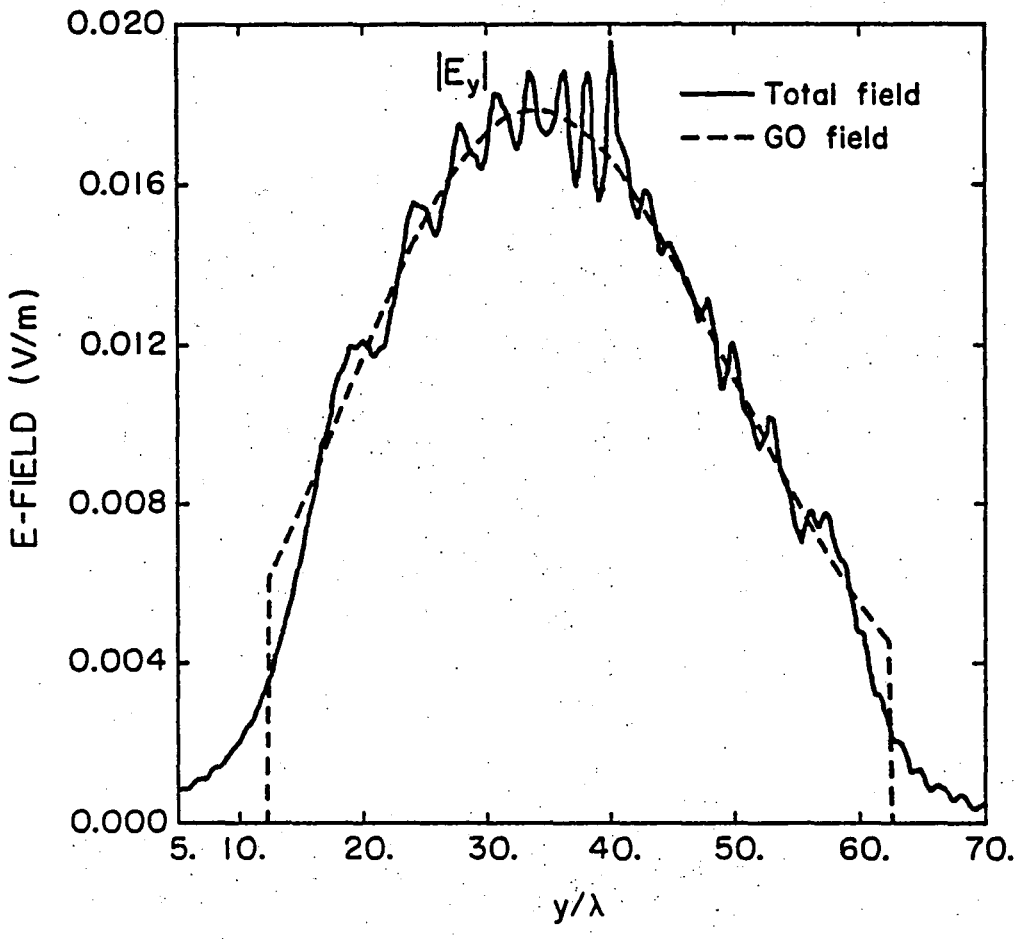

Figure 16a. $|E_y|$ for a y-cut, L = 0

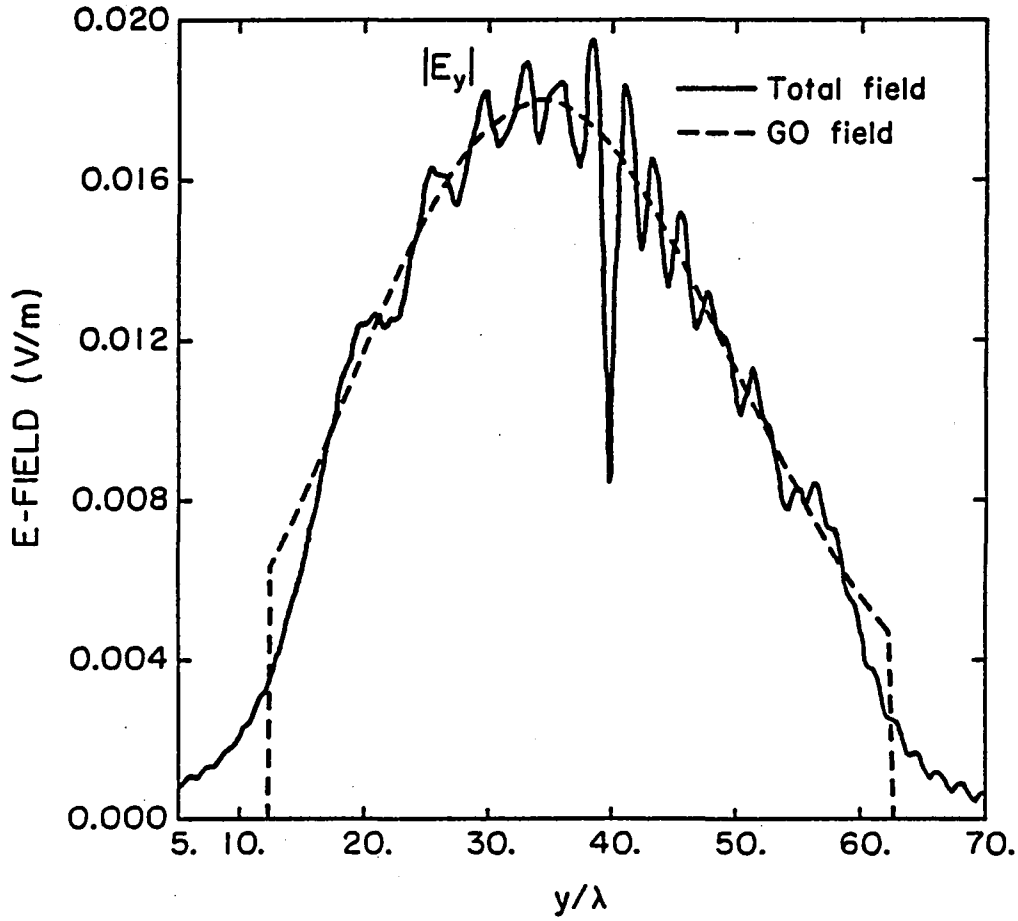

Figure 16b. $|E_y|$ for a y-cut, L = 10λ

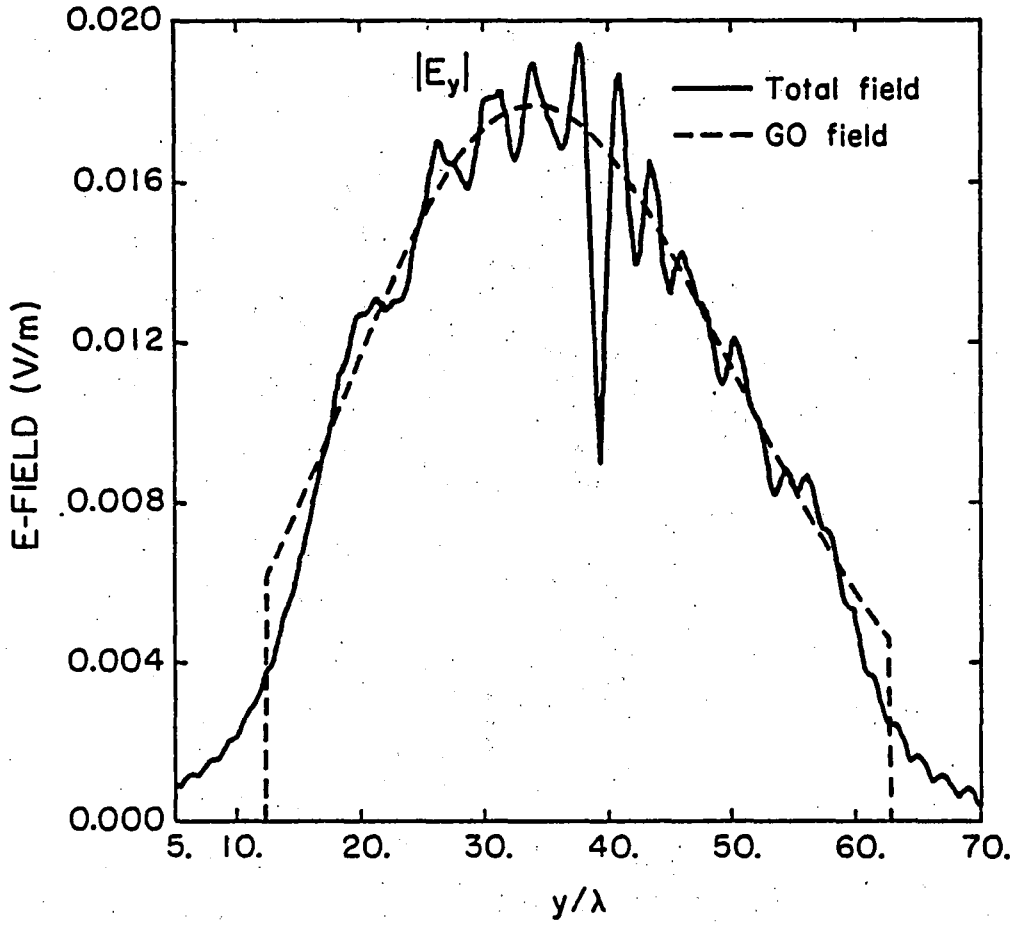

Figure 16c. $|E_y|$ for a y-cut, L = 20λ

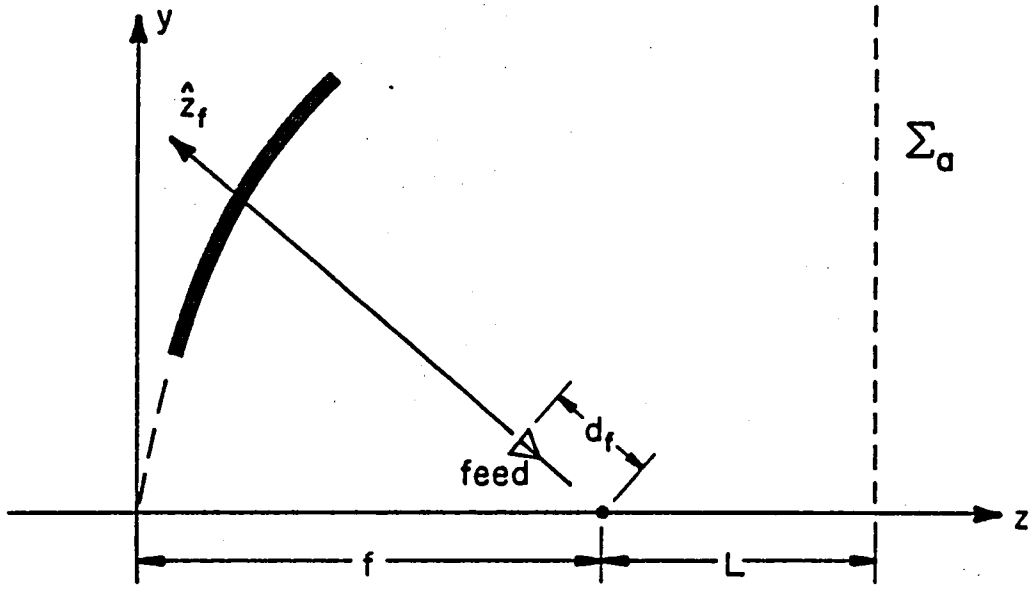

Figure 17. Feed located d_f away from focus along $\hat{z}_f$.

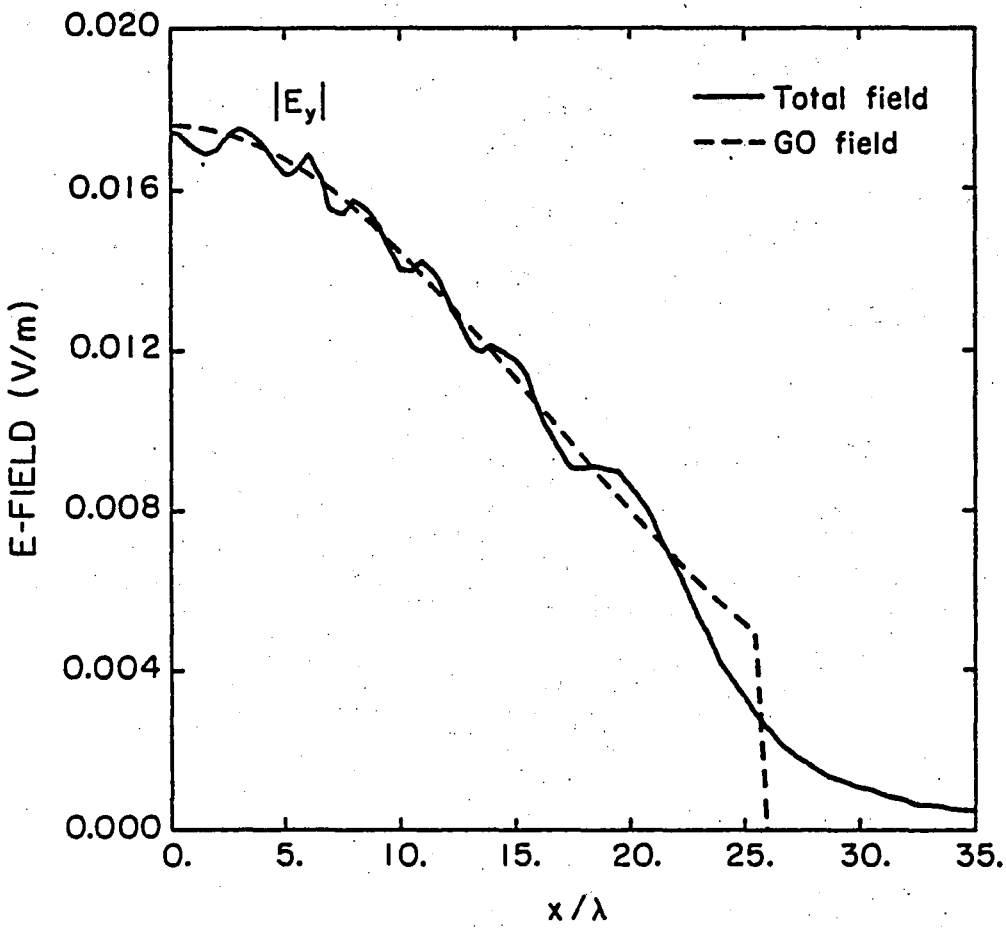

Figure 18a. $|E_y|$ for a x-cut, $d_f = 2\lambda$, $L = 0$.

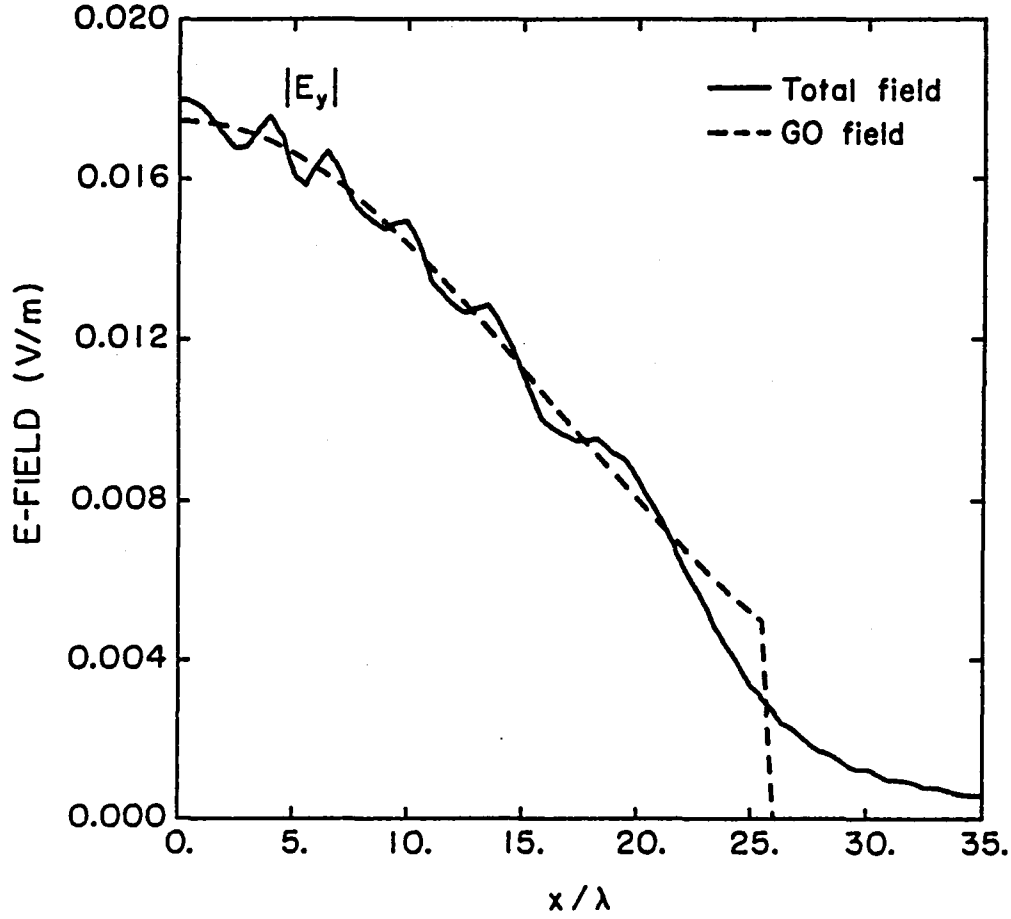

Figure 18b. $|E_y|$ for a x-cut, $d_f = 2\lambda$, $L = 10\lambda$.

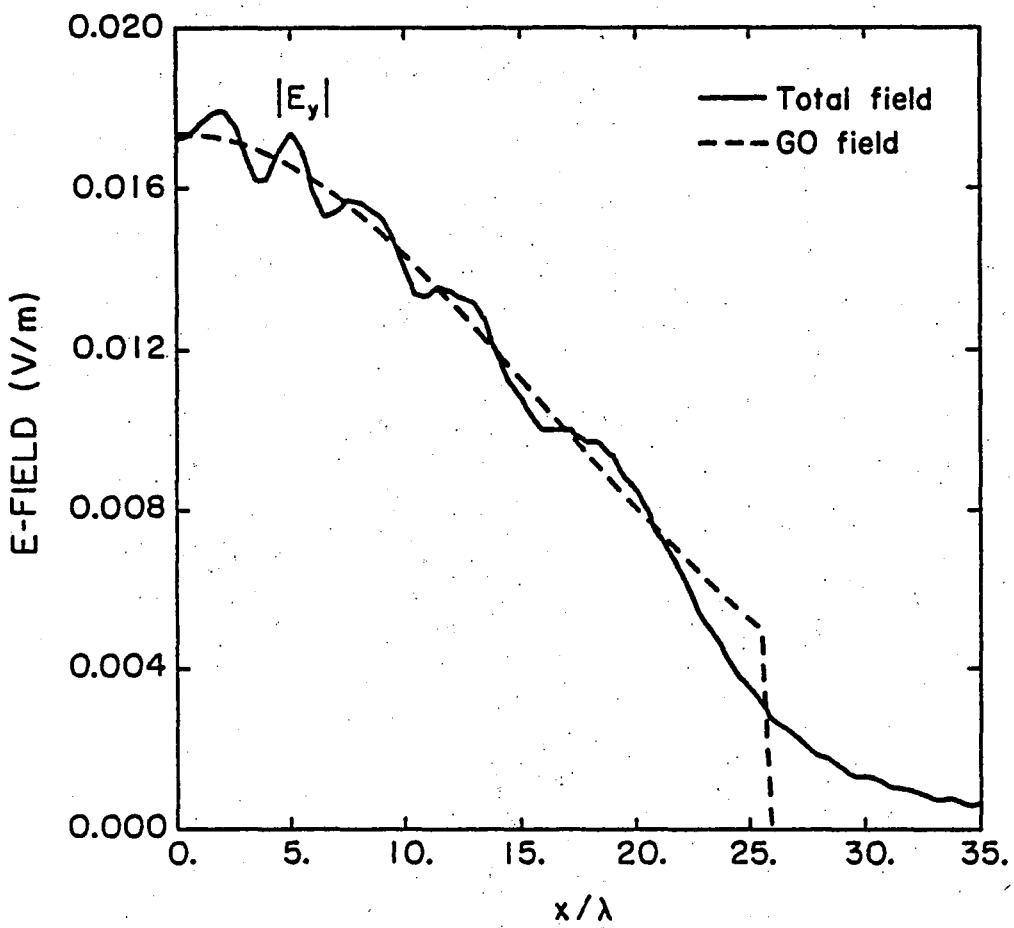

Figure 18c. $|E_y|$ for a x-cut, $d_f = 2\lambda$, $L = 20\lambda$.

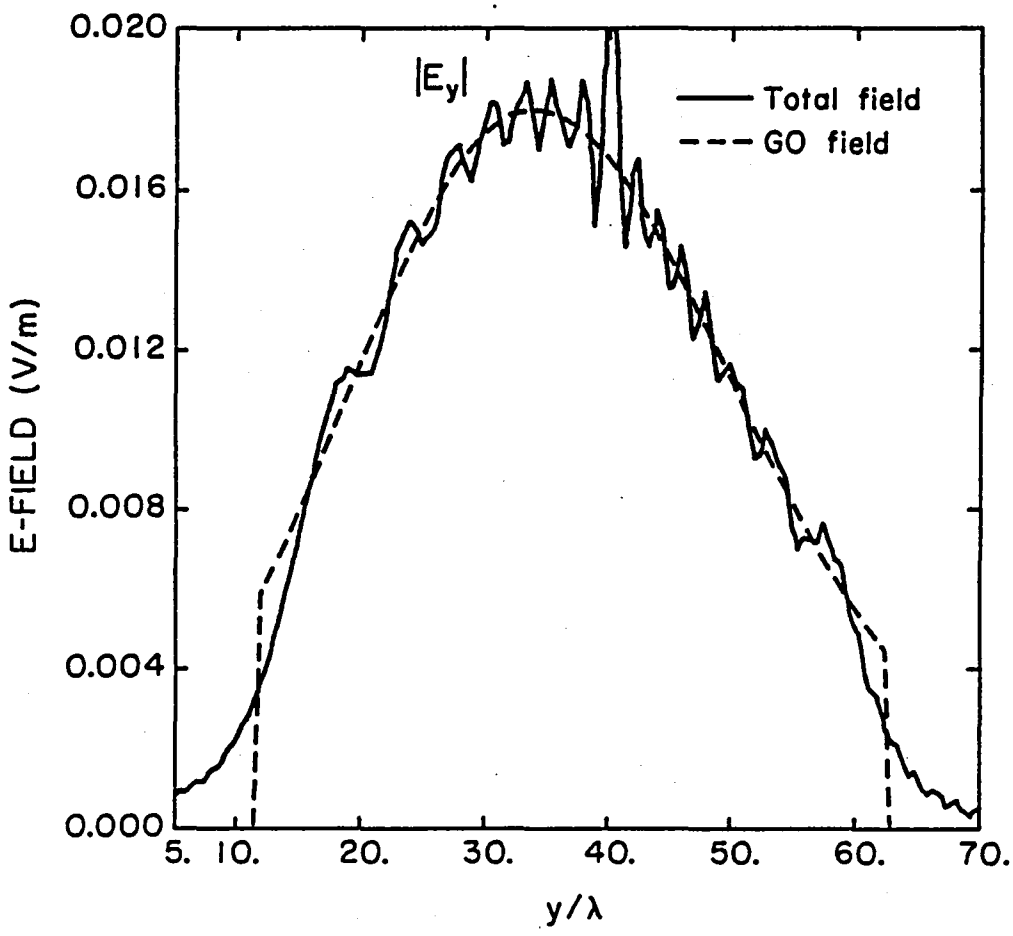

Figure 19a. $|E_y|$ for a y-cut, $d_f = 2\lambda$, $L = 0$.

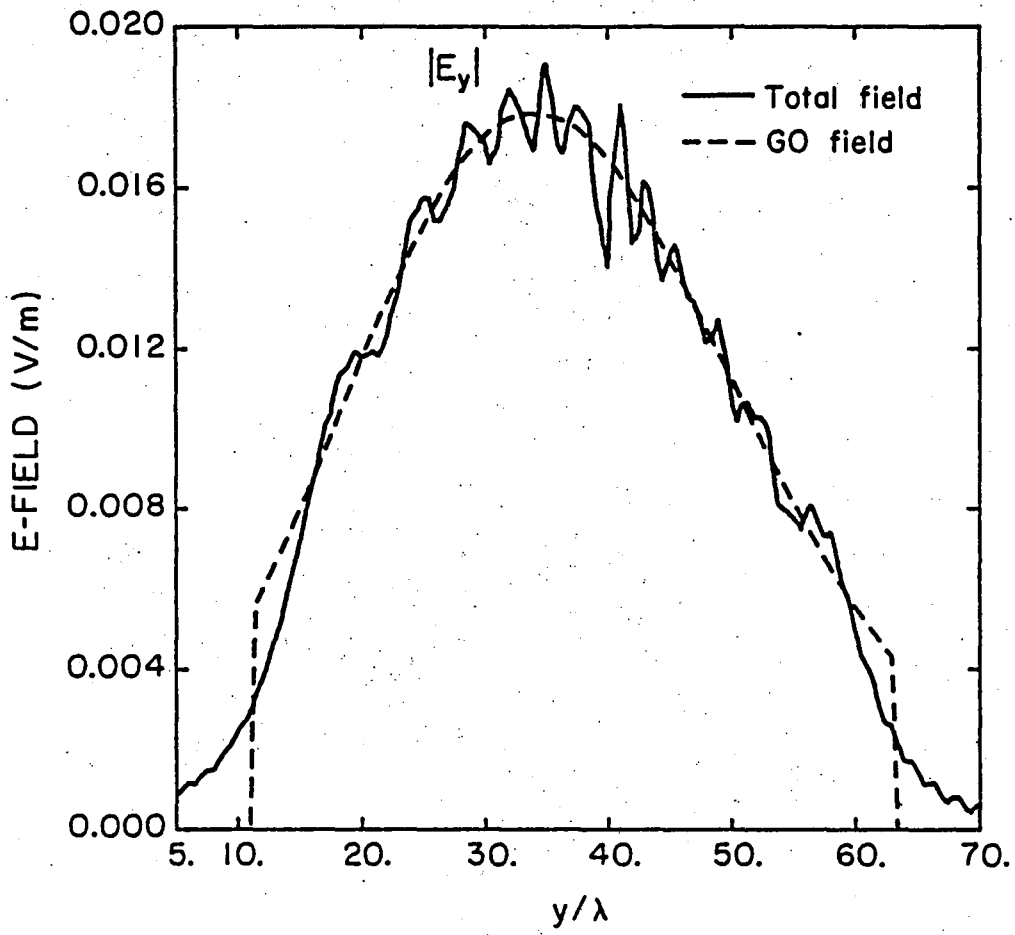

Figure 19b. $|E_y|$ for a y-cut, $d_f = 2\lambda$, $L = 10\lambda$.

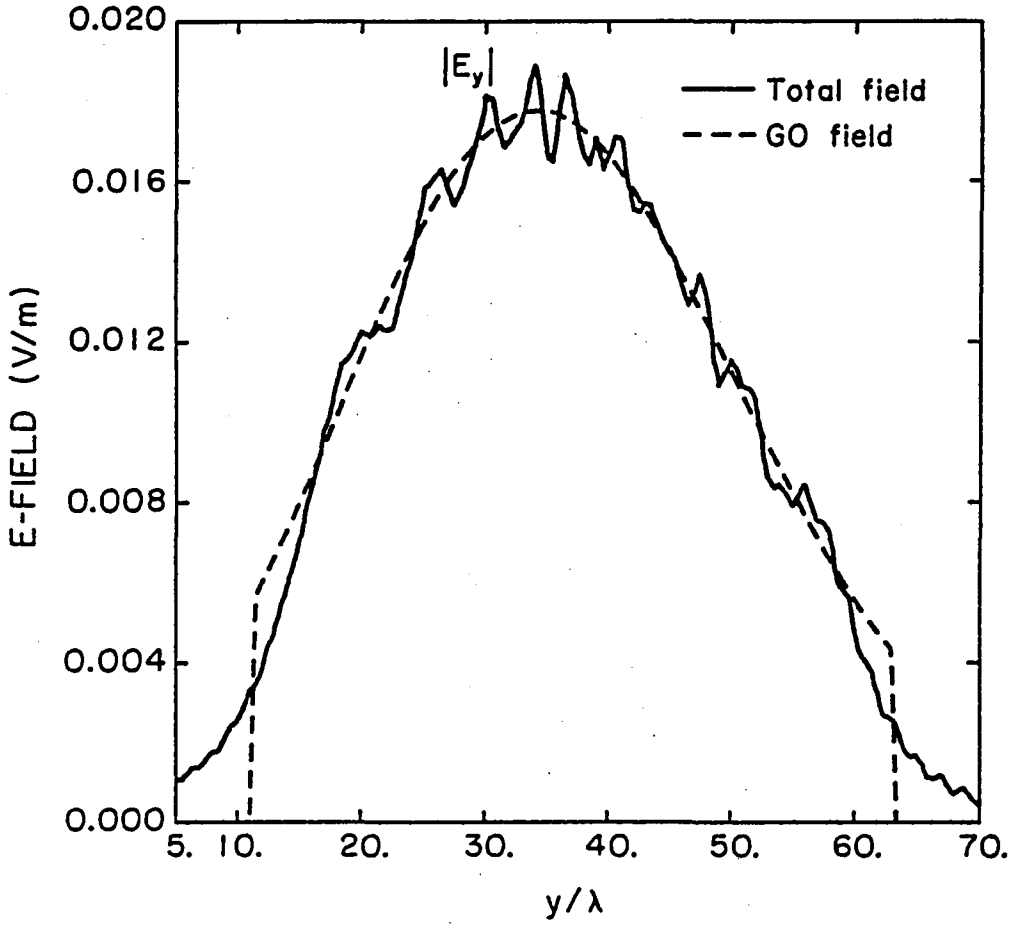

Figure 19c. $|E_y|$ for a y-cut, $d_f = 2\lambda$, $L = 20\lambda$.

$$a = 1/\sqrt{2}\ ,\ b = 1/\sqrt{2},\ \psi = 90^\circ \text{ (RHCP)} \tag{7.5a}$$

$$U_E(\theta) = (\cos\ \theta)^{3.6} \tag{7.5b}$$

$$U_H(\theta) = (\cos\ \theta)^{2.8} \tag{7.5c}$$

Using this aperture integration technique, the secondary pattern for $\phi = 0°$ was computed using GO and GTD constructions. As shown in Figure 20, two patterns are superimposed with Rahmat-Samii's results. One pattern used GO fields only and in computing the other pattern, the edge-diffracted field was included in the aperture field calculation. The gain and sidelobe levels of these two patterns are tabulated versus Rahmat-Samii's results in Table 3 below.

TABLE 3

COMPARISON WITH RAHMAT-SAMII'S RESULTS

	Rahmat-Samii	GO + GTD	GO
main beam	48.28	48.33	48.32
1st sidelobe	28.42	28.29	28.42
2nd sidelobe	22.29	22.18	22.93
3rd sidelobe	18.05	18.02	18.12
4th sidelobe	14.95	14.96	13.40
5th sidelobe	12.39	11.85	11.14
6th sidelobe	10.31	9.05	8.41

Due to the limited amount of computer working space, a 48 x 48 FFT was used. Despite the coarse sampling, the results in Table 3 are in good agreement.

The scan performance of this reflector has been studied by Hung [28]. The Fourier-Bessel series technique is used to compute the secondary pattern. Using the same feed, eq. (7.5), the feed was displaced 5.8 in the

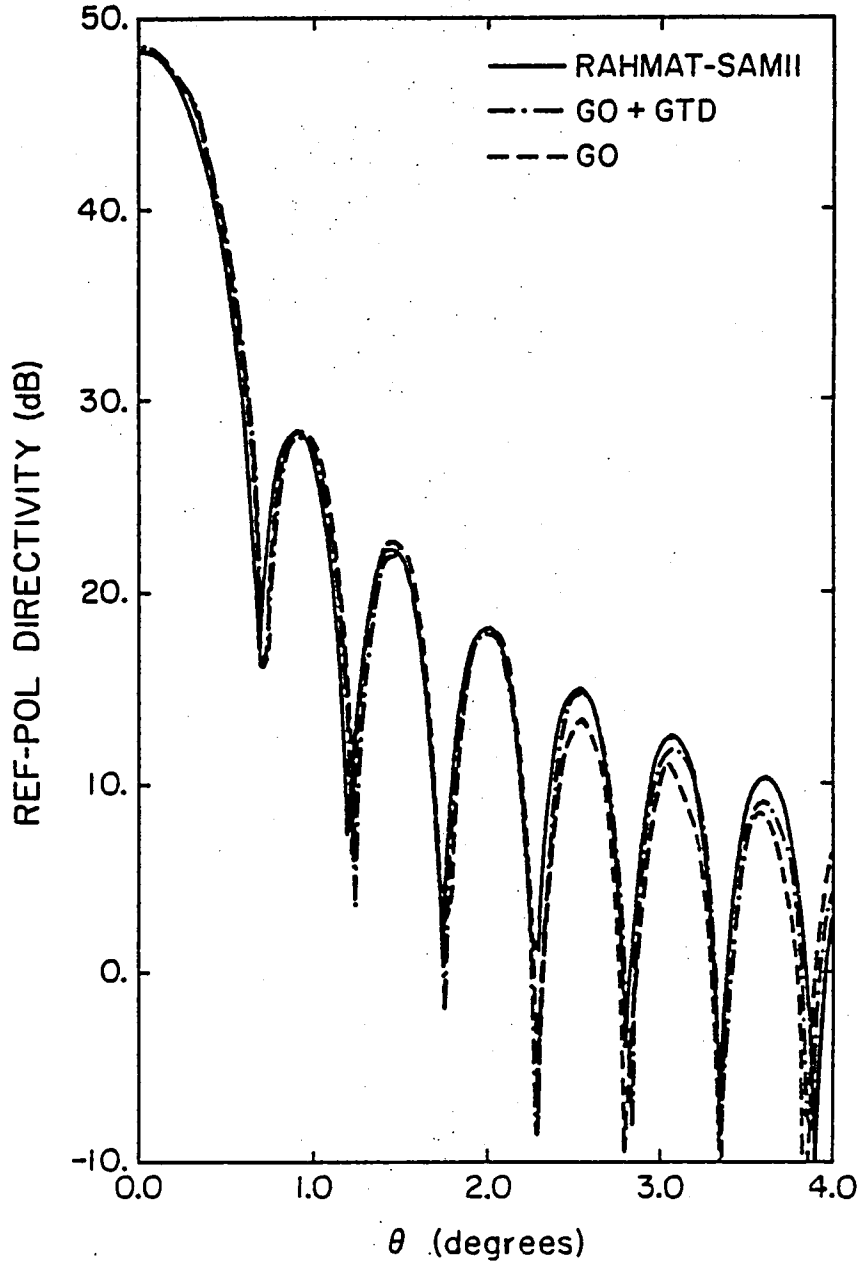

Figure 20. Secondary pattern of a DBS antenna using Jacobi-Bessel series, GO, and GTD.

$-\hat{x}_f$ direction to produce a pattern with peak directivity at $\theta = 3°$ (see Figure 21). The H-plane scan pattern was also computed using the aperture integration technique with and without the edge-diffracted field. Figure 22 depicts the H-plane scan pattern using the aperture integration and Fourier-Bessel series techniques. The patterns are in good agreement.

7.3. TRW Antenna

A dual reflector antenna system was designed by TRW for NASA-Lewis Research Center. The dual reflector is an offset Cassegrain reflector. The main reflector is parabolic and it is described by

$$D = \text{dish diameter} = 257.89\lambda \tag{7.6a}$$

$$f = \text{focal length} = 318.74\lambda \tag{7.6b}$$

$$H = \text{offset length} = 135.51\lambda \tag{7.6c}$$

The reflector is being illuminated by a $\hat{y}_f$-polarized feed at focus with 18 dB edge taper.

Two cuts of Σ_a at the focal plane were taken,

x-cut: $y = H + 0.5D$, $z = f$

y-cut: $x = 0$, $z = f$.

The magnitude and phase of the y-component of the electric field, E_y, are plotted in Figures 23(a)-(b) for the x-cut and in Figures 24(a)-(b) for the y-cut.

The secondary pattern for $\phi = 0°$ of this main reflector is shown in Figure 25. The key features of the reference-pol directivity plot are

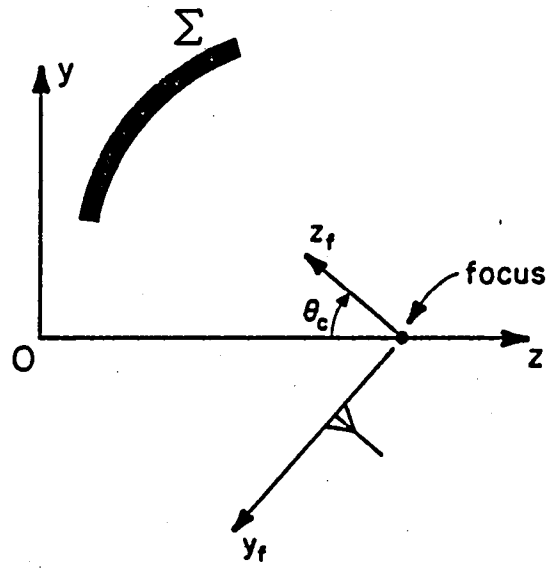

(a) E-plane scan

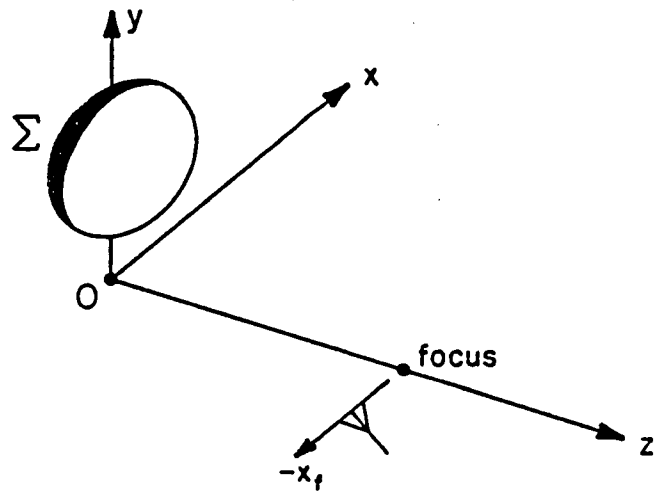

(b) H-plane scan

Figure 21. Feed position for scanning.

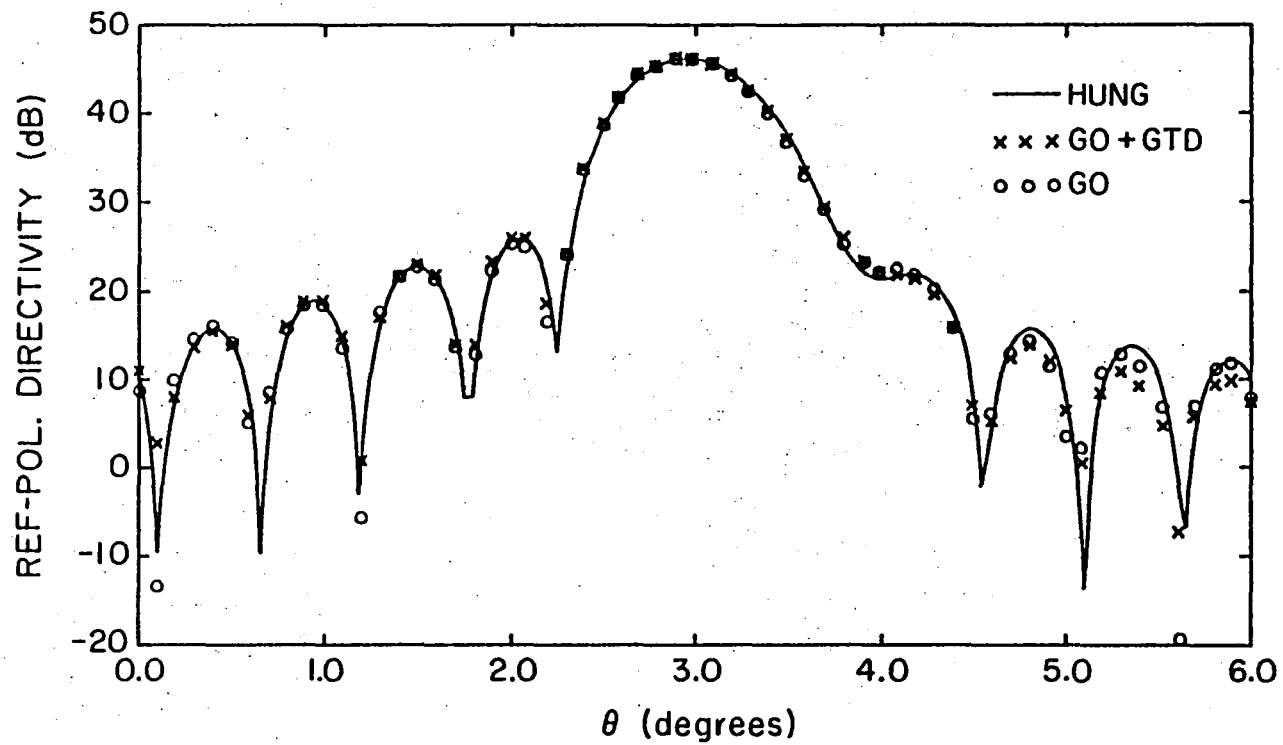

Figure 22. H-plane scan pattern of a DBS antenna using Fourier-Bessel series, GO, and GTD.

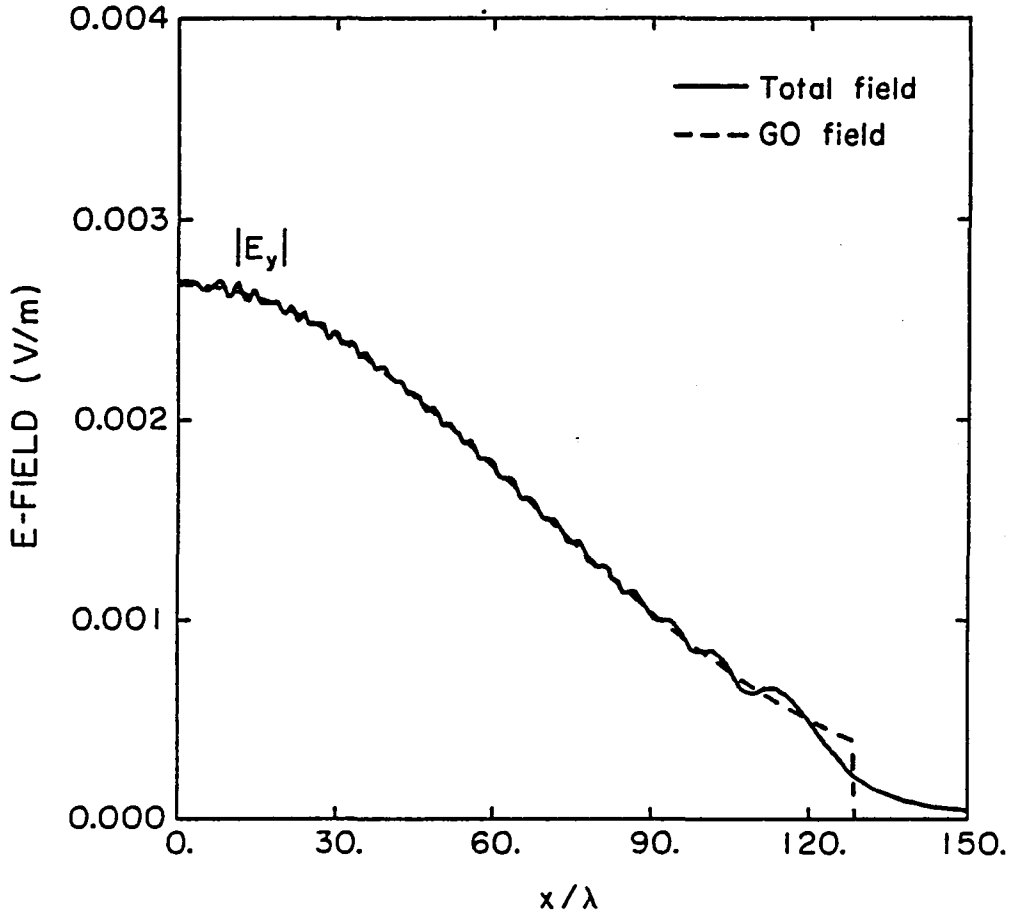

Figure 23a. Amplitude of E_y for a x-cut of TRW main reflector.

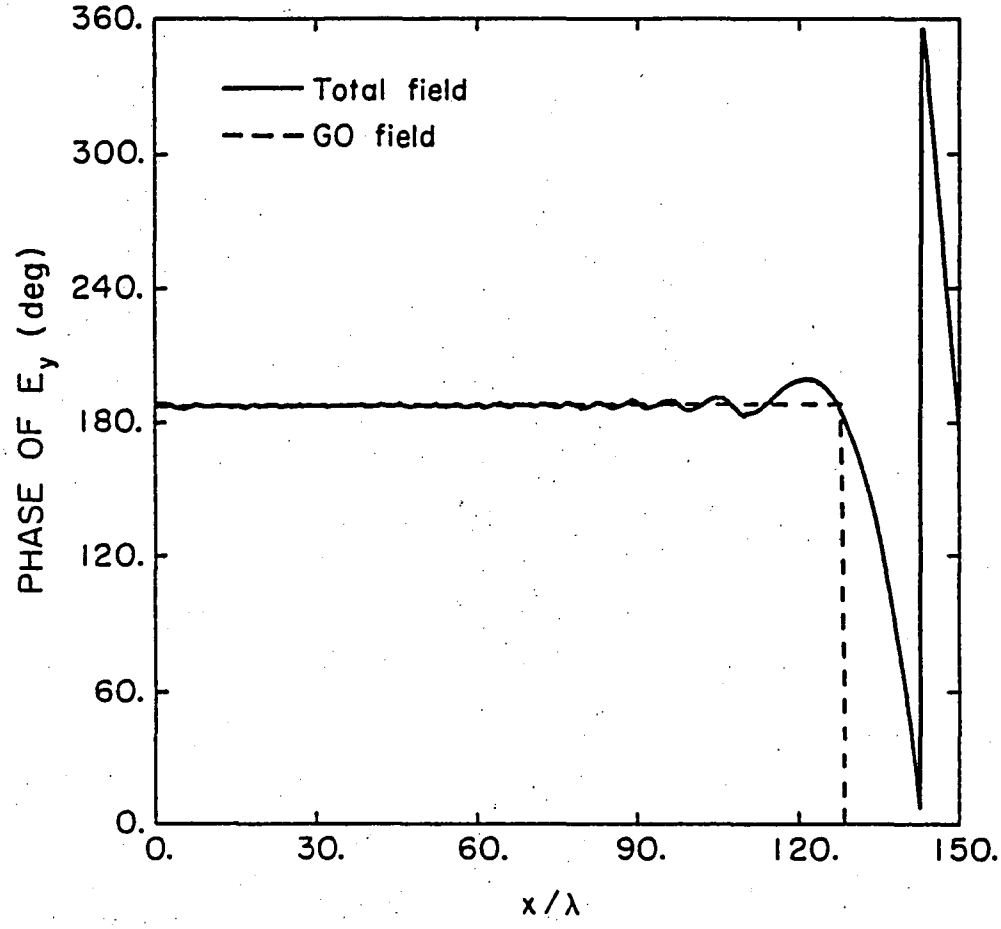

Figure 23b. Phase of E_y for a x-cut of TRW main reflector.

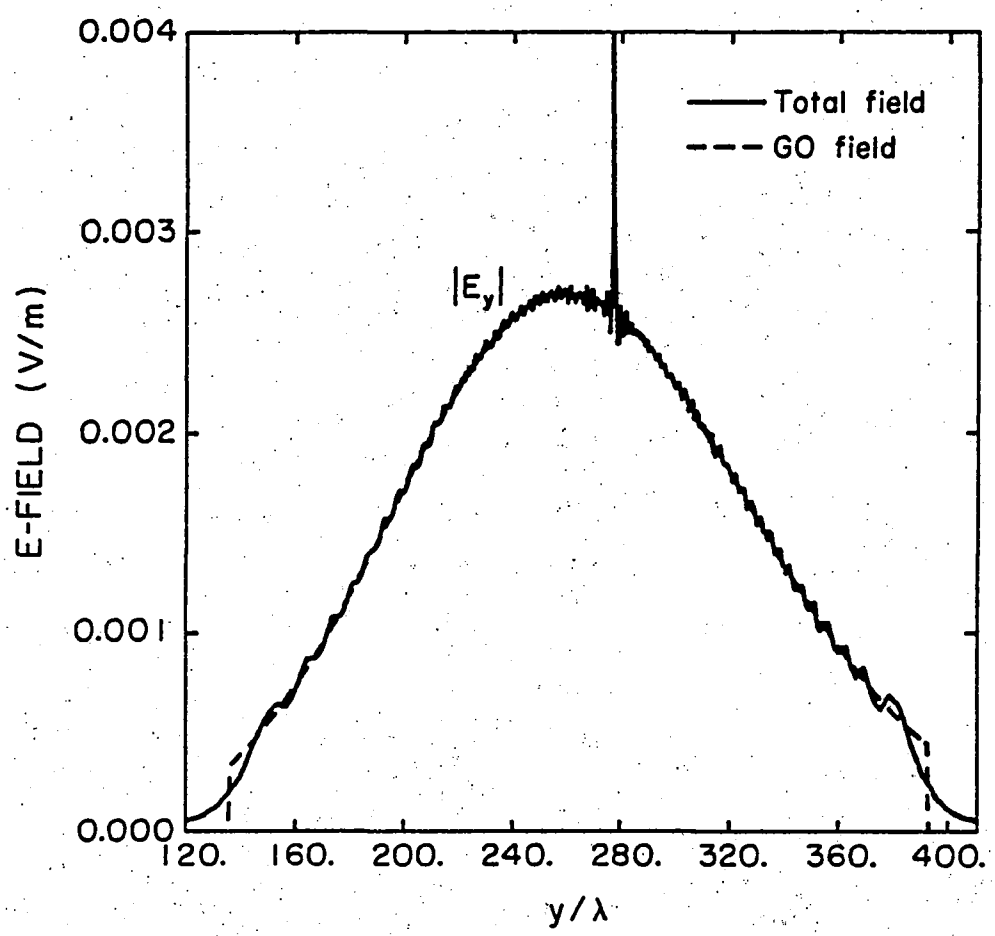

Figure 24a. Amplitude of E_y for a y-cut of TRW main reflector.

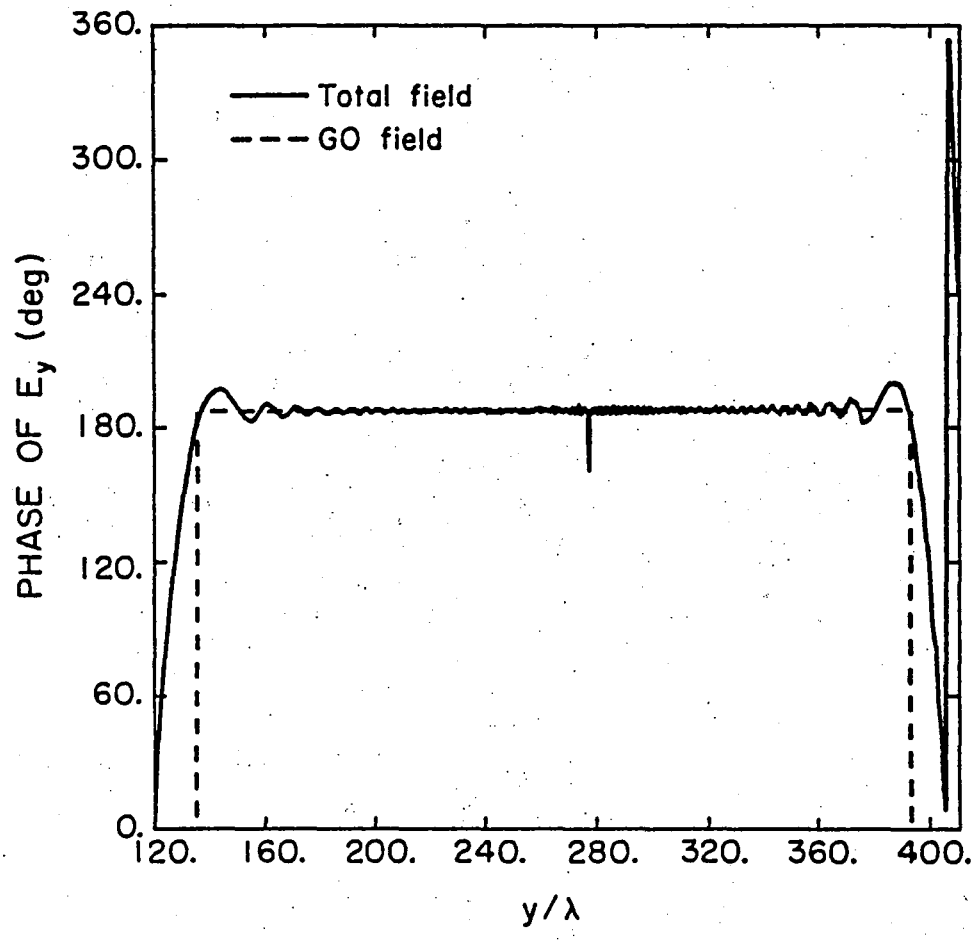

Figure 24b. Phase of E_y for a y-cut of TRW main reflector.

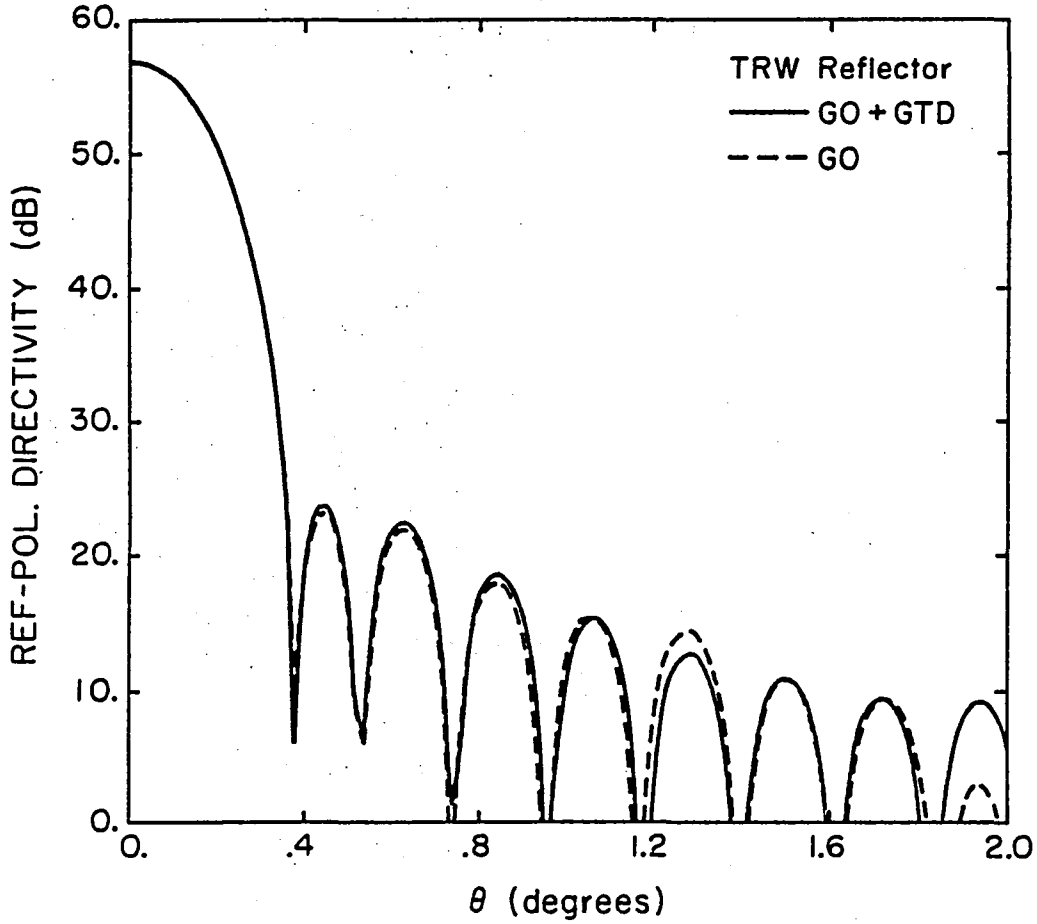

Figure 25. Reference-pol. directivity plot of TRW main reflector, $\phi = 0°$.

	GO + GTD	GO
Gain (dB)	56.95	56.95
HPBW (deg)	0.276	0.277
SLL (dB)	-32.00	-32.26

Figure 26 is a plot of the cross-pol directivity.

The hyperboloid subreflector has a magnification factor of 2. In approximating the performance of this dual reflector system, we employ the equivalent paraboloid [29]. The equivalent paraboloid is described by

$$D = 257.89 \tag{7.7a}$$

$$f = 2(318.74) = 637.48 \tag{7.7b}$$

$$H = 135.51 \tag{7.7c}$$

The corresponding secondary pattern for = 0° is shown in Figure 27. The gain, HPBW, and sidelobe level (SLL) are

	GO + GTD	GO
Gain (dB)	56.87	56.88
HPBW (deg)	0.279	0.280
SLL (dB)	-33.87	-35.15

Figure 28 is a plot of the cross-pol directivity.

Scan performances of the TRW main and equivalent reflector were studied. The scan plane chosen is the $x_f y_f$ plane and E- and H-plane scans were performed (see Figure 21).

For E-plane scan, the coordinates of the feed are

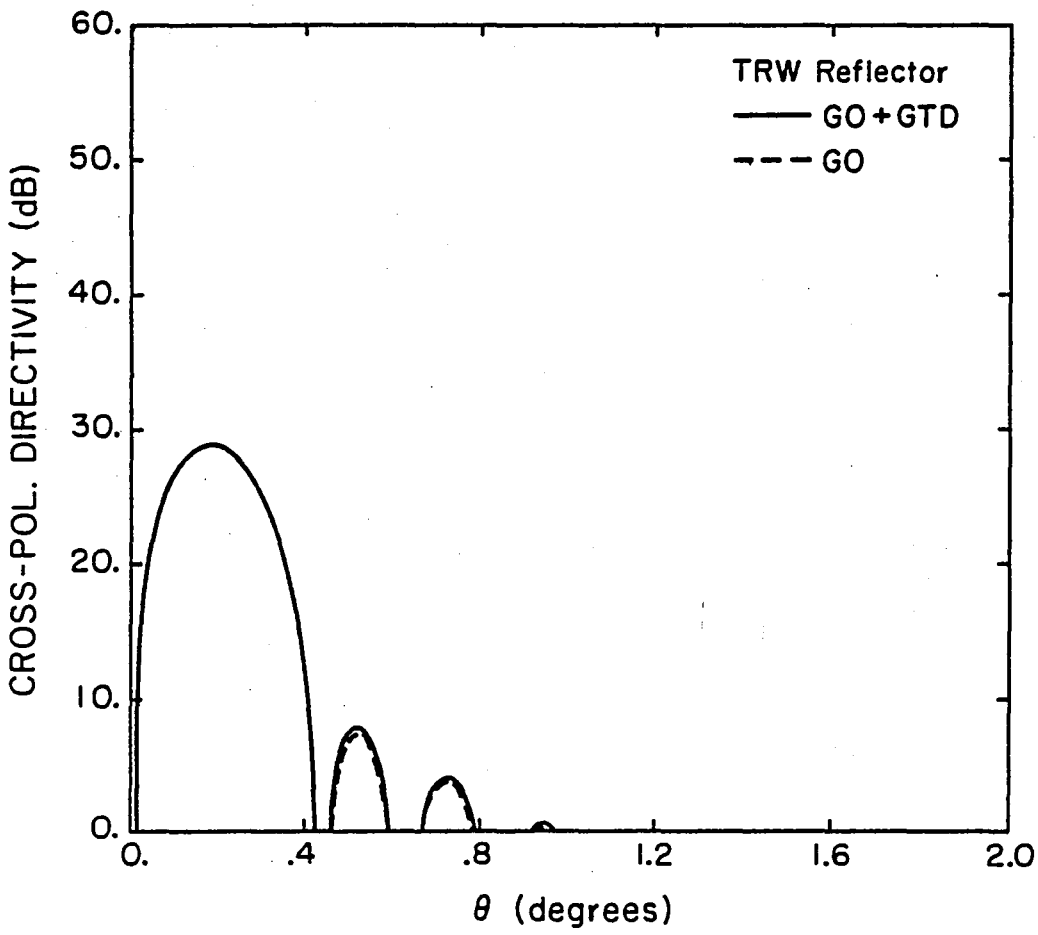

Figure 26. Cross-pol. directivity plot of TRW main reflector, $\phi = 0°$.

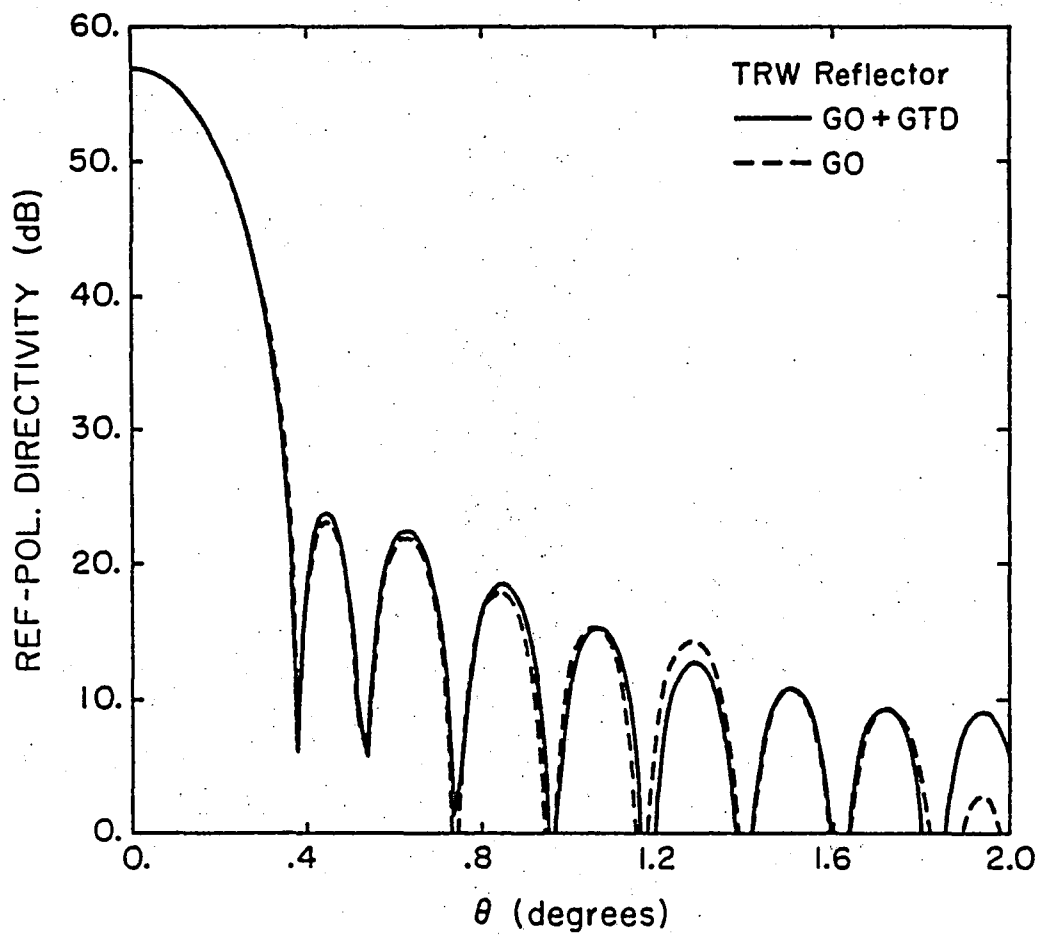

Figure 27. Reference-pol. directivity plot of TRW equivalent reflector, $\phi = 0°$.

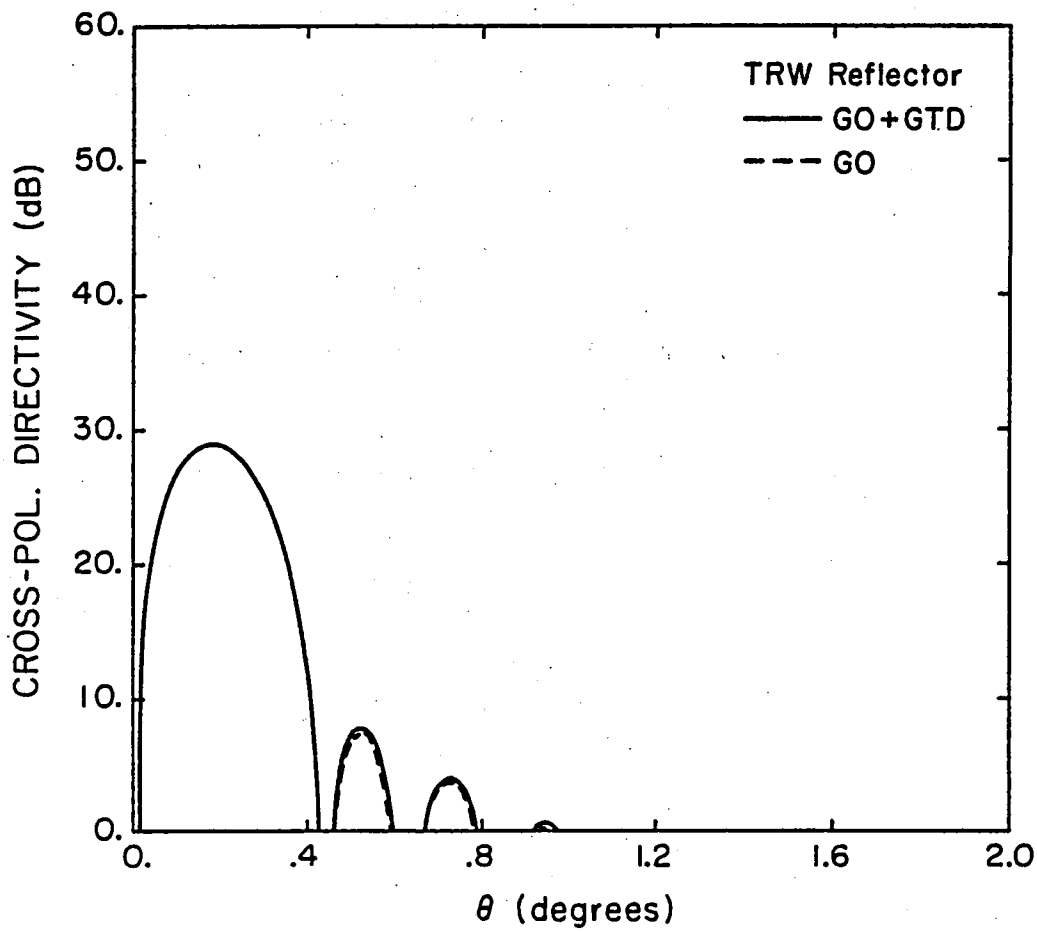

Figure 28. Cross-pol. directivity plot of TRW equivalent reflector, $\phi = 0°$.

$$x = 0 \tag{7.8a}$$

$$y = -f \tan (N \cdot HPBW) \cos \theta_c \tag{7.8b}$$

$$z = f - f \tan (N \cdot HPBW) \sin \theta_c \tag{7.8c}$$

where

f = focal length

$$\theta_c = 2 \tan^{-1} \left(\frac{H + 0.5D}{2f}\right) \tag{7.9}$$

N = number of beamwidth's scan

HPBW = beamwidth of secondary pattern ($\phi = 90°$) with feed at focus.

For H-plane scan, the feed coordinates are given by

$$x = -f \tan (N \cdot HPBW) \tag{7.10a}$$

$$y = 0 \tag{7.10b}$$

$$z = f \tag{7.10c}$$

where

f = focal length

N = number of beamwidth's scan

HPBW = beamwidth of secondary pattern ($\phi = 0°$) with feed at focus.

As the feed moves away from the focus, the secondary pattern degrades. The degradation may be characterized by peak gain loss and half-power beamwidth. These 2 figures-of-merit are plotted versus number of beamwidths scanned for the following four cases:

(1) TRW main reflector, E-plane scan (see Figures 29-30)

(2) TRW equivalent reflector, E-plane scan (see Figures 31-32)

(3) TRW main reflector, H-plane scan (see Figures 33-34)

(4) TRW equivalent reflector, H-plane scan (see Figures 35-36).

As expected, the scan performance of the equivalent reflector is much better than for the main reflector due to its larger f/D value. For the same number of beamwidths scanned, the peak gain loss and amount of beam

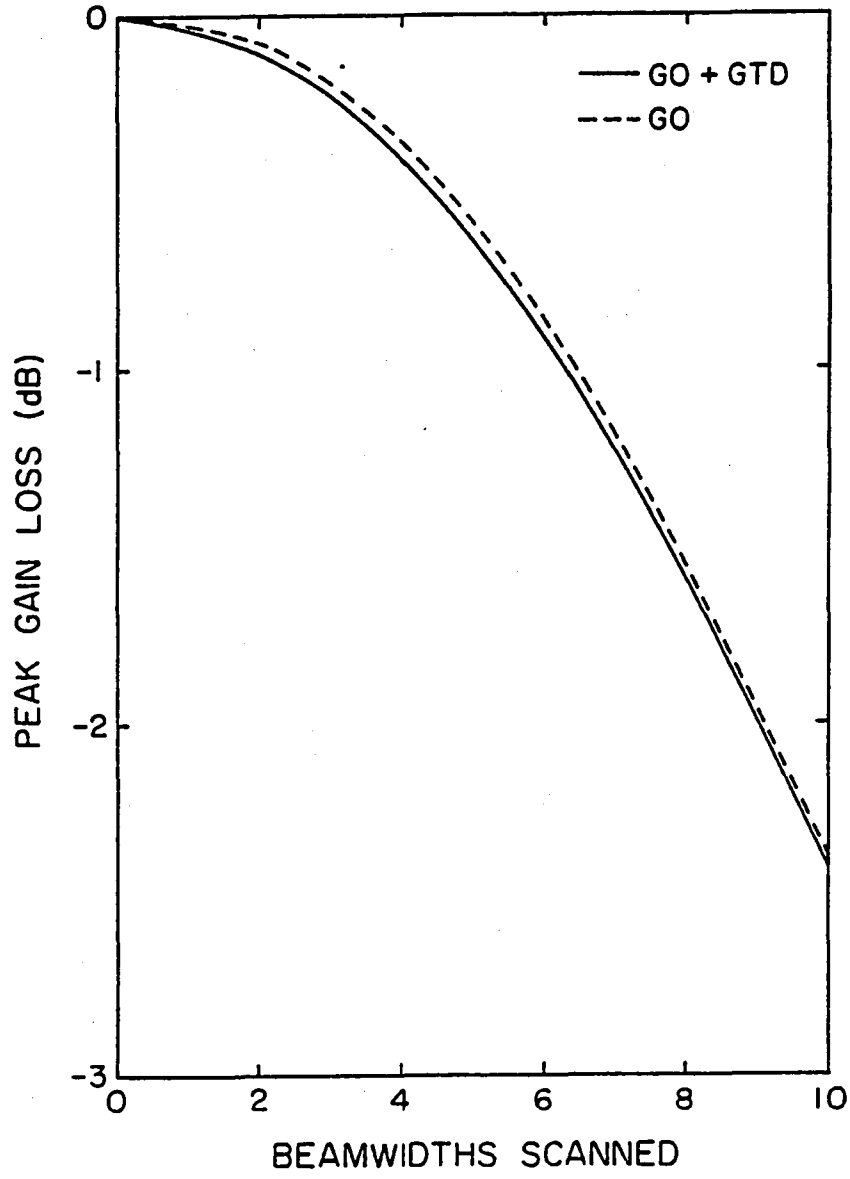

Figure 29. Peak gain loss versus beamwidths scanned for E-plane scan of TRW main reflector.

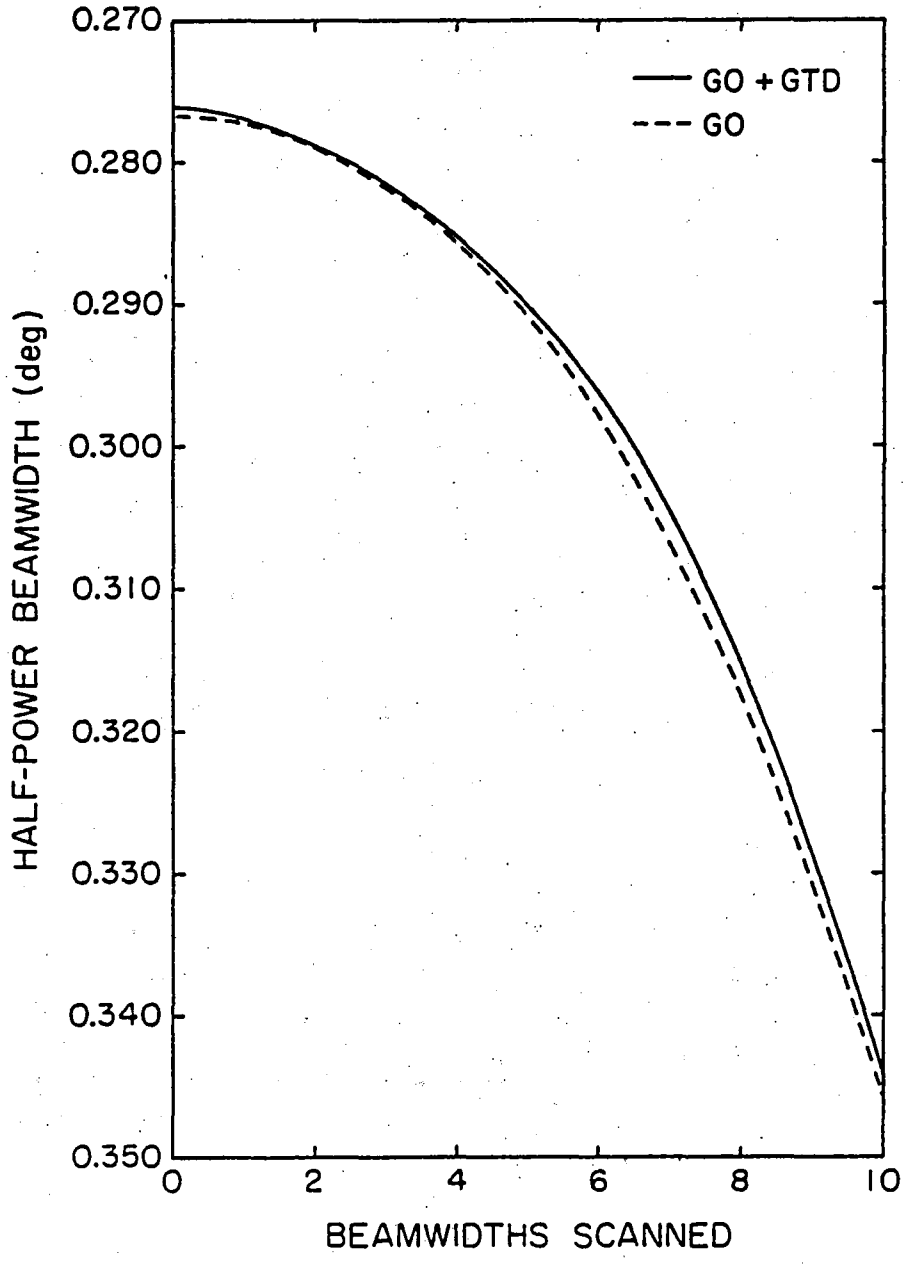

Figure 30. Half-power beamwidth versus beamwidths scanned for E-plane scan of TRW main reflector.

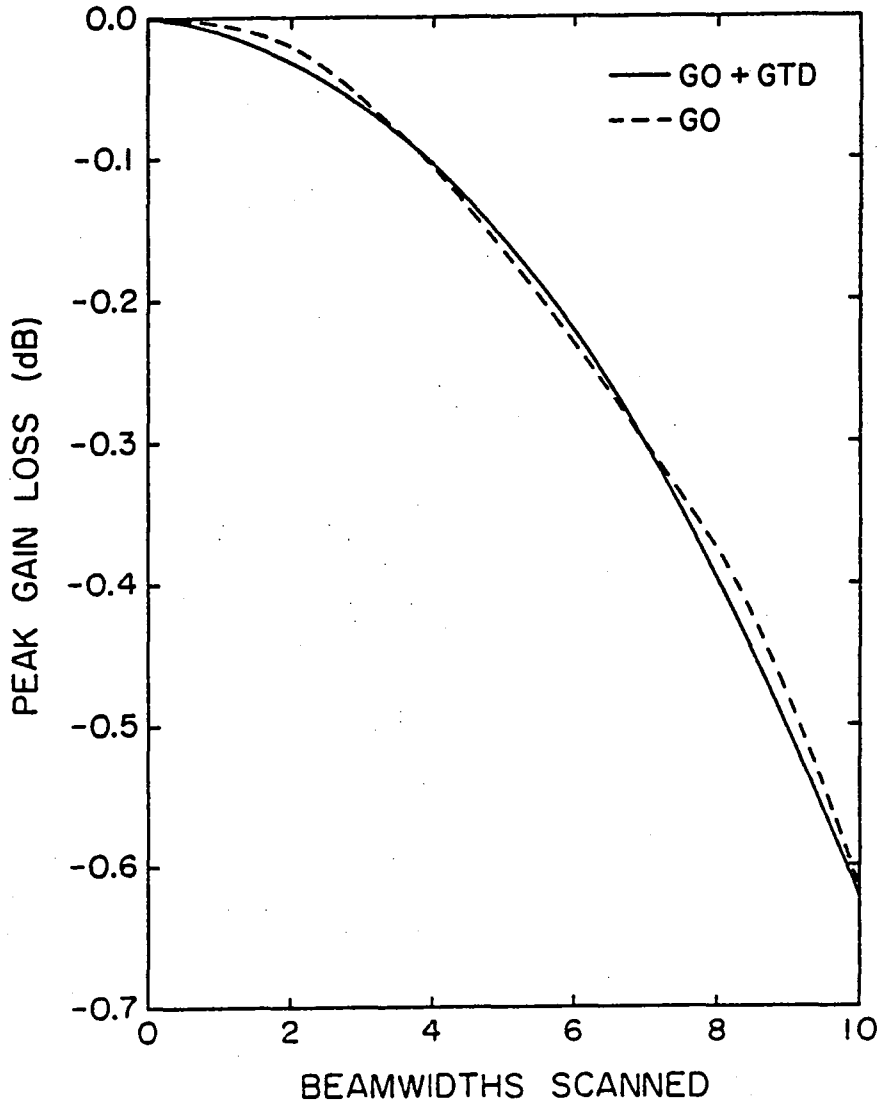

Figure 31. Peak gain loss versus beamwidths scanned for E-plane scan of TRW equivalent reflector.

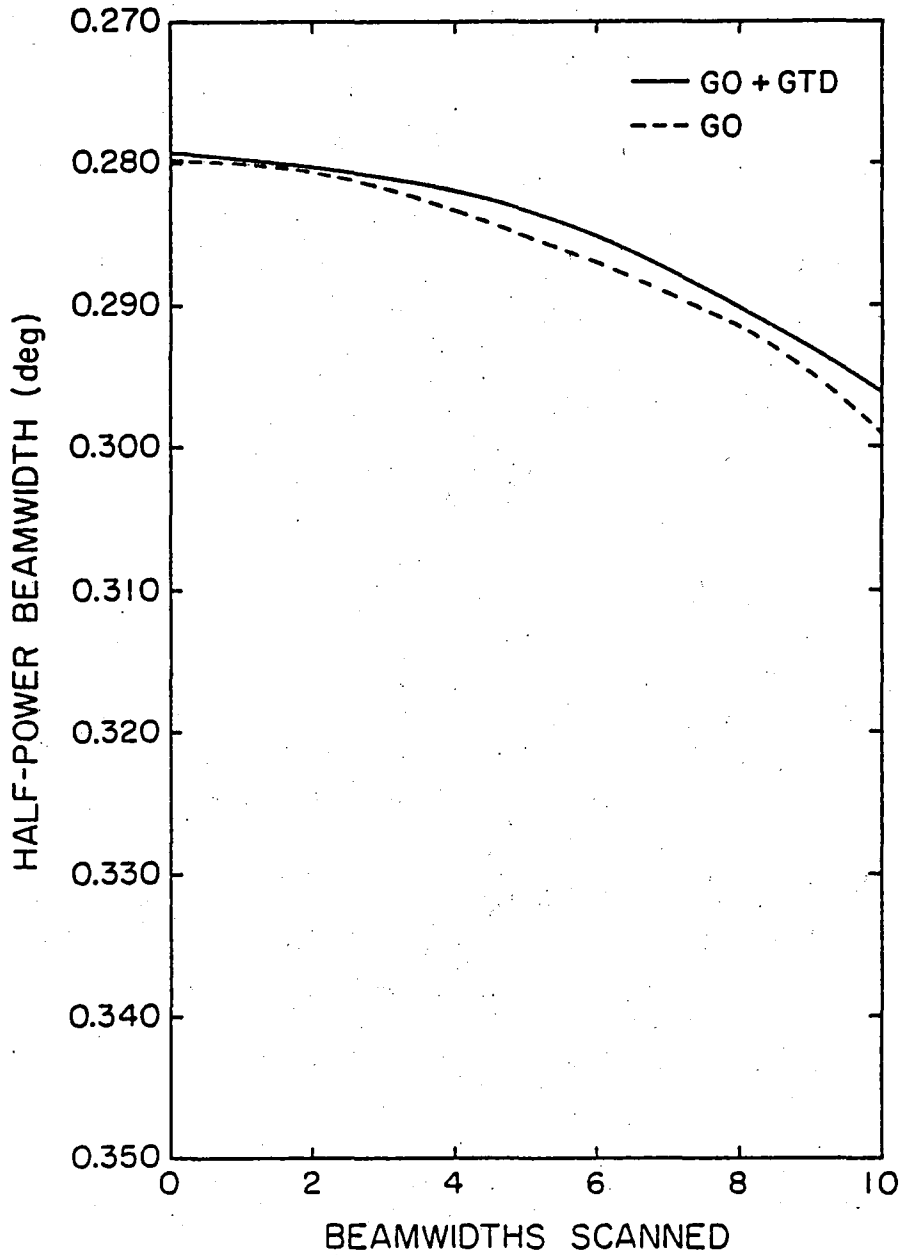

Figure 32. Half-power beamwidth versus beamwidths scanned for E-plane scan of TRW equivalent reflector.

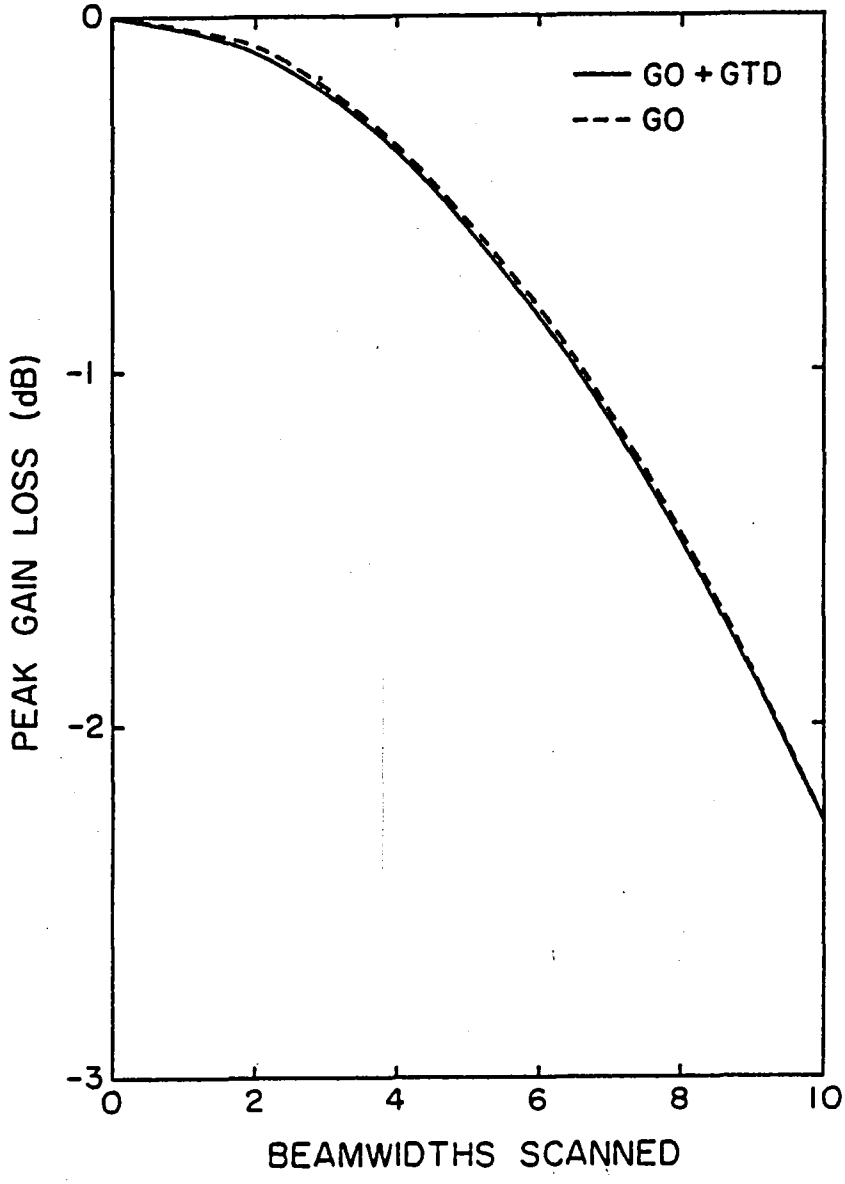

Figure 33. Peak gain loss versus beamwidths scanned for H-plane scan of TRW main reflector.

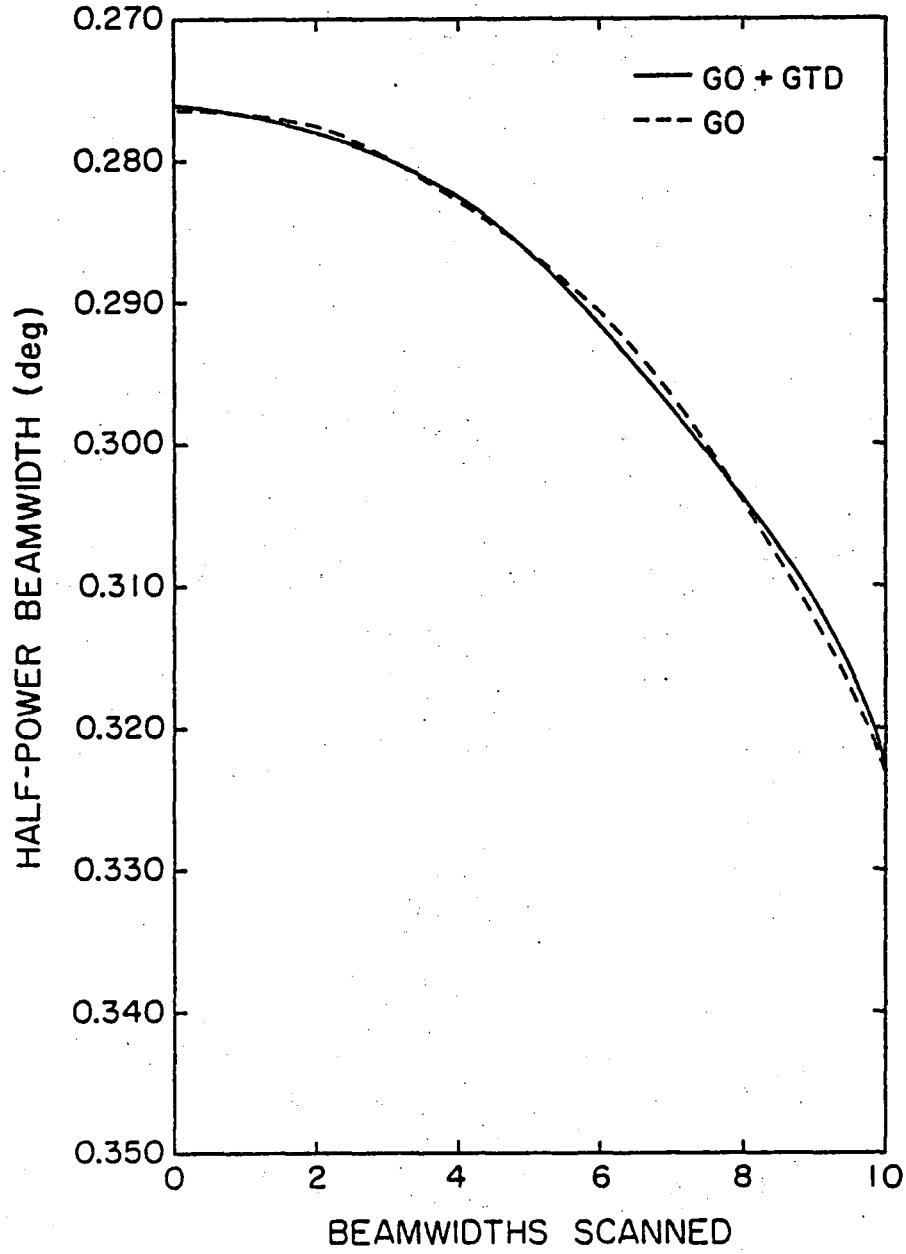

Figure 34. Half-power beamwidth versus beamwidths scanned for H-plane scan of TRW main reflector.

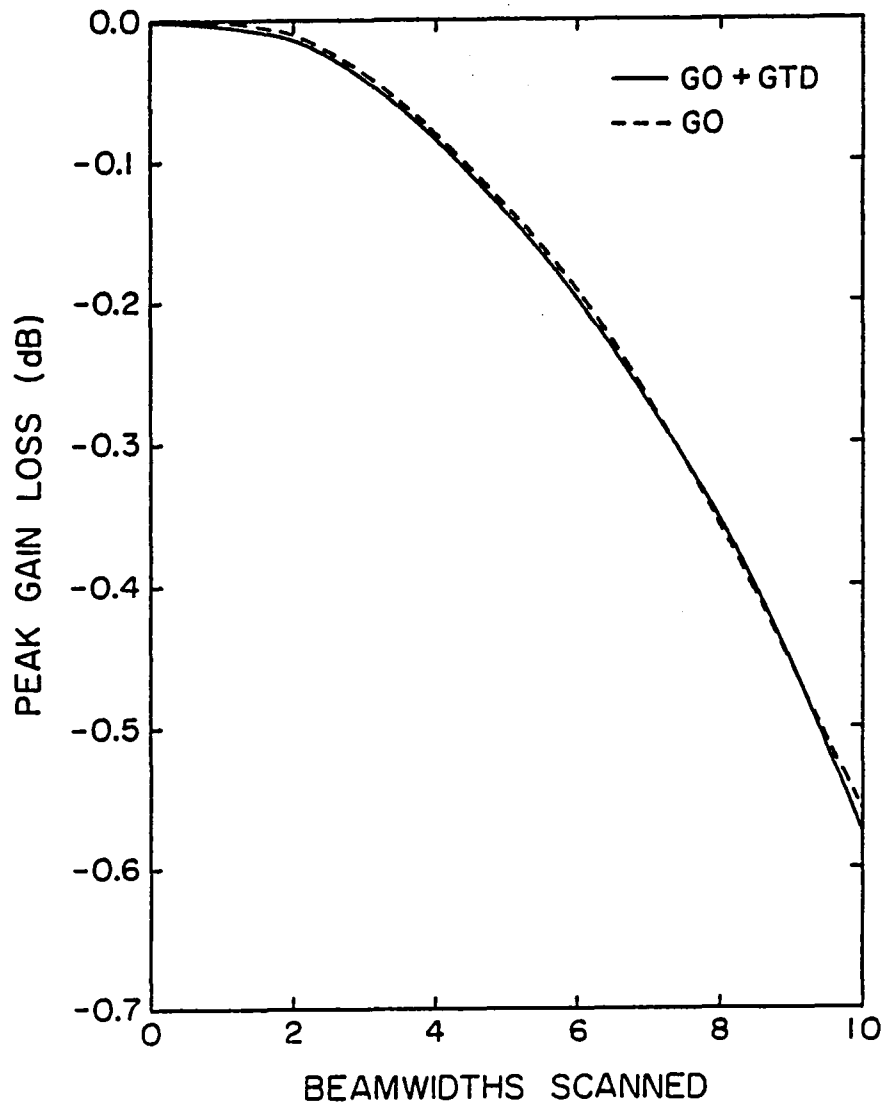

Figure 35. Peak gain loss versus beamwidths scanned for H-plane scan of TRW equivalent reflector.

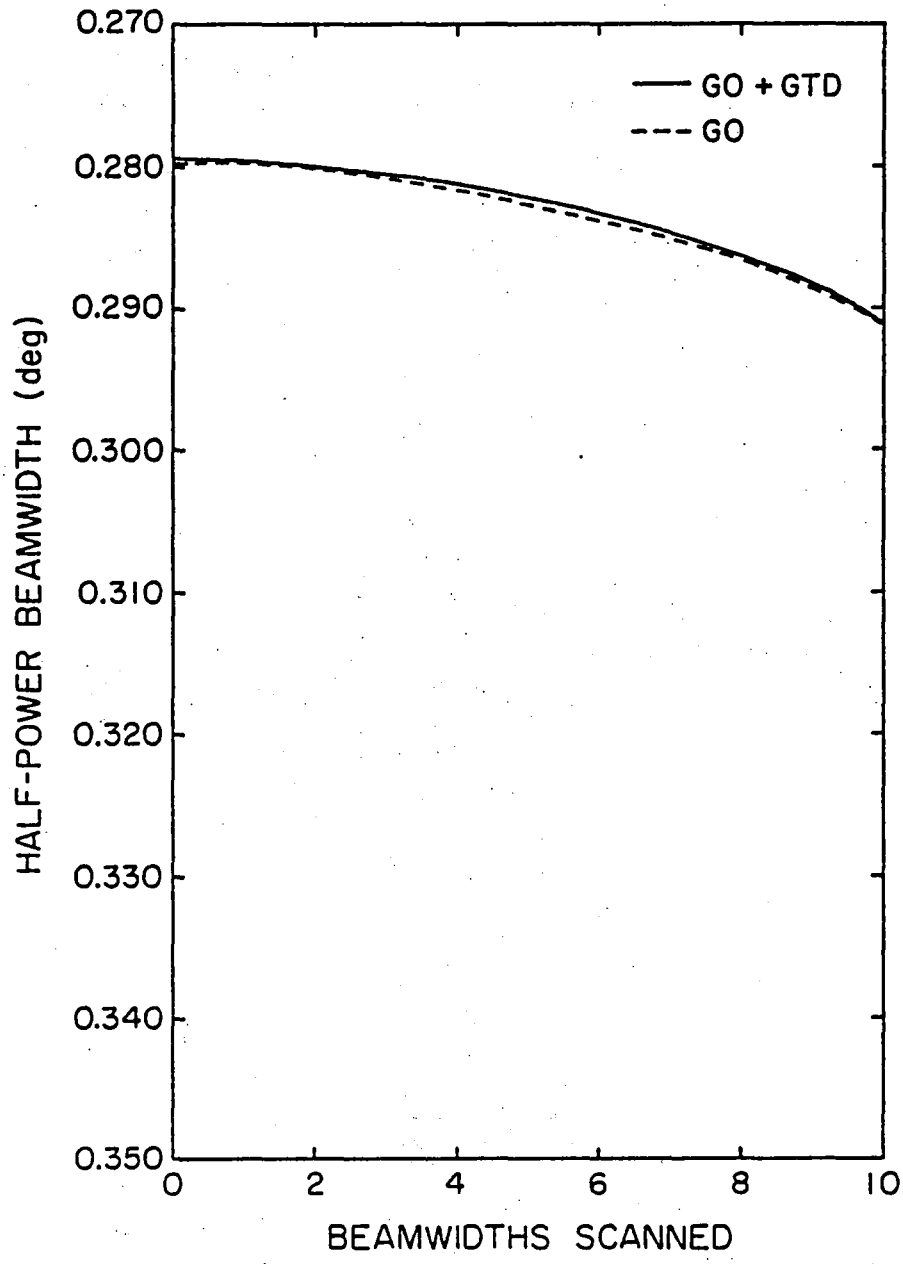

Figure 36. Half-power beamwidth versus beamwidths scanned for H-plane scan of TRW equivalent reflector.

broadening were much less for the equivalent reflector for both E- and H-plane scans. Also, the cross-pol directivity was much lower for the equivalent reflector. Figures 37(a)-(b) and 38(a)-(b) are the reference-pol and cross-pol directivity plots for 6 beamwidth scan in the H-plane for the TRW main and equivalent reflectors, respectively. With respect to the peak directivity, the maximum cross-pol directivity value is -39.15 dB for the equivalent reflector and only -27.95 dB for the main reflector.

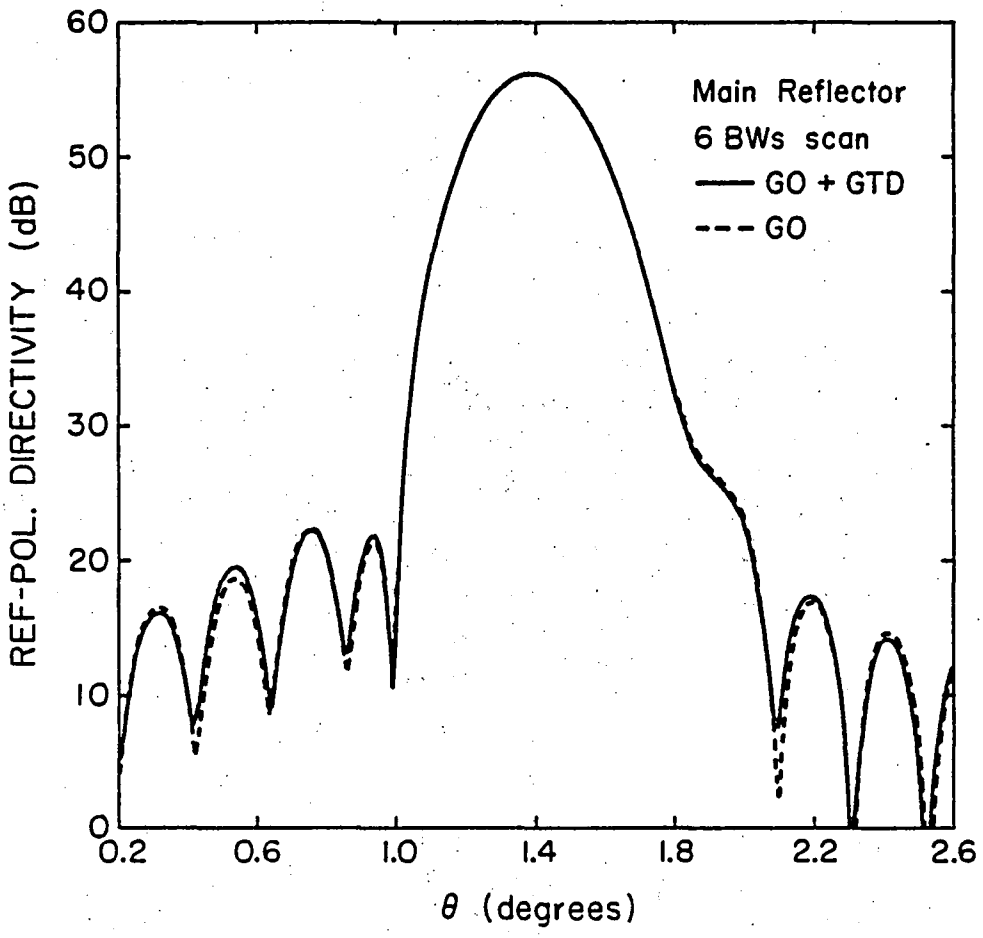

Figure 37a. Reference-pol. directivity plot of TRW main reflector for 6 beamwidth scan in the H-plane.

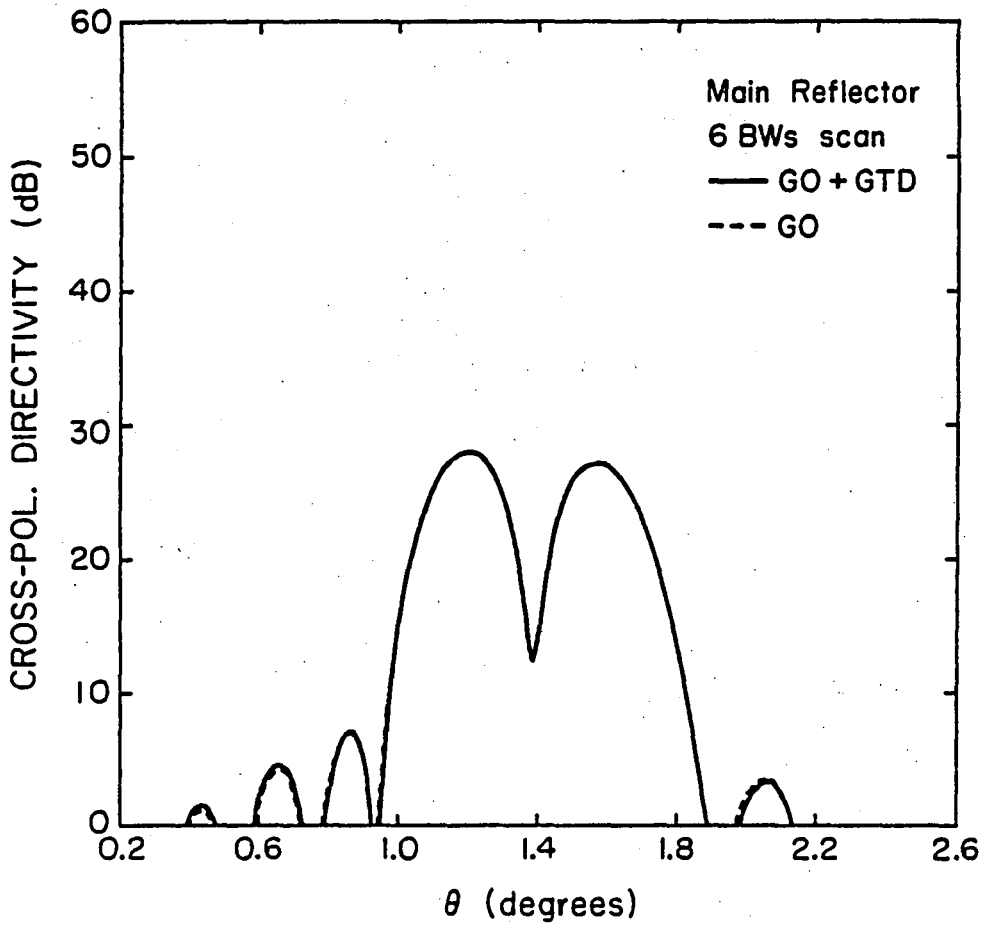

Figure 37b. Cross-pol. directivity plot of TRW main reflector for 6 beam-width scan in the H-plane.

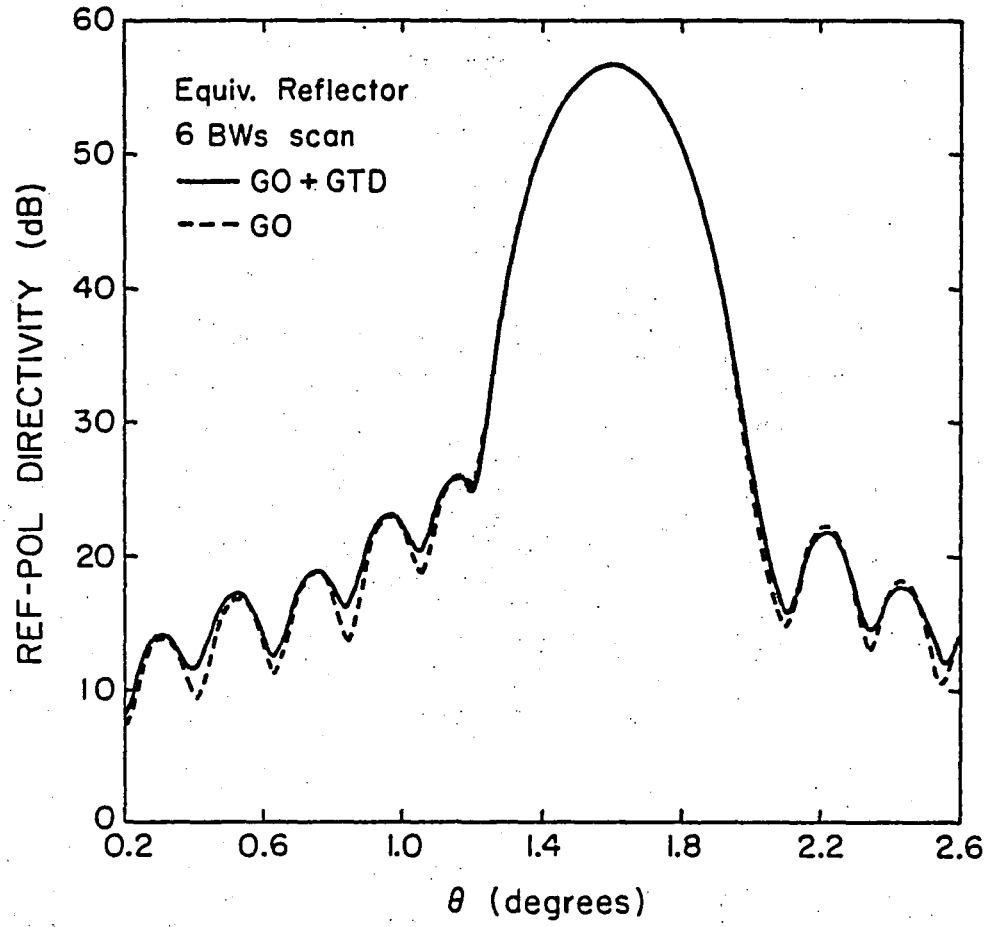

Figure 38a. Reference-pol. directivity plot of TRW equivalent reflector for 6 beamwidth scan in the H-plane.

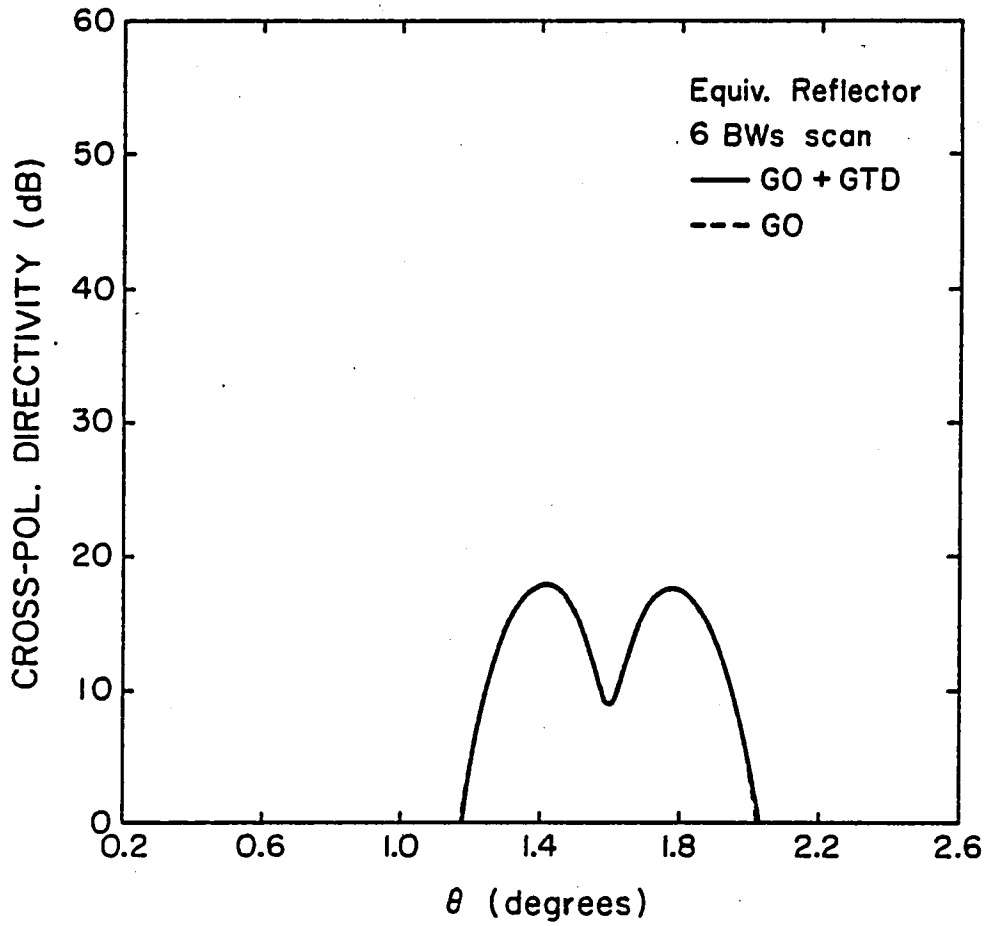

Figure 38b. Cross-pol. directivity plot of TRW equivalent reflector for 6 beamwidth scan in the H-plane.

8. CONCLUDING REMARKS

We have developed a method of calculating the secondary pattern of an arbitrarily shaped reflector illuminated by a feed with arbitrary polarization. An edge-diffracted field was added to the geometrical optics field in the aperture field calculation. By employing the FFT, the secondary pattern is computed very efficiently. The results for the secondary pattern are in good agreement with those obtained by the physical optics integral. Furthermore, this method can be conveniently extended to secondary pattern computation of multiple reflector systems, which will be done in the next phase of this project.

REFERENCES

[1] S. Silver, Microwave Antenna Theory and Design, New York: McGraw-Hill, 1949.

[2] W. V. T. Rusch and P. Potter, Analysis of Reflector Antennas, New York: Academic, 1970.

[3] C. C. Hung and R. Mittra, "Secondary pattern and focal region distribution of reflector antennas under wide-angle scanning," IEEE Transactions on Antennas and Propagation, vol. AP-31, pp. 756-763, 1983.

[4] Y. Rahmat-Samii and V. Galindo-Israel, "Shaped reflector antenna analysis using the Jacobi-Bessel series," IEEE Transactions on Antennas and Propagation, vol. AP-28, pp. 425-435, 1980.

[5] C. C. Hung, "Fourier-Bessel series representation for the far field pattern of arbitrary reflector antennas," Lockheed Missiles and Space Company, Sunnyvale, CA, LMSC Rep. 844955, 1982.

[6] V. Galindo-Israel and R. Mittra, "A new series representation for the radiation integral with application to reflector antennas," IEEE Transactions on Antennas and Propagation, vol. AP-25, pp. 631-641, 1977.

[7] R. Mittra, Y. Rahmat-Samii, V. Galindo-Israel, and R. Norman, "An efficient technique for the computation of vector secondary patterns of offset paraboloid reflectors," IEEE Transactions on Antennas and Propagation, vol. AP-27, pp. 294-304, 1979.

[8] P. A. J. Ratnasiri, R. G. Kouyoumjian, and P. H. Pathak, "The wide angle side lobes of reflector antennas," ElectroScience Laboratory, The Ohio State University, Columbus, Ohio, Report 2183-1, 1970.

[9] W. V. T. Rusch, "Geometrical scattering from inflected surfaces of revolution," Tech. Rept. Jet Propulsion Lab., Pasadena, CA, August 1975.

[10] W. V. T. Rusch and O. Sorensen, "The geometrical theory of diffraction for axially symmetric reflectors," IEEE Transactions on Antennas and Propagation, vol. AP-23, pp. 414-419, 1975.

[11] J. F. Kauffman, W. F. Croswell, and L. J. Jowers, "Analysis of the radiation patterns of reflector antennas," IEEE Transactions on Antennas and Propagation, vol. AP-24, pp. 53-65, January 1976.

[12] R. Acosta, private communication.

[13] Y. Hwang, C. H. Tsao, and C. C. Han, AP Digest, p. 88, May 1983, Houston, TX.

[14] S. W. Lee and G. A. Deschamps, "A uniform asymptotic theory of electromagnetic diffraction by a curved wedge," IEEE Transactions on Antennas and Propagation, vol. AP-24, pp. 25-34, 1976.

[15] R. G. Kouyoumjian and P. H. Pathak, "A uniform geometrical theory of diffraction for an edge in a perfectly conducting surface," Proc. IEEE, vol. 62, pp. 1448-1461, 1974.

[16] Y. Rahmat-Samii, "Useful coordinate transformations for antenna applications," IEEE Transactions on Antennas and Propagation, vol. AP-27, pp. 571-574, 1979.

[17] J. B. Keller, "Geometrical theory of diffraction," J. Opt. Soc. Amer., vol. 52, pp. 116-130, 1962.

[18] S. W. Lee, "Uniform asymptotic theory on electromagnetic edge diffraction: A review," EM Lab. Rep. 77-1, University of Illinois at Urbana-Champaign, Jan. 1977.

[19] D. S. Ahluwalia, R. M. Lewis, and J. Boersma, "Uniform asymptotic theory of diffraction by a plane screen," SIAM J. Appl. Math., vol. 16, pp. 783-807, 1968.

[20] S. W. Lee, "Uniform asymptotic theory on electromagnetic edge diffraction: a review," in Electromagnetic Scattering, P. L. E. Uslenghi, Ed., New York: Academic, pp. 67-119, 1978.

[21] R. M. Lewis and J. Boersma, "Uniform asymptotic theory of edge diffraction," J. Math. Phys., vol. 10, pp. 2291-2305, 1969.

[22] H. Goldstein, Classical Mechanics, Reading, MA: Addison-Wesley, pp. 107-109, 1953.

[23] S. W. Lee, "Differential geometry for GTD applications," EM Lab. Rep. 77-21, University of Illinois at Urbana-Champaign, October 1977.

[24] R. C. Menendez and S. W. Lee, "On the role of the geometrical optics field in aperture diffraction," IEEE Transactions on Antennas and Propagation, vol. AP-25, pp. 688-695, 1977.

[25] R. E. Collin and F. J. Zucker, Antenna Theory Part 1, New York: McGraw-Hill, 1969.

[26] A. C. Ludwig, "The definition of cross polarization," IEEE Transactions on Antennas and Propagation, vol. AP-21, pp. 116-119, 1973.

[27] S. W. Lee, Y. Rahmat-Samii, V. Galindo-Israel, W. A. Imbriale, and R. Mittra, "A baseline design of STC-DBS antenna version II," Lee and Mittra Consultants, Champaign, Illinois.

[28] C. C. Hung, unpublished work and private communication.

[29] P. W. Hannan, "Microwave antennas derived from the Cassegrain telescope," IEEE Transactions on Antennas and Propagation, vol. AP-9, pp. 140-153, 1961.

APPENDIX A

INSTRUCTIONS TO RUN COMPUTER PROGRAMS

To run the computer programs on the University of Illinois CYBER 175 system to compute the secondary pattern of an offset parabolic reflector, the user should perform the following

(1) create input file TAPE2
(2) run program BAL1
(3) run programs BPT, BFFT
(4) for plot, use BPLOT3

The computer commands corresponding to steps (1)-(4) are

```
(first create TAPE2)
R
BAL1
R
P.LOAD(BPT,BFFT); EXECUTE
R
BPLOT3
```

The secondary pattern is stored in TAPE13.

The input file TAPE2 consists of 14 lines. These inputs are described below.

1. H, D, f, z_o -- offset parabolic reflector parameters as depicted in Figure 13
2. 1 -- cylinder boundary or 2 -- cone boundary
3. x_c, y_c, K_1, K_2 -- cylinder boundary parameters or P, $\theta_1, \theta_2, \theta_3$ -- cone boundary parameters as shown in Figure 5
4. $\gamma_1, \gamma_2, \gamma_3$ -- Eulerian angles (see Figure 7)

5. x_1, y_1, z_1 -- source point coordinates in main reflector coordinate system.

6. a, b, ψ -- polarization of feed

7. q_E, q_H -- feed taper parameter for E- and H-plane primary patterns

8. L -- location of aperture plane beyond the focal plane as shown in Figure 14a (taken to be zero)

9. type in 1 or 2

10. x_1, x_2, N
11. y_1, y_2, N

x_1, x_2, y_1, y_2 are bounds of Σ_a (see Figure 12a), N is the number of points in sampling.

12. 0 -- use UAT or 1 -- use UTD, 0 -- compute GO and edge-diffracted field or 1 -- compute GO field only

13. θ_1, θ_2, NFFP -- For a theta cut, θ_1 is the first value and θ_2 is the last value of theta. NFFP is the number of θ values for the secondary pattern

14. 1 -- use E-fields only for the aperture field calculation or 2 -- use H-fields only, PHI -- this is the constant ϕ value when computing the secondary pattern.

For an arbitrarily shaped reflector, the user should use the binary version of MAIN instead of BAL1. However, lines 97 to 107 must be replaced with either the coordinates of the points that define the reflector or the new equations that describes the reflector. For an arbitrary reflector, line 1 of input file TAPE2 has no meaning. Thus, delete line 41 of MAIN and the input file is lines 2 through 14 of TAPE2 described above.

APPENDIX B

VIEWGRAPHS FOR A PAPER ENTITLED "CALCULATION OF NEAR-FIELD OF A REFLECTOR BY GTD" BY P. T. LAM, S. W. LEE, AND R. ACOSTA PRESENTED IN INTERNATIONAL IEEE/AP-S SYMPOSIUM NATIONAL RADIO SCIENCE MEETING, JUNE 1984

GTD Analysis of Reflector Antennas

P. T. Lam and S. W. Lee
Electromagnetics Lab
University of Illinois
and
R. Acosta
Nasa-Lewis Research Center

Outline

1. Problem description
2. Motivation
3. Approach
4. Results
5. Conclusion

Problem Description

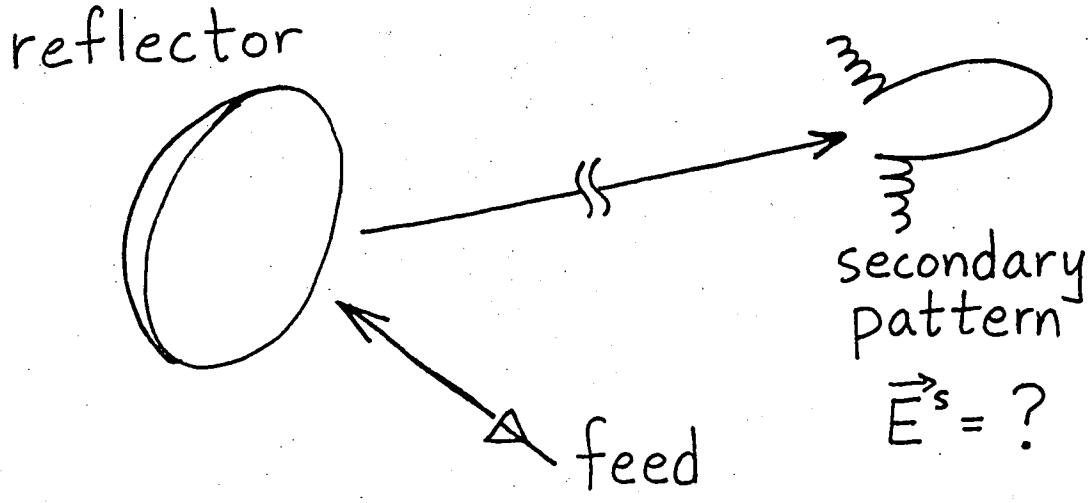

Given:

Description of reflector
Feed location and orientation
Feed pattern and polarization

Determine:

Secondary pattern

Motivation

* general reflector shape

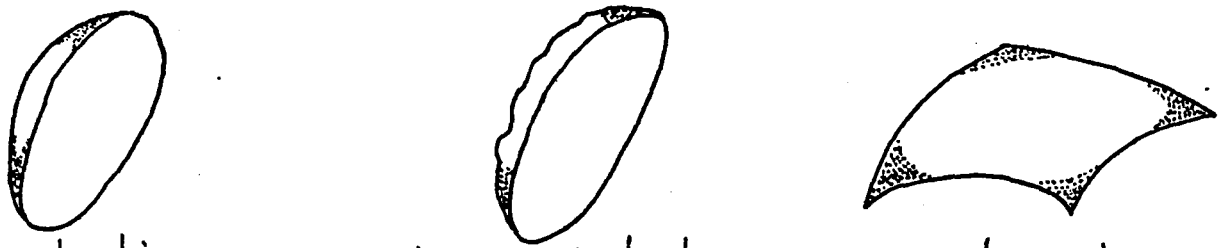

parabolic — thermal distortions — shaped

* multiple reflector systems

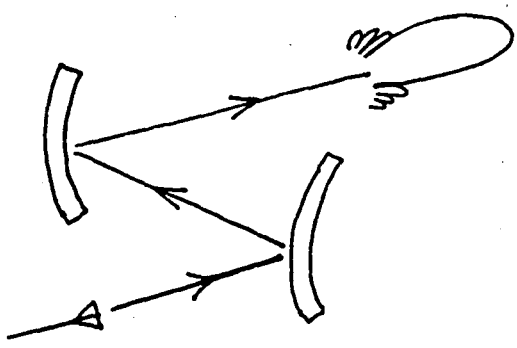

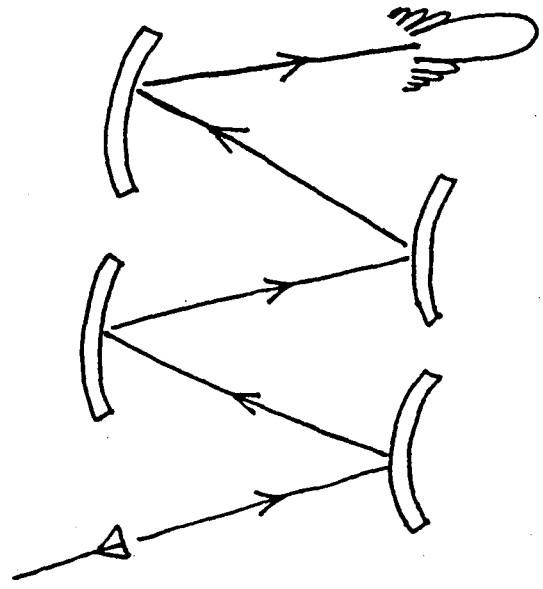

* efficient secondary pattern computation

1 pattern (2 cuts) ~ $10

DBS antenna design requires ~5000 patterns

⇓

$50,000

THREE METHODS OF CALCULATING SECONDARY PATTERN $\vec{E}^s$

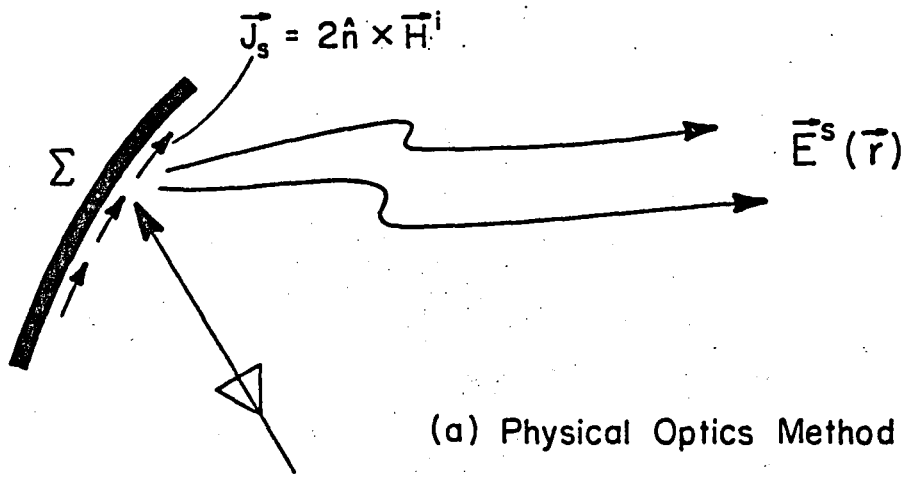

(a) Physical Optics Method

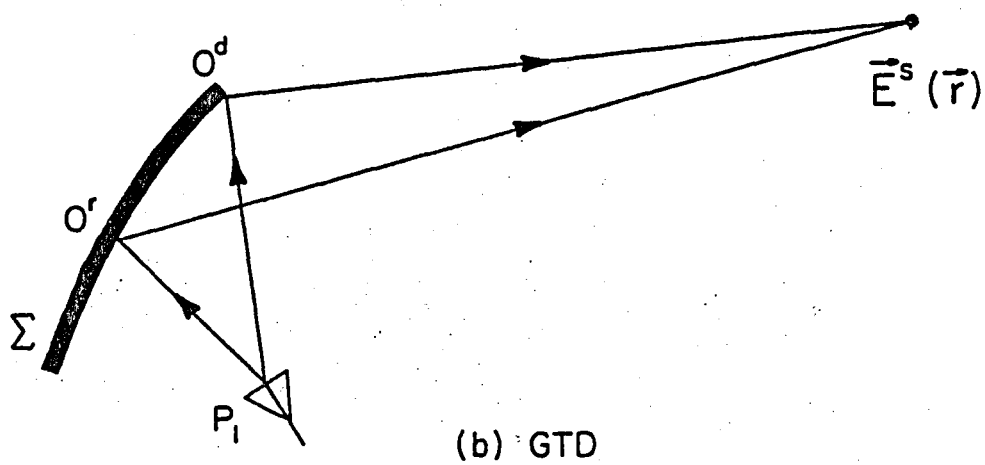

(b) GTD

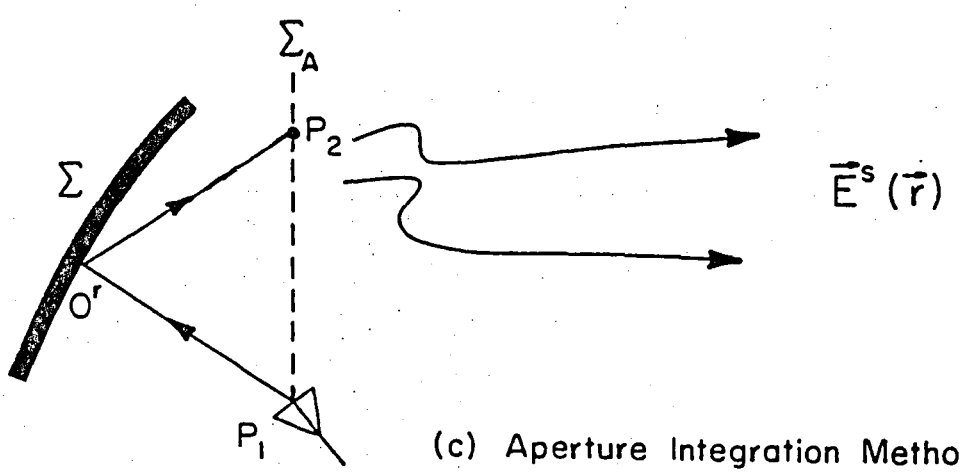

(c) Aperture Integration Method

Comparison of the three methods

As a reference, let us represent the exact solution of $\vec{E}^s$ by the following high-frequency asymptotic series:

$$\vec{E}^s(\vec{r}) \sim e^{-jkS(\vec{r})}\left[\vec{A}_0(\vec{r}) + k^{-\frac{1}{2}}A_1(\vec{r}) + k^{-1}A_2(\vec{r}) + \ldots\right]$$

for $k \to \infty$

Methods	Accuracy	Limitation
PO AI	recover $\vec{A}_0$ and partial $\vec{A}_1$	not accurate for wide-angle lobes
GTD	recover $\vec{A}_0$ and $\vec{A}_1$	predicts infinite field in main beam direction (caustics)

Advantages of aperture integration (AI)

1. May be conveniently extended to multiple reflector systems
2. Provides a theoretical check for near field measurements
3. Accuracy is comparable to physical optics (PO). The use of the FFT makes it numerically efficient.

APPROACH

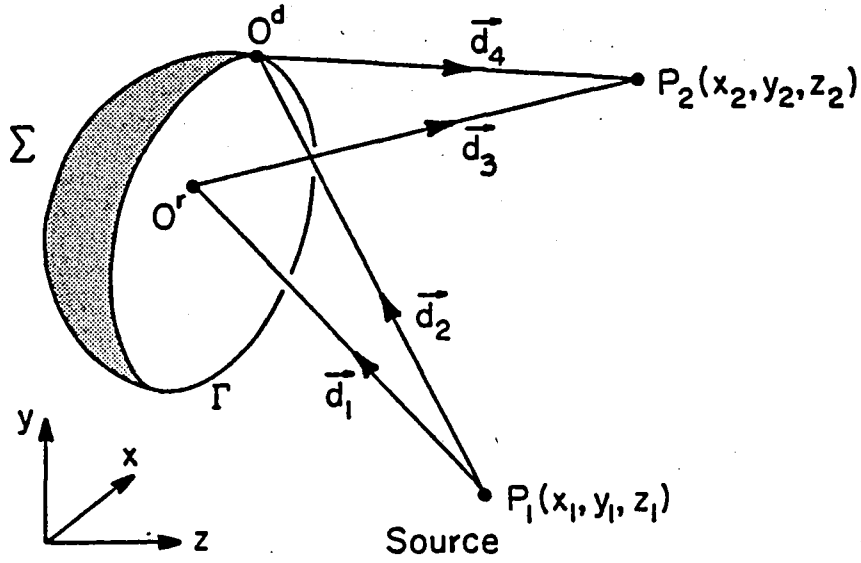
O^d
$\vec{d}_4$
$P_2(x_2, y_2, z_2)$
Σ
$\vec{d}_3$
O^r
$\vec{d}_2$
Γ
$\vec{d}_1$
y
x
z
$P_1(x_1, y_1, z_1)$
Source

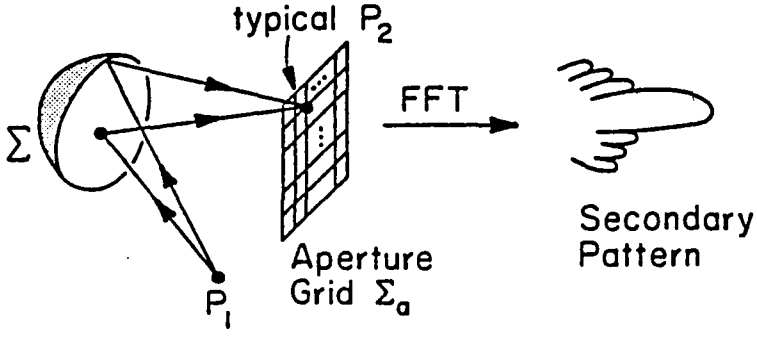
typical P_2
Σ
FFT
Secondary
Pattern
Aperture
Grid Σ_a
P_1

What's new in this AI approach?

1. Edge-diffracted field is included in the aperture field calculation.

2. Surface of reflector is completely arbitrary.

3. Edge of reflector is not restricted to a circular curve. It may be an arbitrary curve lying on an elliptical cone or cylinder.

Description of reflector

Reflector surface:

- Analytic
- Numerical

Reflector boundary:

- Elliptical cylinder
- Elliptical cone

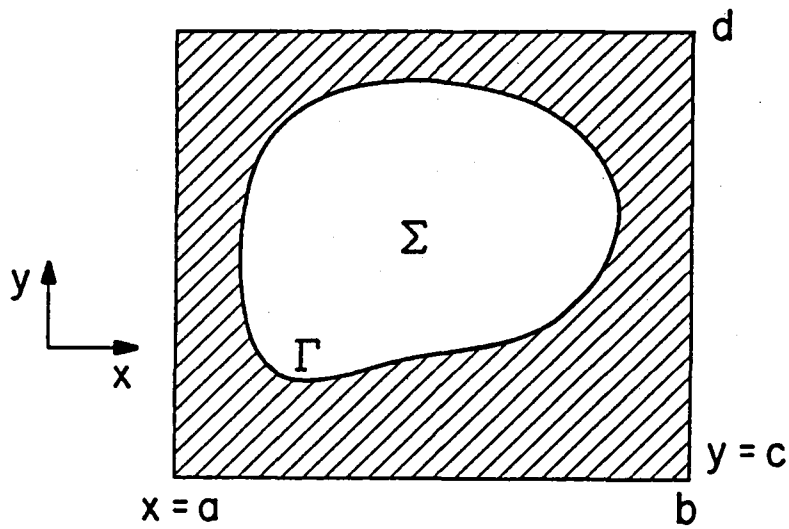

Two types of reflector boundary

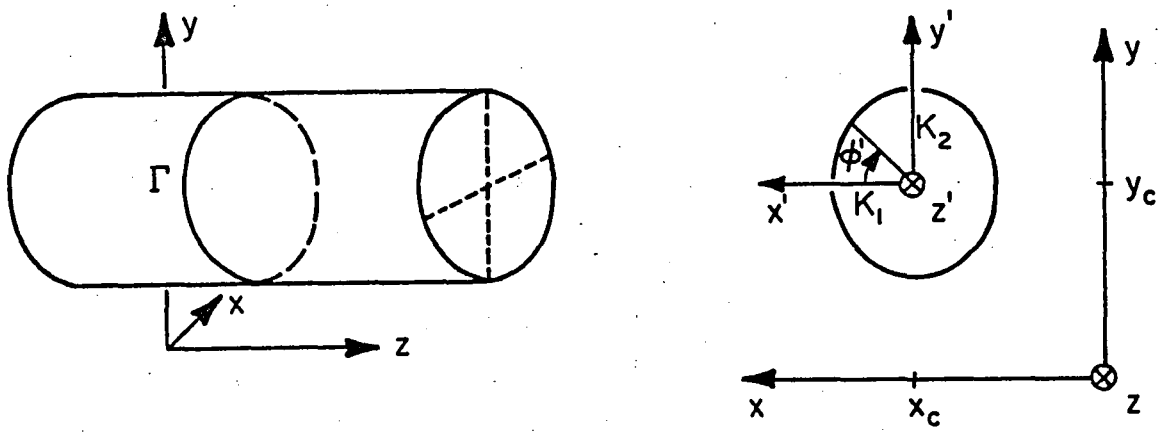

(a) Γ on elliptical cylinder

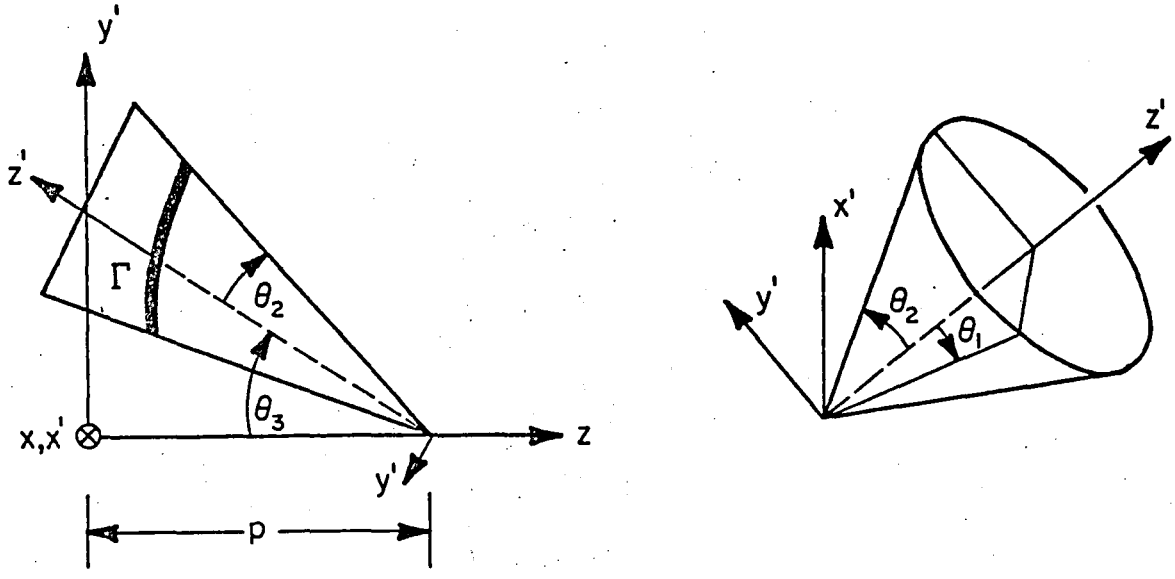

(b) Γ on elliptical cone

Reflector and feed coordinate systems

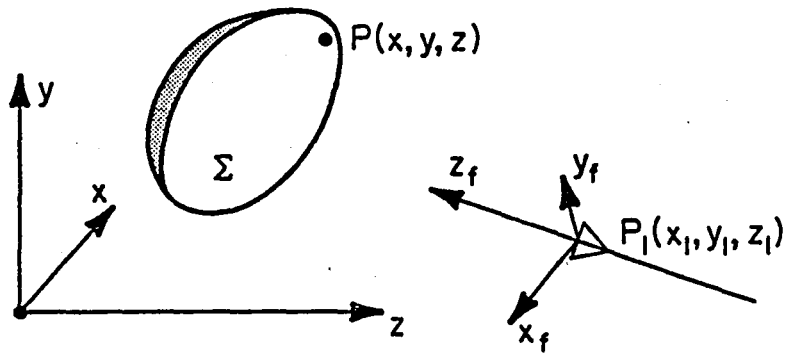

Reflector and feed coordinate systems

Eulerian angles $\gamma_1, \gamma_2, \gamma_3$

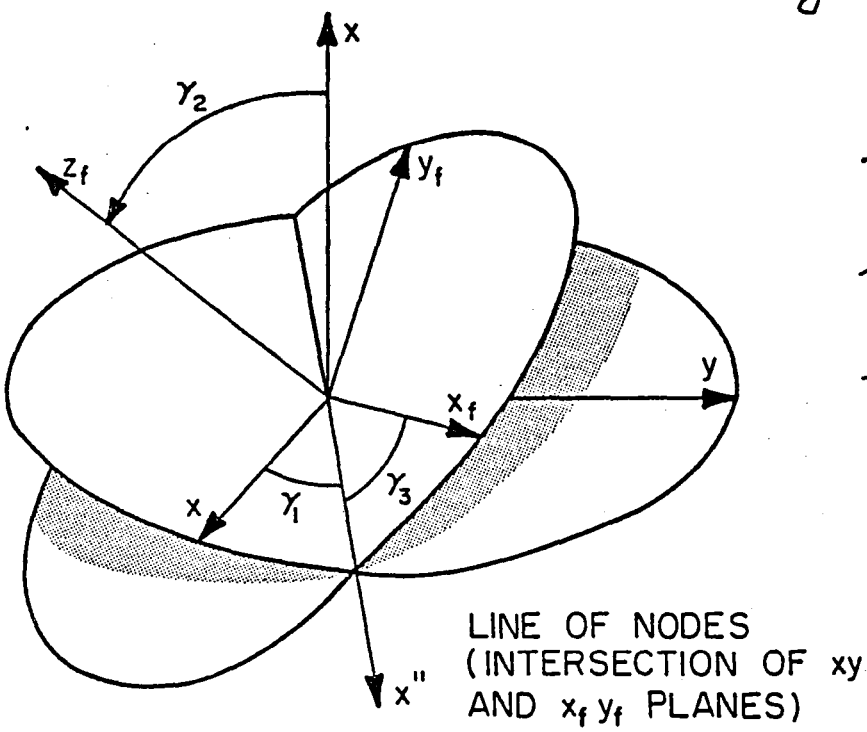

γ_1 brings x on x'' about z

γ_2 brings z on z_f about x''

γ_3 brings x'' on x_f about z_f

Uniform theories

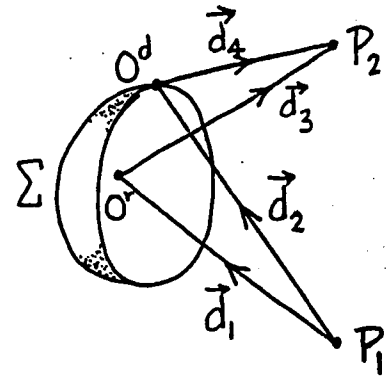

Detour parameter ξ :

$$\xi = \varepsilon\left[k\left(d_3 + d_4 - d_1 - d_2\right)\right]^{1/2}$$

$$\varepsilon = \begin{cases} +1 & \text{if } P_2 \text{ is in the shadow side of the reflected field} \\ -1 & \text{if } P_2 \text{ is in the lit side of the reflected field} \end{cases}$$

$|\xi| > 2$, no correction required

$|\xi| \leq 2$, $\vec{H}^d(P_2)$ must be modified

UAT

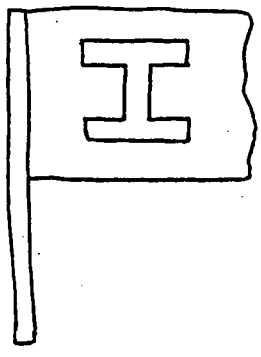

UTD

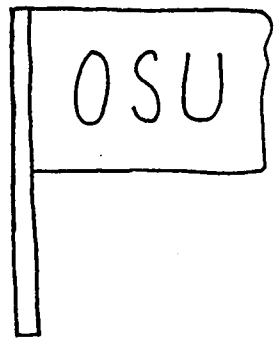

Directivity formulas

Secondary pattern:

$$\vec{E} = \frac{e^{-jkr}}{r}\left[\hat{\theta}\, U_\theta + \hat{\phi}\, U_\phi\right]$$

Two unitary polarization vectors:

$$\hat{R} = \hat{\theta}\left(a e^{j\psi}\cos\phi + b\sin\phi\right) + \hat{\phi}\left(-a e^{j\psi}\sin\phi + b\cos\phi\right)$$

$$\hat{C} = \hat{\theta}\left(a e^{-j\psi}\sin\phi - b\cos\phi\right) + \hat{\phi}\left(a e^{-j\psi}\cos\phi + b\sin\phi\right)$$

Reference-polarization of $\vec{E} = \vec{E}\cdot(\hat{R}^*)^*$

Cross-polarization of $\vec{E} = \vec{E}\cdot(\hat{C}^*)^*$

Reference-polarization directivity:

$$D_R(\theta,\phi) = \frac{4\pi\,|\vec{E}\cdot\hat{R}|^2/Z_0}{P_{inc}}$$

Cross-polarization directivity:

$$D_C(\theta,\phi) = \frac{4\pi\,|\vec{E}\cdot\hat{C}|^2/Z_0}{P_{inc}}$$

Incident power radiated

$$P_{inc} = \int_{\phi=0}^{2\pi} \int_{\theta=0}^{\frac{\pi}{2}} \frac{\vec{E} \cdot \vec{E}^*}{Z_o} r^2 \sin\theta \, d\theta \, d\phi$$

$$\vec{E} = \sum_{m=1}^{M} \vec{E}_{em} I_m e^{jk\hat{u}\cdot\vec{\rho}_m}$$

$$\vec{E}_{em} = \frac{e^{-jkr}}{r}\left[\hat{\theta}\, U_{Em}(a e^{j\psi}\cos\phi + b\sin\phi) + \hat{\phi}\, U_{Hm}(-a e^{j\psi}\sin\phi + b\cos\phi)\right]$$

Assume

$$U_{Em} = (\cos\theta)^{q_{Em}}$$

$$U_{Hm} = (\cos\theta)^{q_{Hm}}$$

For arbitrary polarization,

P_{inc} may be expressed in terms of $\left\{\begin{matrix}\text{Bessel}\\ \text{Gamma}\\ \text{Lommel}\end{matrix}\right\}$ functions.

Offset parabolic reflector

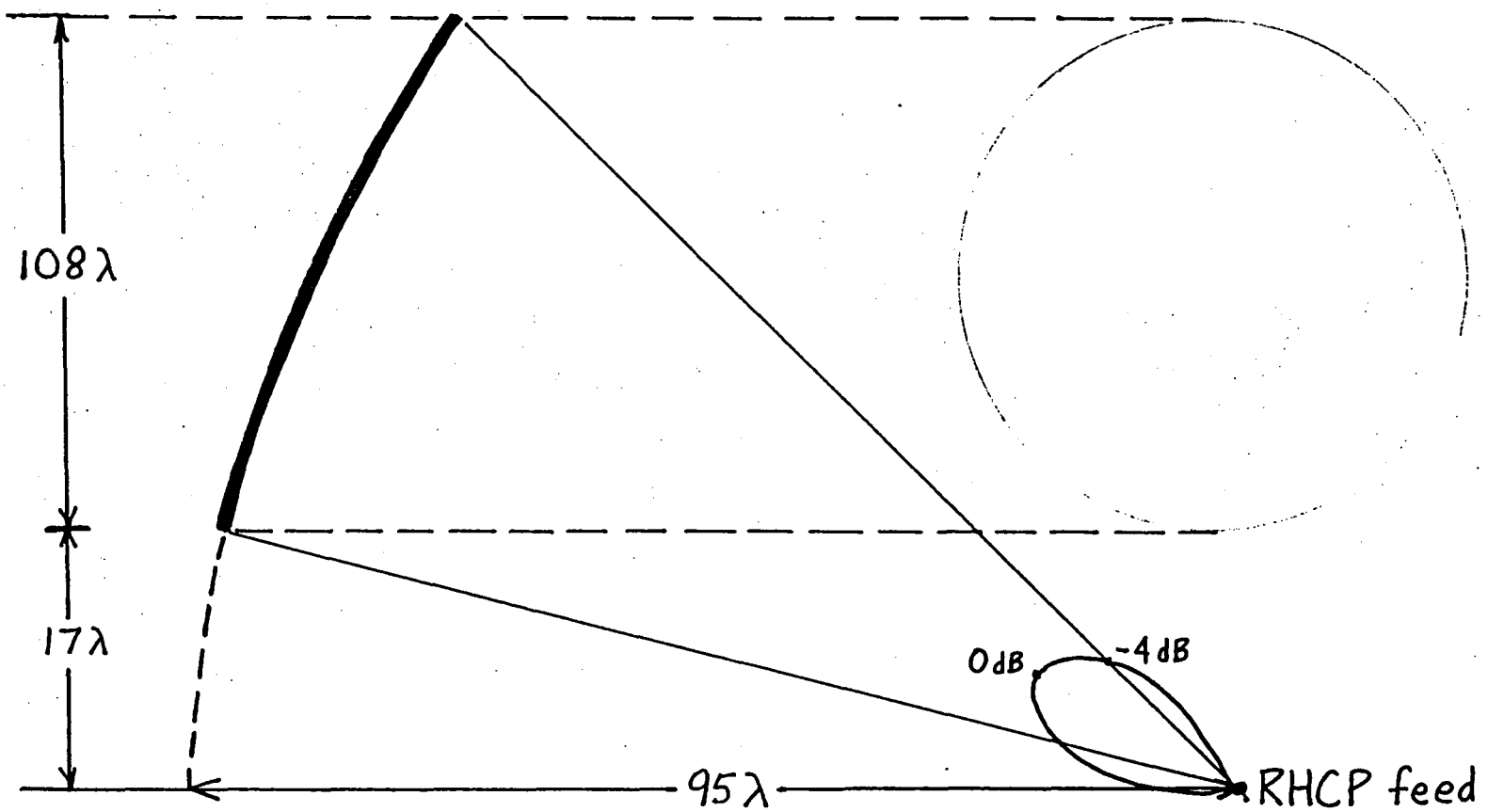

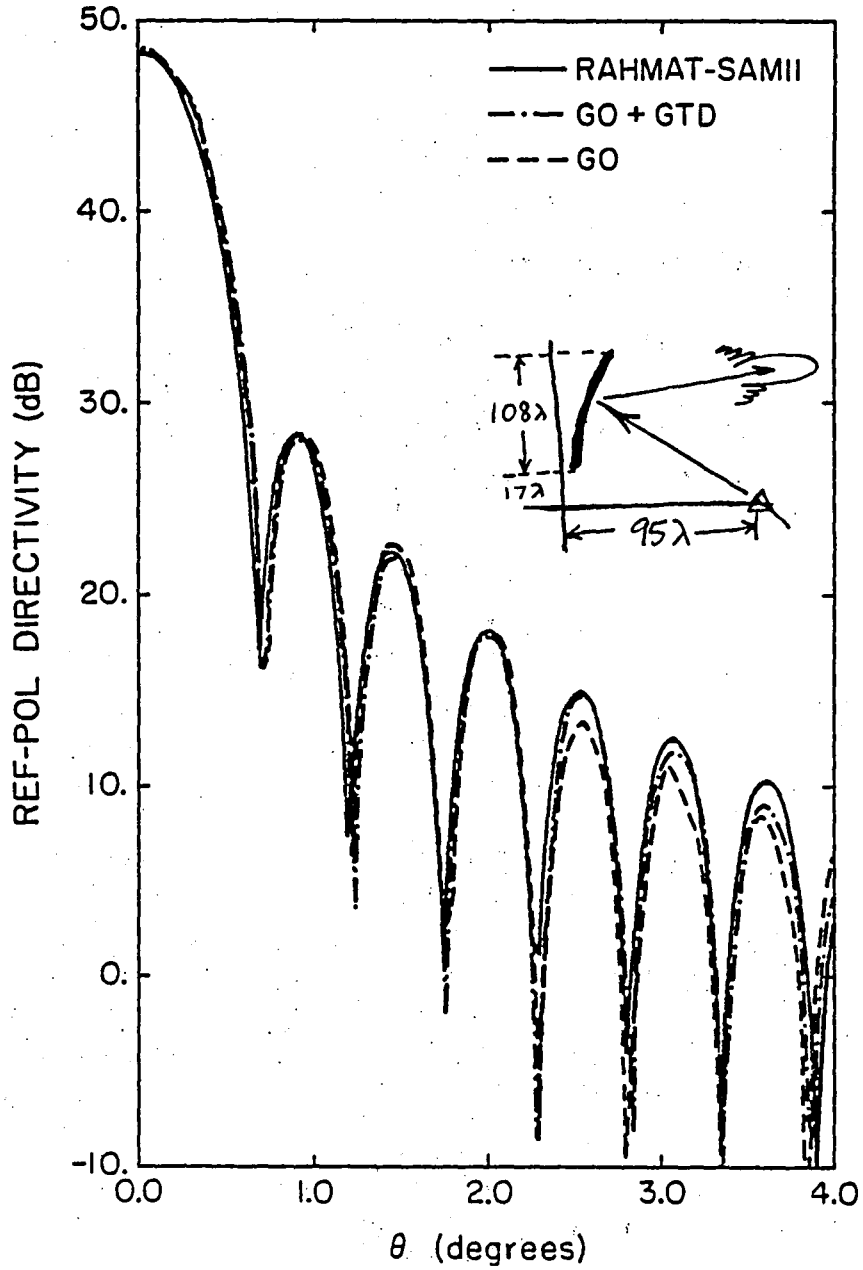
RAHMAT-SAMII
GO + GTD
GO
REF-POL DIRECTIVITY (dB)
θ (degrees)
50.
40.
30.
20.
10.
0.
-10.
0.0
1.0
2.0
3.0
4.0
108λ
17λ
95λ

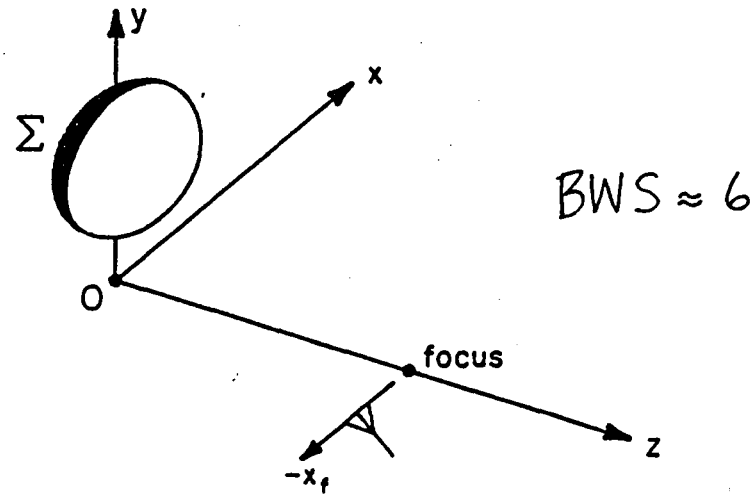
y
x
Σ
O
focus
z
$-x_f$
BWS ≈ 6

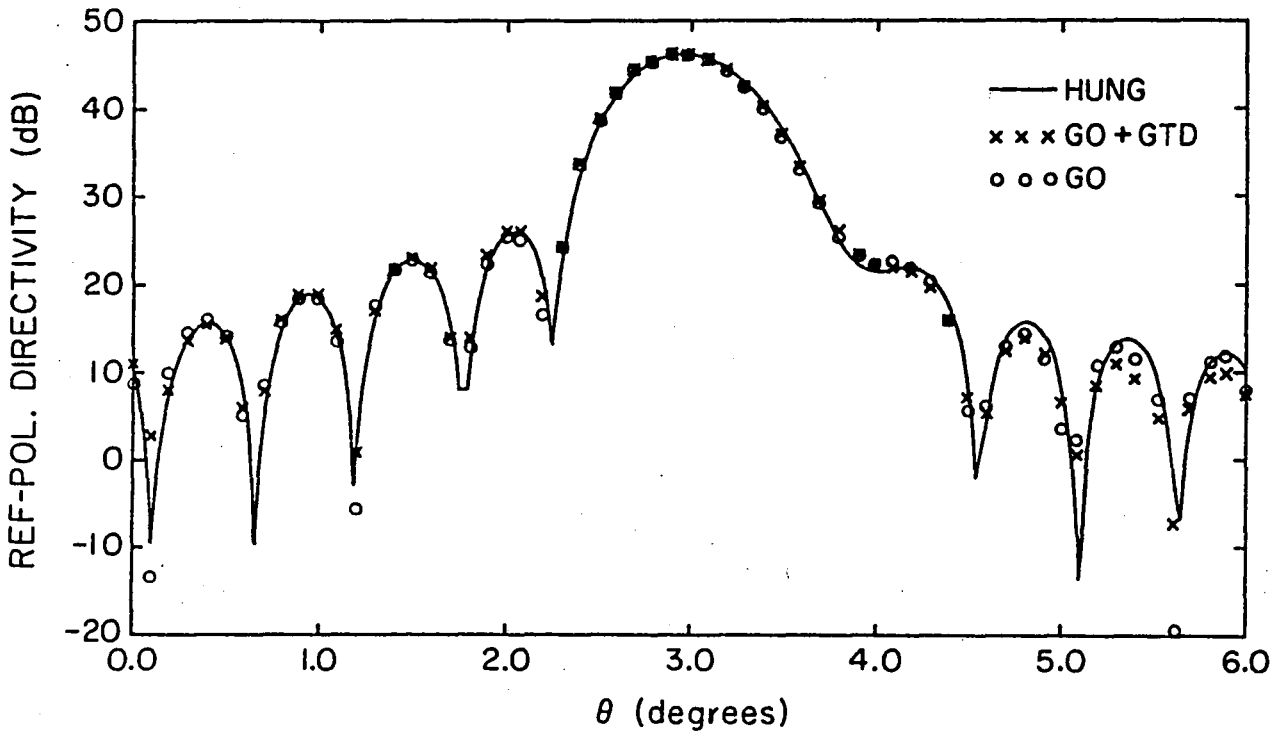
HUNG
× × × GO + GTD
o o o GO
REF-POL. DIRECTIVITY (dB)
θ (degrees)
50
40
30
20
10
0
-10
-20
0.0
1.0
2.0
3.0
4.0
5.0
6.0

CONCLUSION

* With this AI approach, the main beam and sidelobe regions of the secondary pattern is accurately computed.

* The reflector shape is completely arbitrary.

* This technique is numerically efficient by employing the FFT.

* Near field measurements may be checked.

* This AI formulation is suitable for extension to multiple reflectors.

Future work

* extend technique to a dual reflector system
* array feed
* multiple reflectors

1. Report No.	2. Government Accession No.	3. Recipient's Catalog No.
NASA TM-87162		

4. Title and Subtitle	5. Report Date
Secondary Pattern Computation of an Arbitrarily Shaped Main Reflector	November 1985
	6. Performing Organization Code: 506-62-52
7. Author(s): Peter T.C. Lam, S.W. Lee, and R. Acosta	8. Performing Organization Report No.: E-2796
	10. Work Unit No.
9. Performing Organization Name and Address: National Aeronautics and Space Administration, Lewis Research Center, Cleveland, Ohio 44135	11. Contract or Grant No.
	13. Type of Report and Period Covered: Technical Memorandum
12. Sponsoring Agency Name and Address: National Aeronautics and Space Administration, Washington, D.C. 20546	14. Sponsoring Agency Code

15. Supplementary Notes

Final report. Peter T.C. Lam and S.W. Lee, University of Illinois, Urbana, Illinois; and R. Acosta, NASA Lewis Research Center.

16. Abstract

This report studies the secondary pattern of a perfectly conducting offset main reflector being illuminated by a point feed at an arbitrary location. The method of analysis is based upon the application of the Fast Fourier Transform (FFT) to the aperture fields obtained using geometrical optics (GO) and geometrical thoery of diffraction (GTD). Key features of the present work are (i) the reflector surface is completely arbitrary, (ii) the incident field from the feed is most general with arbitrary polarization and location, and (iii) the edge diffraction is calculated by either UAT (Lee and Deschamps) or by UTD (Kouyoumjian and Pathak). Comparison of this technique for an offset parabolic reflector with the Jacobi-Bessel and Fourier-Bessel techniques shows good agreement. Near field, far field, and scan data of a large reflector are presented.

17. Key Words (Suggested by Author(s))	18. Distribution Statement
Antenna; Electromagnetics; Physics	Unclassified - unlimited STAR Category 32

19. Security Classif. (of this report)	20. Security Classif. (of this page)	21. No. of pages	22. Price*
Unclassified	Unclassified		

*For sale by the National Technical Information Service, Springfield, Virginia 22161

End of Document